IR transmission optimisation for Cadmium Telluride

Sverre Magnus Engø

Master thesis in measurement technology and nano physics

Supervisor:
Martin Møller Greve

Faculty of Mathematics and Natural Science
University of Bergen

June 2021

Abstract

Cadmium Telluride (CdTe) alloys are extensively used as IR detection substrates, and since its discovery in the 1960s [45] it has been the subject of several technological improvements. Among the advantages of CdTe is its customizable refractive index. CdTe has a high transmission ($\approx 70\%$) over the whole IR range. IR transmission can reach values of 99% narrow-band, or upwards of 90% average transmission over a broad range(0.45-20μm). Several anti-reflective methods are examined for transmission optimisation for CdTe, with varying improvements. Surface roughness is examined, as it is the precursor to moth-eye structures, and found to affect the transmission. Anti-reflective coatings (ARCs) are used for specific narrow-band transmission, with attempts at dual-band transmission with decent results. Then anti-reflective micro-structures (ARMS) are designed and simulated with promising results of transmission upwards of 99% for larger bands.

Acknowledgement

Contents

List of Figures

List of Tables

1   Introduction

As technology has kept advancing, the infrared (IR) spectrum has attracted more and more interest within the scientific communities, especially within detector technology. This becomes apparent as it is possible today to buy hand held IR detectors of reasonable quality within consumer prices, when earlier devices needed a steady vacuum, or extensive cooling methods, and were only available to large companies or the military. The interest in the infrared is justified through the fact that IR spectroscopy is an integral method within most of the sciences. All objects which carry heat radiate in the IR, making almost *everything* visible to some degree in the IR. To make these detectors, *some* material must allow the radiation to reach the detector, and this material is Cadmium Telluride. This semiconductor works as an entrance window for the radiation to reach the optoelectronics inside, and hence the transmission window must be optimised for the IR to make sure the electronics can work with as much radiation as possible. Therefore, several methods that optimise the IR transmission for CdTe is discussed here.

1.1   Objectives of this thesis

The main goal of this thesis is to improve the electromagnetic (EM) transmissivity of CdTe for both narrow and broad transmission bands, and identify useful anti-reflection (AR) techniques for the highest peaks in the atmospheric window. This will be done by applying either a single layered anti-reflective coating (ARC), or by nano-structuring the surface with anti-reflective micro structures (ARMS). Comparisons will be made, and designs from the literature are tested. The summarised goals are to

- Simulate the broadband IR transmission for untreated CdTe.

- Identify effects that affect IR-transmission for CdTe.

- Simulate anti-reflective coatings for the atmospheric window peaks, and determine optimal parameters for said coatings.

- Coat the CdTe substrate in a anti-reflective material and measure the new transmission bands.

- Compare findings with a reference material - namely Silicon.

- Design and find useful configurations of ARMS for CdTe and create these in Lumerical FDTD.

- Simulate nano-structured surface for CdTe.

- Compare results with literature.

1.2   Thesis outline

First, some theory for the mechanisms of transmission is explained and described, as well as the material specific properties which will affect the results. Several anti-reflective techniques and designs are presented and discussed, including some mechanisms for how they work, and which will be the best designs. A short dive is done into the fabrication techniques and other difficulties in working with these materials. The general setup for the simulations is explained in the methods section, along with some basic analysis into the packing of the materials. Finally, the simulations are presented in the results, along with some initial experimental results are performed, such as AFM measurements of the surface, and FTIR measurements of the transmissivity. Lastly the discussion and conclusion where the success of the designs studied is discussed.

2 Theory

The physics behind the mechanisms for transmission are fortunately not riddled with abstractions and heavy mathematics, but *some* formulation must be acknowledged. First, the physical mechanisms for EM-radiation in a medium boundary must be understood to analyse *how* the methods presented work, and why such methods are selected. It is also useful to understand the working environment of the devices this technology is for. Some materials science is necessary to understand the design choices made in the earlier development of this technology.

2.1 IR technologies

Infrared light was only "discovered" around 200 years ago, and like many other scientific discoveries, it was somewhat of an accident. Sir Frederick William Herschel wanted to measure the energy distribution in different colours of light in the atmosphere. He did so by splitting the light in a prism, and then pointing a thermometer onto each colour, so that he could see how fast the temperature would rise per time "per colour". He was surprised to see that the temperatures rose faster the closer to red light he measured. Because of this rising energy distribution towards the red light, he decided to point a thermometer further out than the red light - in a invisible region - and he discovered that the temperature here was higher than any other point. He had just discovered "invisible" light beyond the red - hence *infra*red. Until recent launch and successful deployment of the James Webb Telescope in December 2021, the Herschel Space Observatory (in his name) was the largest infrared telescope ever built, and was used to gather a plethora of astronomic data.

The infrared range covers 0.7 - 1000 μm, and is subdivided into several smaller ranges as shown in table 1. These subdivision are selected because each range covers *many* different fields of science. In addition, the IR spectrum encompasses the *atmospheric windows*, which are the wavelengths of light that reach the ground on earth, from the sun. This window can be seen as the optimal transmission wavelengths for transversal in air, and will be used to compare the results. In chemistry, one can use IR to analyse and categorize molecules, their movement and energy distribution (degrees of freedom), and the same mechanisms which make IR useful in these applications, cause large absorption bands in the atmospheric windows. In astronomy, one can see the temperatures of celestial bodies by measuring its black-body radiation according to Wien's displacement law, which describes the spectral emission from an object based on its temperature. IR thermal imaging can be used by emergency services for search and rescue missions. It is heavily used by the military for IR thermal imaging by satellite, tracking systems for rockets and much more

Table 1: Overview over the ranges (wavelength, frequency and energy) and names and abbreviations of the infrared bands.[35]

Name	Abbreviation	Wavelength	Frequency	Photon energy
Near IR	**NIR**	0.75-1.4 μm	214-400 THz	886 - 1653 meV
Short-wavelength IR	**SWIR**	1.4-3 μm	100-214 THz	413 - 886 meV
mid-wavelength IR	**MWIR**	3-8 μm	37-100 THz	155-413 meV
Long-wavelength IR	**LWIR**	8-15 μm	20-37 THz	83-155 meV
Far IR	**FIR**	15-1000 μm	0.3-20 THz	1.2-83 meV

IR has a major advantage to visible light when trying to observe with EM-detectors, namely that everything that holds heat, radiates in the IR. This makes it possible to view warm objects even through a colder environment, like a flash light in a mist. When viewing in the visible light spectrum, one is dependent on the background radiation which is caused by scattered photons in the atmosphere. When detecting IR radiation on the other hand, there is no need for the reflected background radiation from external light sources. But rather *everything* that contains heat will radiate IR radiation though *blackbody radiation*. A *blackbody* is an object which absorbs all radiation and re-radiates it in a different wavelength - mainly in the IR. This will be described in greater detail below. Some modern IR detection-devices generate their own background - like a camera uses flash to light up a room - and are called *active* detectors. *Passive* detectors on the other hand, will only detect the radiation that emanates from the environment. Detection in the visible range means *more* light - hence more information, and better signal to noise ratio. However, IR technology can use the fact that an ambient homogeneous temperate scene generate close to no contrast, allowing easier detection of warm surfaces, such as detecting surface temperatures by hand held devices, finding people in search-and-rescues, molecular vibration-detection, gas detection/analyser.

While IR detection is usually done passively by detecting radiation emanating from either a *blackbody* or a specific chemical process. This means that detection in a pitch black room is possible (night vision), or detection through smog/mist. IR sensors makes it possible to measure temperatures wirelessly with a IR thermometer, or measure the humidity with an active IR absorbance meter. There is an abundance of applications for IR detection in the whole range, and so, improving the transmission into the detectors allows for even more sensitive data, and new applications.

2.2 Cadmium Telluride

CdTe is a II-VI semiconductor alloy with a wide range of applications from optoelectronics [8]. CdTe has a closely optimal band gap of ≈ 1.52 eV (≈ 0.81 μm) in room temperature and a low absorption coefficient [50] above the band-gap (wavelength). Its applications range from infrared windows in high-energy CO_2 lasers, to microwave generation, light absorber in high-efficiency solar panels, substrate for IR detectors, and much more [36]. Additionally, the high average atomic number, high band gap and sufficient electron- and hole-mobility lifetime makes it useful in nuclear particle detection. CdTe has a very wide transmission range (0.85-30μm), but with a relatively high refractive index of ≈ 2.73. This high refractive index is the reason for the large Fresnel reflection losses observed [8]

- more details will follow.

Ever since its discovery as a material with remarkable IR-optoelectronic properties, extensive research into what surface coatings can be applied to it for increased light transmission has been performed. Then more recently *micro structuring* the surface has been explored to customize its surface properties like spectral transmission, hydrophobia and contamination resistance, and angle of incidence dependence for the transmission [10]. Both of these techniques (surface coatings and micro-structuring) will be explored later in the thesis. The refractive index of CdTe has a spectral dependence [6], and as such, a reliable set of values for the indices in the ranges 0.45-20 μm must be used.

The refractive index for CdTe reported by several providers are shown in figure 1 below. The datasets each cover different intervals, with the datasets from Hlìdek and Palik covering the entire range. The agreement between the datasets is very good. These data sets will hereby be referred to as only "Hlidek", "Palik", "Reading" and "Marple". Additionally, the transmission band for CdTe around 0.45-20 microns reported from two professional providers, and FFI (Forsvarets Forskningsinsitutt) is shown below in figure 2.
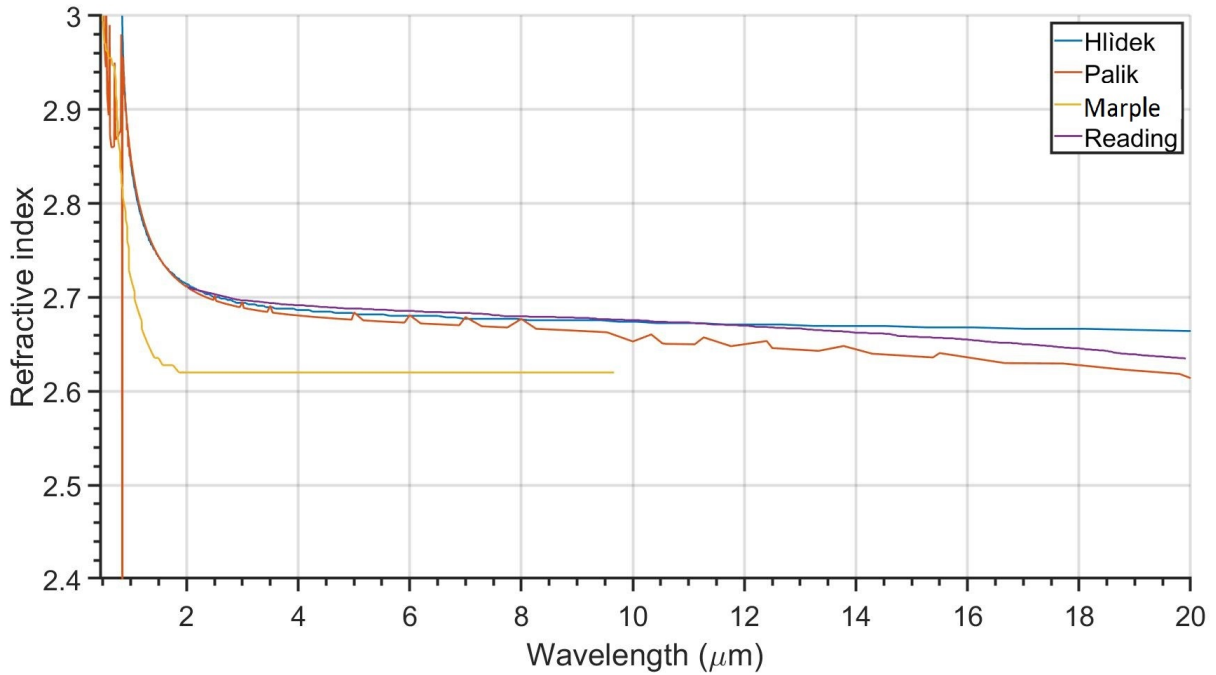
Figure 1: *Refractive index for CdTe reported from different datasets: [18], [33], [26], [40]. These data are extracted from low-resolution papers, and hence the data-point extraction are limited by this resolution.*

6
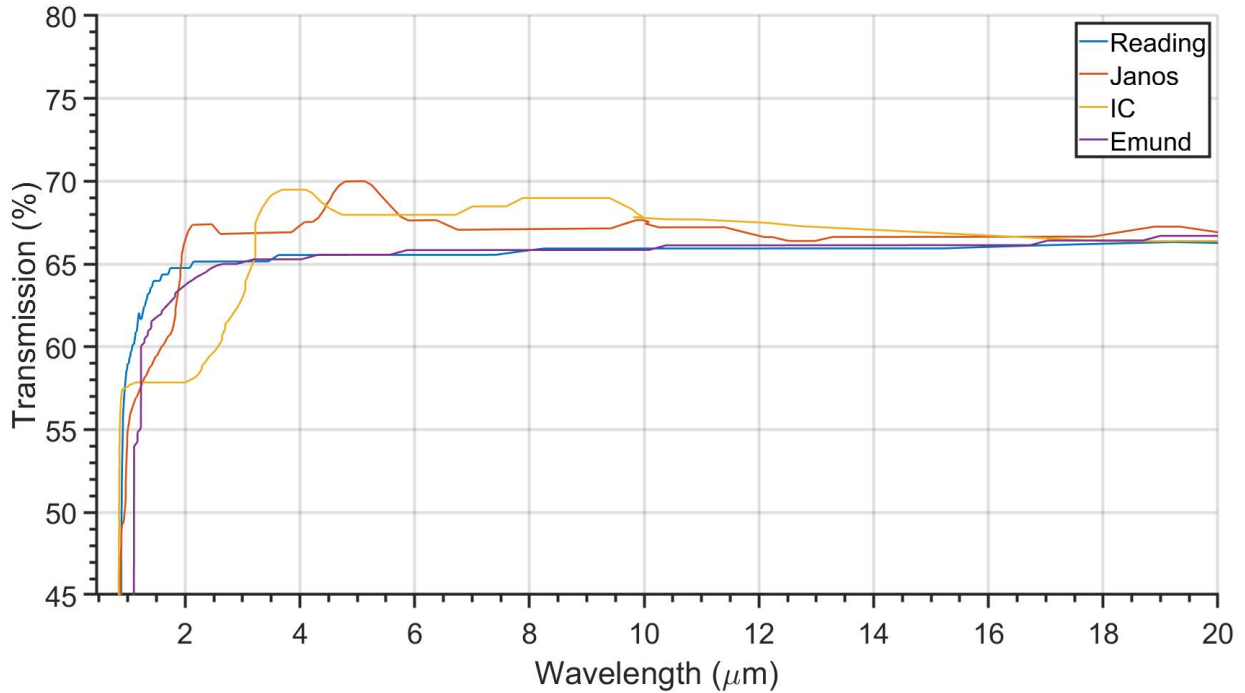
Figure 2: *The transmission spectra for bare Cadmium Telluride reported from three CdTe providers [30], [32], [12], and the university of Reading [40].*

CdTe in its early days seemed like the "go to" material for IR optoelectronics and visible light photovoltaic applications because of its high transmissivity in the IR range, and high absorption in the visible range. In modern times though, it has been acknowledged that alloying could produce new properties, or allow customization of properties. It didn't take long from the discovery of CdTe before zinc and mercury was introduced to the alloy, allowing for a wider collection of use cases. Two of these alloys are of particular interest because of their wide range of applications in IR optoelectronics, and will be discussed in the following chapters.

2.2.1   CdZnTe - CZT

Alloying CdTe is a great way to produce further tailored properties. For this reason, zinc has been applied to CdTe almost since it discovery. The addition of Zinc allows precision customization of the lattice constant, which is very helpful when layering different alloys, and CdZnTe (CZT) is often layered with HgCdTe (MCT) [50]. In addition, CZT shows very similar transmission properties for the IR range in question (3-5 & 8-12 μm), with a 21% reflection in the 7-14 micron range. Zinc also has the effect of improving the mechanical strength of the alloy, and helps produce a less fragile substrate. This does not come without caveats, however. Telluride segregates during crystal growth, producing an inhomogeneous distribution in the lattice, but it has also been determined that Zn also does this, causing even further inhomogeneity. There are methods to avoid this, but the introduction of Zn produces some more complexity to the crystal production.

For the most part, CdTe and CZT display the same properties in simulation, as their refractive indices are very similar. Therefore most analyses done with for example FDTD simulations in Lumerical can be extended to CdZnTe applications, but clearly other concerns must be addressed, such as chemical compatibility and precision measurements

of material properties should be redone for CZT if this is to be extended to experimental work.

2.2.2   HgCdTe - MCT

Mercury Cadmium Telluride (MCT) is in the literature known as the most important semiconductor material for middle and long wave IR (3-30 μm) photo detector, but it has been attempted to be replaced for a while because of its main caveats [44]. One of the large drawbacks of HgCdTe is the weak bond between Hg - Te. This means that during production, the temperature must be quite low in comparison with normal working temperatures for alloys. Among the reasons as to why HgCdTe has not been replaced yet are found to be extreme flexibility, as the refractive index can be tailored for the whole IR region. Additionally the lattice parameter difference between CdTe and HgCdTe is close to zero ($\approx 0.2\%$). This allows both CdTe and HgCdTe to work as either substrate or coating with little to no lattice mismatch stress between the boundaries, and even this small mismatch can be compensated for by alloying either two materials with trace amounts of Zinc or Telluride.

2.3   Silicon

Silicon is the most important semiconductor in the world, as it is the key component in all integrated circuitry, and it has dominated the electronics industry for 40 years [43]. This has industrialised the production of high quality crystals, which is a requirement for its use in optoelectronics. Silicon, whose physical and optical constants are well know, serves itself well as a substitute for other expensive materials for optoelectronic research - in this case, as a substitute for the CdTe substrates. The refractive index for Si is ≈ 3.43 for the IR region [13], which is quite high for transmission purposes, but circumventable. Si has a wide transmission band of $0.85 - 20\mu$m [20]. Moreover, it has a bandgap of 1.12 eV (1.07μm), and hence is highly absorbing in the Near IR (NIR) bands. Additionally, the complex refractive index is quite sensitive to crystal quality - and hence absorption is heavily dependent on the crystal quality [20].

2.4   Mechanisms of EM transmission and reflection in semiconductors

The conditions for the transmission of electromagnetic radiation into a medium are governed by the boundary conditions between the two media surfaces, and the frequency of the incident rays. By solving Maxwell's equations for a sliver of material in contact with a second material, one gets the boundary conditions (*i-iv*) below, given that the media do not contain bound charges (media must be linear) [16].

$$(i) \quad \epsilon_1 E_1^\perp - \epsilon_2 E_2^\perp = 0, \quad (iii) \quad \mathbf{E}_1^\parallel - \mathbf{E}_2^\parallel = \mathbf{0}$$

$$(ii) \quad B_1^\perp - B_2^\perp = 0, \quad (iv) \quad \frac{1}{\mu_1}\mathbf{B}_1^\parallel - \frac{1}{\mu_2}\mathbf{B}_2^\parallel = \mathbf{0}$$

Here, E is the electric field, B is the magnetic field, ϵ and μ is the permittivity and permeability respectively. Suppose a plane wave traveling in the z-direction, hitting the material. The incoming wave is described by:

$$\tilde{E}_I(z,t) = \tilde{E}_{0I} \, e^{i(k_1 z - \omega t)}\hat{\mathbf{x}}$$

$$\tilde{B}_I(z,t) = \frac{1}{v_1}\tilde{E}_{0I} \, e^{i(k_1 z - \omega t)}\hat{\mathbf{y}} \tag{1}$$

The reflected wave is described by:

$$\tilde{E}_R(z,t) = \tilde{E}_{0R} \, e^{i(-k_1 z - \omega t)}\hat{\mathbf{x}}$$

$$\tilde{B}_R(z,t) = \frac{1}{v_1}\tilde{E}_{0R} \, e^{i(-k_1 z - \omega t)}\hat{\mathbf{y}} \tag{2}$$

and lastly, the transmitted wave into the medium:

$$\tilde{E}_T(z,t) = \tilde{E}_{0T} \, e^{i(k_2 z - \omega t)}\hat{\mathbf{x}}$$

$$\tilde{B}_T(z,t) = -\frac{1}{v_2}\tilde{E}_{0T} \, e^{i(k_2 z - \omega t)}\hat{\mathbf{y}}$$

Here, the tilde implies that the complex amplitudes are used. The k is the wave number for the wave function, t is time, and ω is the angular frequency. At the medium boundary the sums of the electric fields must be the same on each side:

$$\tilde{E}_I + \tilde{E}_R = \tilde{E}_T \tag{3}$$

Now, (iv) can be rearranged by using $B_1 = B_I + B_R$ and formulas 1 and 2.

$$\frac{1}{\mu_1}\left(\frac{1}{v_1}\tilde{E}_{0I} - \frac{1}{v_1}\tilde{E}_{0R}\right) = \frac{1}{\mu_2}\left(\frac{1}{v_2}\tilde{E}_{0T}\right)$$
$$\Rightarrow$$
$$\tilde{E}_I - \tilde{E}_R = \frac{\mu_1 n_2}{\mu_2 n_1}\tilde{E}_T$$

for which the amplitudes can be solved with (1), which gives

$$\tilde{E}_R = \frac{1-\beta}{1+\beta}\tilde{E}_I, \;\; \tilde{E}_T = \frac{2}{1+\beta}\tilde{E}_I, \;\; \beta = \frac{\mu_1 n_2}{\mu_2 n_1}$$

For most media, the permeability is almost the same as the value for vacuum, and so β can be rewritten as $\beta = \frac{v_1}{v_2}$. Using this and the fact that reflection and transmission are both *ratios* of reflected versus incident light, and transmitted versus incident light,

the amount of reflected and transmitted light from one media to another can be written as:

$$R \equiv (\frac{n_1 - n_2}{n_1 + n_2})^2, \quad T \equiv \frac{4n_1 n_2}{(n_1 + n_2)^2} \tag{4}$$

For which the sum (R + T) must equal 1. For these equations, it is trivial to see that the reflection goes to zero as the refractive index difference goes to zero, or as n_1 nears n_2: $n_1 -> n_2$. This implies that there are some basic *gradient index of refraction* methods which *gradually* increases the refractive index between the media which would work very well at avoiding reflection. These methods will be discussed in detail below.

2.4.1 impedance matching

Another way to describe *how* an EM wave is reflected or transmitted, is by imagining the wave as a 1D string. Then the amplitudes of the incident, reflected and transmitted wave can be described by (3). In wave form on the other hand, the equation takes a different shape:

$$\psi_I + \psi_R = \psi_T \tag{5}$$

Where ψ_x is the wave function for incidence, reflected and transmitted waves respectively. Clearly, just like general waves, the wave must adhere to the generalized wave function and its boundary conditions on each side of a medium change presented below (6 and 7).

$$[\frac{\partial^2}{\partial t^2} - v^2 \frac{\partial^2}{\partial x^2}]\psi_{1/2} = 0 \tag{6}$$

$$\psi_I(0, t) + \psi_R(0, t) = \psi_T(0, t) \tag{7}$$

$$T_1 \frac{\partial \psi_1(0, t)}{\partial x} = T_2 \frac{\partial \psi_2(0, t)}{\partial x} \tag{8}$$

Here the T stands for the material tension, and is described by $T = v^2 \mu_m$ for a string, with μ_m as the linear mass density of the string, and v is the material speed of sound. Now imagine that the string is attached at a junction, after which a new string is attached to the first string, but with different material properties(such as density or stiffness). What then happens with an incoming wave from the first string, and onto the junction? Depending on the difference in material impedance, the wave will be proportionally transmitted or reflected. If the impedance difference is large, then the transmission of energy will be resisted, and high reflection is observed. It can be shown that (5) describes the left and right side of the junction, and applying the boundary conditions (7), one arrives at:

$$\psi_R = \frac{\frac{T_2}{v_1} + \frac{T_1}{v_2}}{\frac{T_1}{v_1} - \frac{T_2}{v_2}} \psi_I \tag{9}$$

This relationship describes the amplitude of the reflected wave for a given material boundary with tensions T_1 and T_2, wave speeds v_1 and v_2 (light speed for EM radiation), and incoming wave amplitude of ψ_I. For any given medium, the material impedance is defined as $Z = \frac{T}{v}$, and in a homogeneous material the EM wave impedance is everywhere equal to the intrinsic impedance of the medium. Hence, the fraction in the above formula (9) describes the *reflection coefficient*, and the *transmission coefficient* can be calculated by substituting (9) into (7):

$$\psi_R = R\psi_I, \quad R = \frac{Z_1 - Z_2}{Z_1 + Z_2} \tag{10}$$

$$\psi_T = T\psi_I, \quad T = \frac{2Z_1}{Z_1 + Z_2} \tag{11}$$

These equations imply that there is a "perfect" method of achieving perfect transmission - *simply* match the material impedances for the whole material boundary. This can be translated to a matter of having a gentle slope for the gradient of the refractive index, as can be seen by the similarities of the reflection and transmission coefficients calculated by Maxwell's equations, and the coefficients achieved by impedance matching; they are the same calculations but with different abstractions. The maths seems optimistic on paper, which is reflected in the lack of perfect transmitters out in the world today. "Simply" matching the impedances implies an infinitely slack slope of the gradient of refractive index, which implies infinite thickness of the anti-reflective layer, which is clearly impossible.

2.5 Absorption

CdTe has high optical absorption close to its bandgap of 1.52 eV, but it rapidly decreases - From around 10^4 at 1.52 eV to 10^1 at 1.45 eV [1]. This low absorption at longer wavelengths allow for almost all the EM radiation to reach the detector through the substrate, which is why CdTe is a lucrative material for use in IR optics.

For an uncoated and polished chip of CdTe, the optical transmission at normal incidence *with* backside-reflection lies around 63% [4] (This thesis excludes backside-reflections, as the device design behind the substrate is not clear at this point). The ranges for the transmission are determined in the lower wavelengths by the electronic bandgap, and for the longer wavelengths by lattice vibrations.

For semiconductors there are four principal mechanisms for optical absorption, namely: Inter-band electronic transitions, fundamental and harmonic lattice vibrations including multi-phonon processes, impurity absorption, and lastly free carrier absorption. These factors can be the dominant cause for absorption, but is mostly preventable by using high quality crystals and polish, and hence excluded unless the crystals used are shown to be less than perfect. The actual absorption for CdTe in the ranges 0.45-20 μm is close to zero for the substrate thicknesses used here.

2.6   Mechanisms of IR emission - Blackbody radiation

All objects in the universe that have internal thermal energy, will emit IR radiation. An ideal blackbody is an object which absorbs all incoming radiation and re-emits it in a distribution described by Planck's radiation law. Most life on earth are a higher temperature than their background, certainly humans. This means that humans are *blackbodies*, and hence radiate in the IR, which they do alot of [14]. Human bodies are about 37° degrees celcius. This can be used with Plancks law of blackbody radiation to find the emission spectrum. This law shows the spectral power density of a blackbody per its temperature, and so, solving it will show *which* wavelengths an object radiates. Below are presented the formula and its graph for a 37° C object.

$$W(\lambda, T) = \frac{2\pi h c^2}{\lambda^5} [exp(\frac{hc}{\lambda k T}) - 1]^{-1} \tag{12}$$
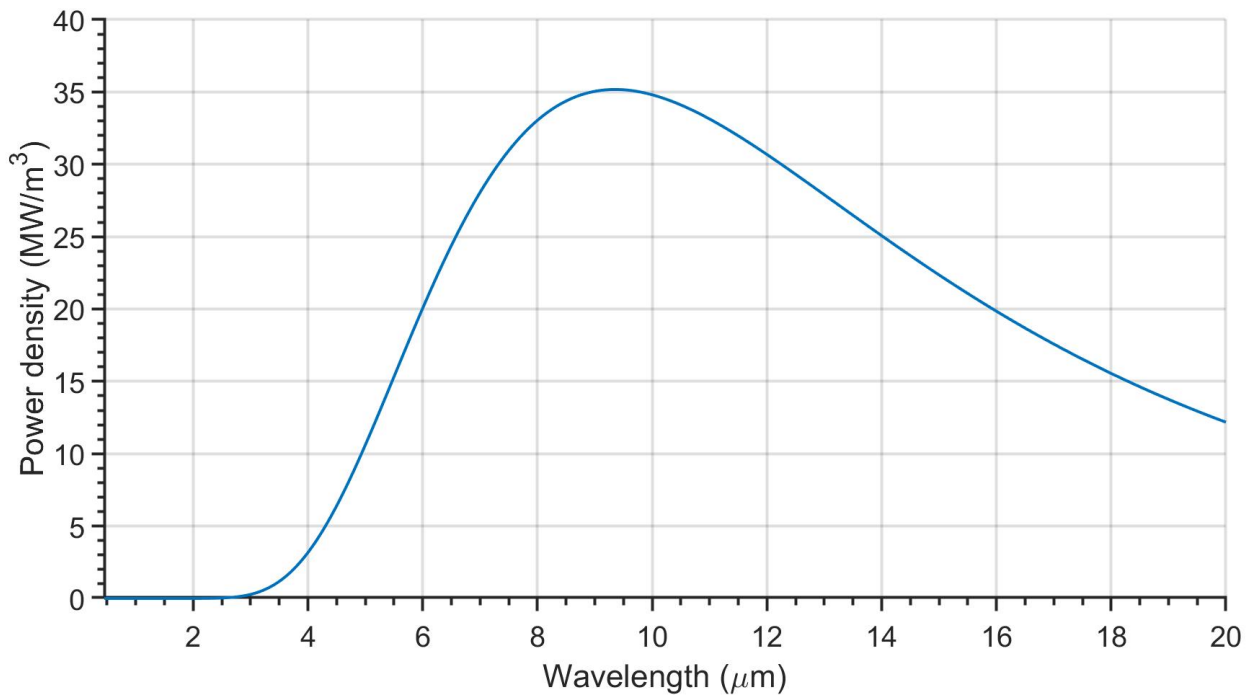
Figure 3: *Human blackbody radiation acquired from calculating the spectral power density of a 37° C object.*

This figure shows that the peak wavelength for the emission from a human is 9.55 μm, for which it is trivial to design a detector with good transmission, as can be seen later in the results.

2.7   Atmospheric windows and imaging contrast

Almost all IR-detection devices require transmission through air, and as such it is useful to look at which wavelengths transmit the best through air. Air consists of several high-absorptivity molecules such as H_2O, CO_2 and O_3, which potentially limits the atmospheric transmission [46]. Many of these molecules are depicted in figure 4. When

designing a IR detection device, one either needs to make an active sensor, which generates its own "background", or a passive device, which just detects what is already in the background. It is in this latter case one has to take into account what radiation is present. The atmospheric transmission at ground level is limited by the molecules shown in figure 4, but certain circumstances that change the concentrations in the air can change the transmission diagram. Larger suspended particles scatter the radiation regardless of their wavelengths, but for smaller particles (compared to the wavelength) however, Rayleigh scattering becomes the dominant mechanism for dispersion. Small particles exhibits higher polarizability, and hence allow themselves to easily interact with larger wavelengths, behaving like a radiating dipole. Rayleigh scattering has a $\frac{1}{\lambda^4}$ dependence on the wavelength. By extending this, one can conclude some useful things about different weather effects.

After rain, the air contains more water vapour, which scatter IR radiation more than air. During a forest fire on the other hand, where smoke and small particles are suspended in the air, IR transmission is higher than that of visible light which allows better visibility. Therefore, studying the environmental conditions surrounding the use cases of IR detection helps deduce parameters for the detector. This has certainly been done before, so no deep study goes into this, but it is important too keep in mind.
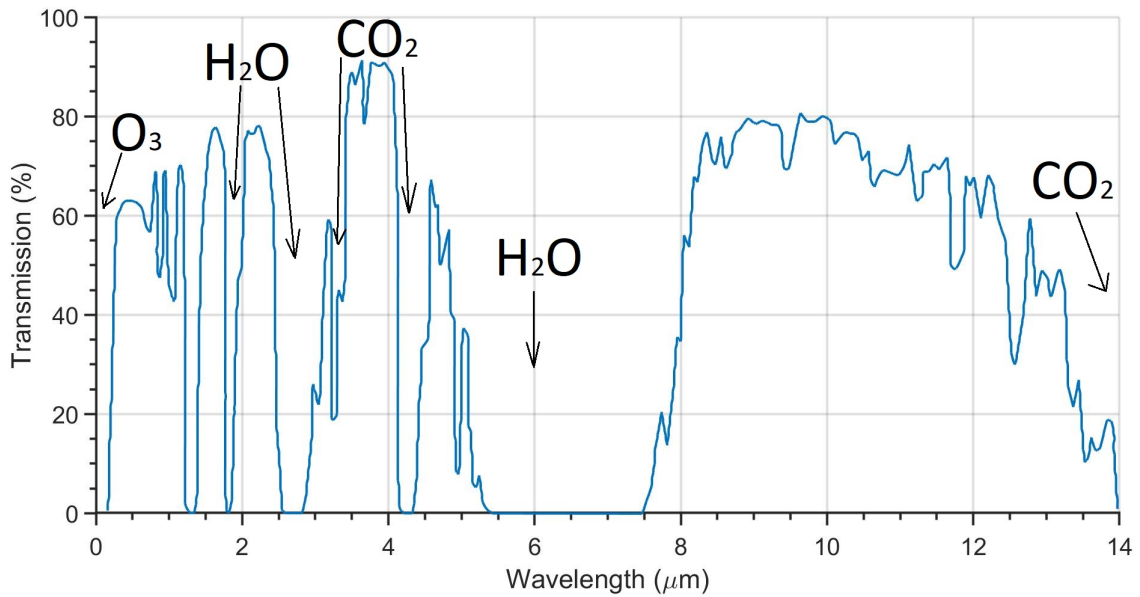
Figure 4: *Solar radiation penetrating the atmosphere and reaching the ground. Including the highly absorbing molecules and their absorption bands. This implies which wavelengths penetrate furtherest in air.*

Another mechanism that should be considered is the imaging contrast attainable when measuring passively in the atmosphere. This can fortunately be calculated by using Plancks radiation law (12). The definition of scene contrast is as shown in (13):

$$C = \frac{\partial W / \partial T}{W} \tag{13}$$

Where:

$$\frac{\partial W(\lambda, T)}{\partial T} = \frac{-2\pi h^2 c^3}{\lambda^6 kT} [exp(\frac{hc}{\lambda kT})]^{-1} \tag{14}$$

Here W is the spectral power density for a given temperature and wavelength range. Solving this equation and plotting for five different temperatures around 270 K yields formula 14, and figure 5 below.
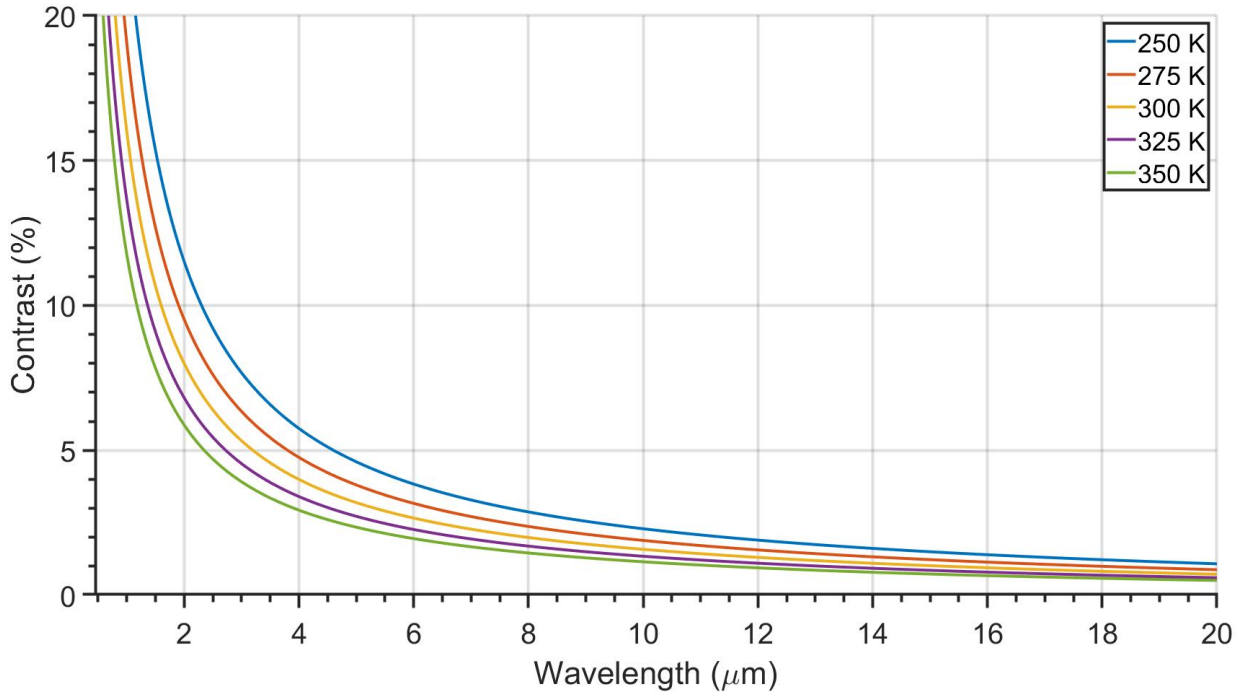
Figure 5: *Calculated scene contrast against background by solving the spectral power density difference of two objects.*

Figure 5 shows that smaller wavelengths are easier to distinguish from each other, as the contrast is higher. A note should be taken of the solar emission spectrum, for which the *shorter* wavelengths are by far more represented, with a peak on green colour (500 nm). A 290 K blackbody radiates 4.1 Wm^{-2} in the 3-5 μm range, but 127 Wm^{-2} in the 8-13 μm range [46]. As a comparison, the radiation measured at ground-level from the sun is 24 Wm^{-2} and 1.5 Wm^{-2} respectively for the same ranges. This implies that distinguishing an object in the MWIR band (3-8 μm) is easier, as the contrast between the object and background radiation is higher [46].

2.8 Anti-reflective methods

Most infrared transmitting materials have a relatively high refractive index. Cadmium Telluride is no different with a refractive index of $n_{CdTe} > 2.70$ for 300K between 0.45-20 μm. [18]. This high index of refraction causes large Fresnel reflection losses. These high losses has led to the development of anti-reflective methods which reduce the reflection. The two most used mechanics to solve this is: layered anti-reflective coatings on the surface - which work by causing deliberate destructive interference in the reflected direction which allows higher transmittance by reducing reflection. The other method is using a *graded* refractive surface, for which the index of refraction will gradually increase from $n_{air} \rightarrow n_{CdTe}$. This would satisfy the transmission mechanics from (4), and theoretically would allow for extremely low reflection. The interference effects from the anti-reflective coating have traditionally been caused by coating the substrate with a material of lower

refractive index, or by stacking alternating low-high index materials. The mechanisms are the same: they deny reflections by destructive interference in the reflected direction. Unfortunately, single layer coatings usually have a narrow bandgap and poorer angular response than the bare CdTe [8], but higher transmission. Multilayered coatings on the other hand, are expensive, and difficult and time consuming to manufacture and develop. Additionally, they can be material-specific, meaning the medium boundaries might not be chemically compatible. Micro-structures in the surface on the other hand, does not have the narrow band-width caveat, yet it has better angular resolution than the base material and they are as chemically stable as the base material - though mechanically vulnerable, as the protrusions are more exposed [19].
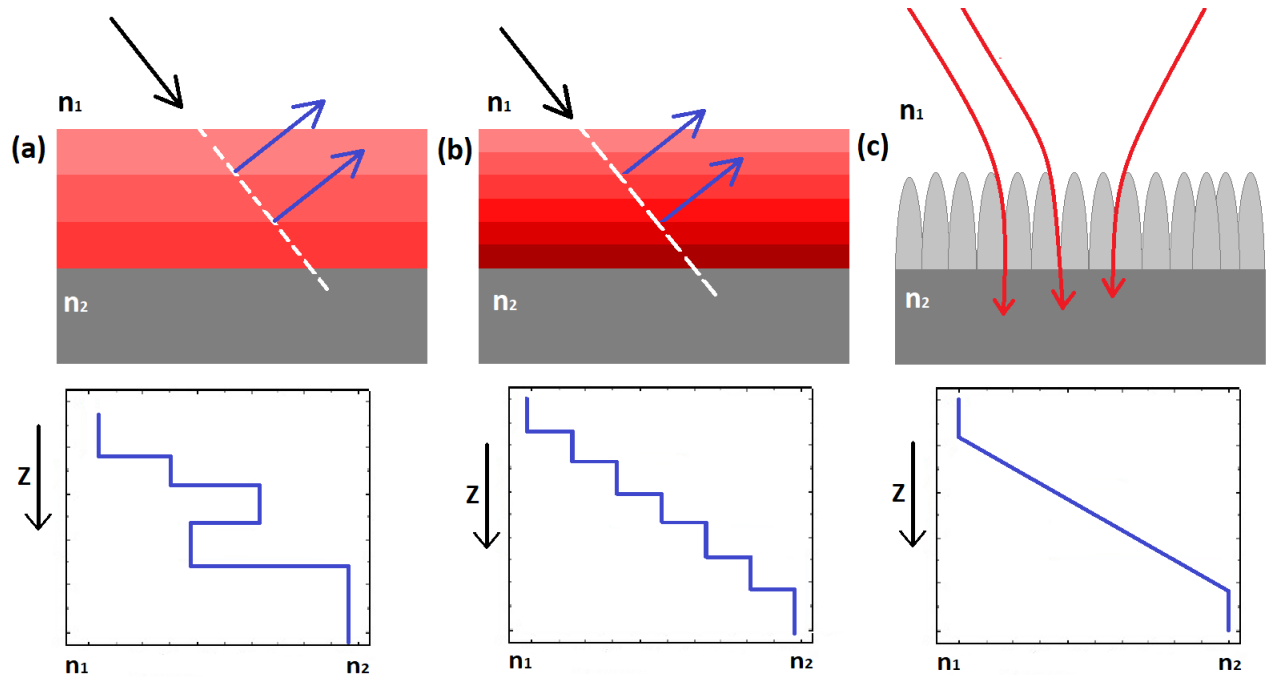
Figure 6: *Mechanisms of anti-reflective methods (Recreated from [8]). Here (a) is a layered ARC with three layers all with alternating high and low refractive indices as indicated by the depth-to-refractive index plot below it. (b) is also a layered ARC but with many more layers, with a graded refractive index, illustrating the goal of micro-structures. (c) is an illustration of moth-eye structures and their high angle of incidence transmission properties.*

Some examples of ARC transmission improvement are: for photovoltaics, just a basic ARC on the glass casing can increase transmission by up to 4.3% [5], potentially improving efficiency from 18% to 18.8%. For lighting fixtures, simple anti-reflective coating on the surface can increase emission by 4.3-8.6%. Even greenhouses can make use of this, by coating the glass panels it can increase transmission in the photosynthesis region (400-700 nm) by 8.6% [5].

2.8.1 Layered anti-reflective coatings (ARCs)

By stacking one or more layers of high and low refractive index materials, one can create an *interference filter*, which causes destructive interference in the direction of the incoming light, increasing transmission directly by preventing reflection [5]. They consist of

either a single layer, or stacks of low absorption coefficient layers, alternating between high and low refractive index. If it only has a single layer, then the coating is chosen from a group of materials with lower refractive index than the substrate, such that the refractive index transition is lower from air to the ARC. For this to work efficiently, the layer is usually tuned to a specific narrow wavelength band, and as such has poorer broadband applications. Additionally, because of the interference effects of the layer, the transmission will vary periodically dependent on the coating thickness.

It is also possible to stack several layers, allowing for custom tailoring of the transmission band. This thesis will focus on single layered ARCs, as multi-layered ARCs are quite complicated to fabricate. These coatings are usually used when the application is narrow-band, or some specific material is preferred. In the Table below some single-layer coatings are presented from the literature. Some of the coatings found in the literature only had a sharp transmission peak, while others had a relatively broad band around the transmission maximum. They are also not all specifically for IR, but are included for comparison.

Table 2: Overview over some modern ARCs, as reported from the literature. Unfortunately, some vendors do not disclose the coating material. (DLC = Diamond like carbon). *vendor has not divulged the coating material. **not IR range but used for illustration of the possibilities.

Substrate	**Coating**	**Range** (μm)	**max T** (%)	**Peak** λ (μm)	**Source**
Ge	DLC	2- 14	97	11.5	[21]
Si	DLC	3 - 5	97	3.8	[31]
$ZnSe$	*	1 - 18	97	5.5	[21]
"VisiClear"	*	0.425 - 0.675**	99.5	0.51	[52]
"Cleartran"	YbF_3	2 - 14	82	8.5	[27]
Al_2O_3	MgF_2	0.4 - 0.7**	99.5	0.55	[42]
Si	SiO	0.4 - 1.1	99	0.74	[39]
Si	CeO_2	0.4 - 1.1	96	0.84	[39]
Si	ZnS	0.4 - 1.1	99.5	0.75	[39]
ZnS	DLC	2.5 - 10	96	2.5	[54]
SiO_2	HMDS & PMMA	0.4 - 2.4	94	0.6	[53]

To tailor the coating to its wavelength one has to optimise the film-thickness to get the most out of the coating. This can be done using the formula described below, which is a geometric method for ensuring that the incoming waves destructively interfere as much as possible with the reflected waves from the substrate; When two materials are layered on each other - lets say oil and water - and they have different refractive index, then the incoming wave will reflect both in the air-oil boundary, and the oil-water boundary. The interference between these waves will be destructive or constructive in the reflected direction, depending on the thickness of the film. A simple illustration is shown in figure 7.
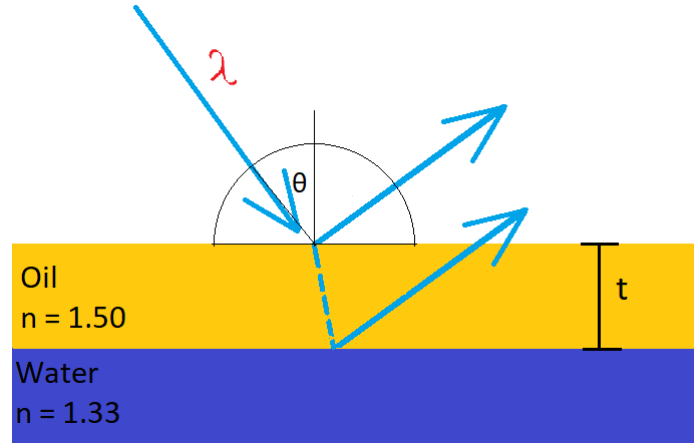
Figure 7: *Single layer thin-film reflection illustration. Even though ARCs here are for normal incidence, the incoming wave is drawn at an angle to better illustrate the situation.*

As the reflection is intended to be destructive, the wave reflected off the oil-water boundary must be *out* of phase with the wave coming from the air-oil boundary. Assuming always normal incidence, the coating thickness is easy to calculate from the well known interference formula $(d * sin(\theta) = m\lambda_n)$ with $sin(\theta) = 1$:

$$t = \frac{m\lambda_n}{2} sin(\theta), \quad \lambda_n = \frac{\lambda}{n}, \quad sin(\theta) = 1, \quad m = 1, 2, 3, 4...$$

Now, if the coating material has refractive index higher than the substrate - in this case it is air - the wave will undergo a phase shift of 180 ° at the interface. So, in this case the integers in m must be shifted by one half period, and one arrives at:

$$m' = m - \frac{1}{2}, \quad m' = \frac{1}{2}, \frac{3}{2}, \frac{5}{2}, \frac{7}{2}, ...$$

So the final formula becomes:

$$t = \frac{\lambda}{2n} \times \{\frac{1}{2}, \frac{3}{2}, \frac{5}{2}, \frac{7}{2}, ...\} \tag{15}$$

This formula describes the thicknesses that have the *least* reflection loss, and allows optimisation for any wavelength as long as the spectrally dependent refractive index is available. For most materials and wavelengths in the IR, this yields a thickness around 0.5-2 μm. Unfortunately, these are thicknesses that are not so easy to deposit on all materials, but some will be presented.

Damage resistant AR methods
One of the drawbacks of ARMS are the mechanical stability of the material surface, as the surface now has more exposed protrusions [19]. The structured surface *must* retain its integrity to function properly, but at the same time is more vulnerable to scratching, deformation, breakage, and contamination than the bare substrate. This can obviously be minimized by using materials known for their abrasion-resistance and mechanical strength. Fortunately, the materials examined here are known for exactly this. Aluminium and silicon oxides are famous for being remarkably damage resistant [19], and so,

Sapphire(Al_2O_3) and Silicon dioxide(SiO_2) are examined for anti-reflection. In addition to these, Diamond-like carbon (DLC) is also examined, as it is an established material within anti-reflective optics, and diamond is well-known to be among the hardest materials. These are all materials known for their high rankings on Mohs scale of hardness(9, 7, $\approx$10 respectively) [47].

ARCs also provide some form of damage resistance, as they protect the substrate from the conditions the coatings are met with. CdTe, for example, oxidises over time in air, forming a telluride oxide layer near the surface [36]. It is also a relatively soft metal, meaning the surface is at risk of abrasive damage. In applications where the sensor is exposed to the elements, this can prove to be a problem. Luckily, several of the anti reflective coatings presented here are also very hard materials, and prove them selves to be both chemically and mechanically much more stable than the substrate. This is some of the motivation behind looking into Silicon Dioxide(7 on Mohs scale of hardness) and Aluminium Oxide(9 on Mohs scale), both of which are used as abrasives because of their mechanical hardness.

2.8.2 Anti-reflective micro-structures (ARMS)

Instead of coating the substrate with a second material, it is also possible to create microscopic structures on the surface, creating a surface with a graded refractive index - this is the purpose of anti-reflective micro-structures. By applying periodic, sub-wavelength structures onto the material, one can improve the transmission properties - direct transmission, angle of incidence and transmission band-width. The inspiration for this comes from nature, where the colour blue is generated almost exclusively by micro-structures. Bio-mimicry is the process of identifying a desired trait or property generated by nature, and then reproducing said ability with the use of technology. A great example are blue animals. Most animals turn a certain colour after consuming relevant pigments, like flamingos turning pink because of the red pigments in their diet - shrimp. There is on the other hand, almost *no* blue pigments in nature. This is because blue makes up the most significant part of the energy budget for photosynthesis, and so almost no plants dare reflect away the precious blue light they need to grow. With a lack of blue pigment one would expect there to be no blue animals, alas, butterflies, spiders, colibris and peacocks all display radiant and clear blue colours, though with a lack of pigment - They display *structural colour* [56], which is when the colour is generated by micro-structures rather than by pigment, as seen in figure 8, where the micro-structures on the wings of butterflies is illustrated.
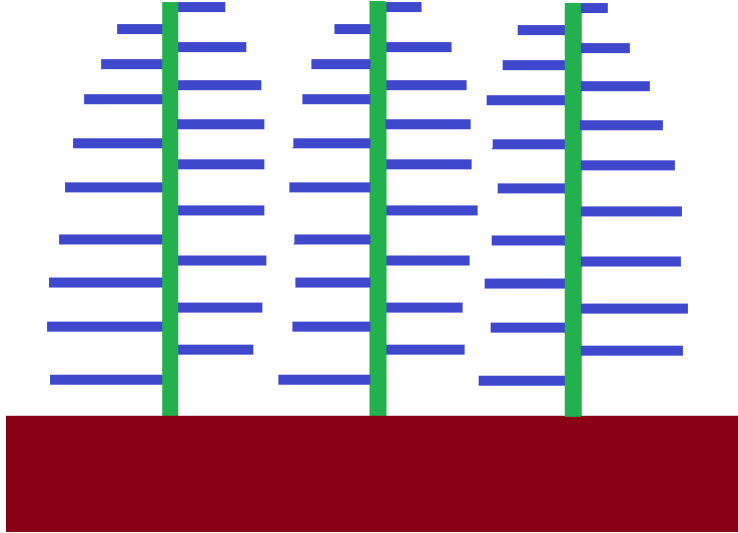
Figure 8: *Structures responsible for generating structural blue in butterfly wings [56]. Though this is not the same effect as ARMS generate, they are both examples of nano-scale effects.*

When the photons come in, only the ones with wavelength close to the distance of the hairs on the trees will be reflected, as they will resonate and interfere constructively with the incoming waves. So the structures work as a reflection filter for only the blue colour. A note to be taken is that the mechanism for these close to mono-chromatic reflections is not the same for transmission optimisation, but serves as illustration of the power of wavelength-sized structures.

There are many advantages of Anti-Reflective Micro-Structures (ARMS), as they do not depend on the bonding and cohesion of different materials like ARCs do, as the structures consist of the same material as the substrate - doing this avoids placing mechanical stress because of lattice parameter mismatch and thermal expansion mismatch, as the lattice constants are identical, causing no mechanical strain because of repeated expansion and contraction (through heating and cooling from the environment). Additionally, the structures improve the omni-directionality of the transmission into the surface, as even low angles towards the surface will see a graded surface, making them better in both broad-band and angle-dependence [15], *and* they minimize surface interference effects which are very apparent in ARCs or with just bare substrate, which will be seen in the results.

The most popular structure for anti-reflection is called *Moth-eye*, and are inspired from the eyes of moths, which are known for excellent night vision [2]. They are a group of geometric protrusions, and are illustrated in figures 10 and 11. For a *basic* moth-eye structure, the most important metrics for the geometry are the base radius, the height and the radius of curvature (ROC). These are correlated mathematically, and they are dependent on the function used to define the moth-eye. In most applications, the moth-eyes are parabolic cones defined by $f(x) = ax^2$, $a \neq 0$, and this is what is used in this thesis, with a = 1. The radius and height are here treated as the free variables, and the ROC is defined through them. The ROC at height y and radius x is calculated from the curvature of a curve, and can be found to be:

$$p_0 = \left(\frac{y''}{(1 + (y')^2)^{\frac{3}{2}}} \right)^{-1}$$

$$p_0 = \left(\frac{1}{2} + 2x^2 \right)^{\frac{3}{2}}$$

Where p_0 is the ROC. The geometry of the cones are here defined only using the base radius, the height, and their distance from each other, so the ROC is not necessary for this thesis, but as they are used quite a lot in the literature, they are included.

Another very useful metric is the packing fraction (PF), which can be calculated from the relationship between the area of a hexagon, and seven circles in a plane as seen in figure 9. This will be used to calculate the gradient for the refractive index by calculating an average *effective* refractive index from the height-dependent packing fraction. The foundation of this method is based in the *effective medium theory* [15], which states that the effective refractive index of a mixed medium can be calculated by summing up the constituent indices for each material. For moth-eye structures for example, the "mixing" occurs between the pillars, where the effective index would be the weighted sums between the CdTe pillars, and the air gaps between. Setting up a hexagonal area centered on a pillar, and all corners in the centres of six other pillars, the area can easily be extended to define the whole ARMS structures by arranging these areas in the plane:
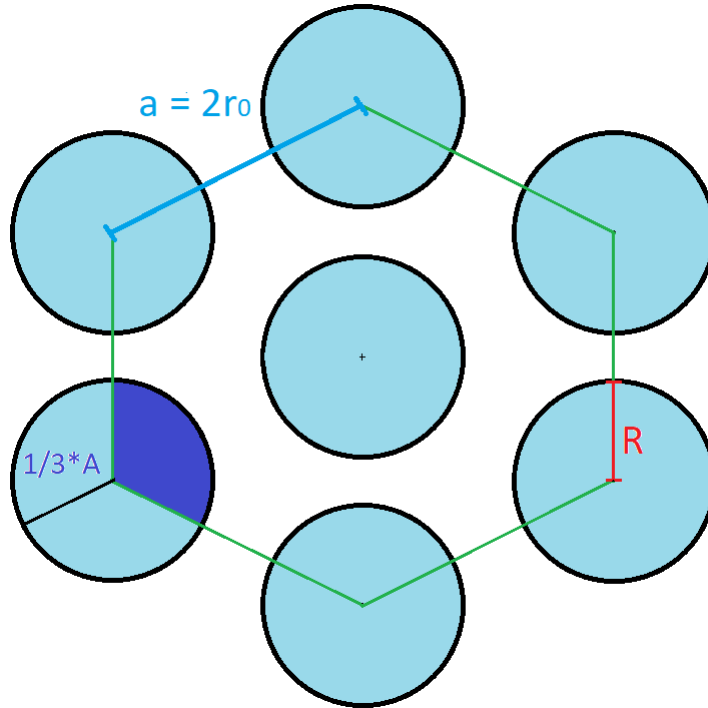
Figure 9: *Packing fraction for hexagonally arranged pillars with tapering radius.*

The area of a single circle and the area of a hexagon are respectively:

$$A_p = \pi R^2$$
$$A_{hex} = 6\sqrt{3}{r_0}^2$$

With a equals to the radius of the base of the pillars, R equals the height-dependent radius, which is r_0 for h = 0. From figure 9, it can be seen that one whole pillar, and six one-third pillars are encompassed by the hexagon, meaning a total of 3 pillar areas inside the hexagon. The packing fraction is therefore:

$$PF = \frac{3A_c}{A_{hex}} = \frac{\pi R^2}{2\sqrt{3}{r_0}^2}$$

This can be solved for the height of the pillar, by acknowledging that from the definition of this parabola, that $R = \sqrt{h} =>$

$$PF = \frac{3A_c}{A_{hex}} = \frac{\pi h}{2\sqrt{3}{r_0}^2} \tag{16}$$

This can be used to calculate the *effective* refractive index per height. The index of refraction of a mixed material, such as an interface between air and moth-eyes. The effective refractive index is the weighted sum of the material areas in the plane, per height, this sum was calculated in (16). The effective index for the moth-eye boundary between substrate and ambient is therefore:

$$n_{eff} = PF * n_{sub} + \bar{PF} *_{ambient}$$

With $\bar{PF} = 1 - PF$. A plot of the gradient is presented below. This was done by letting $R^2 = $ h scale from 0 to its maximum height/radius:
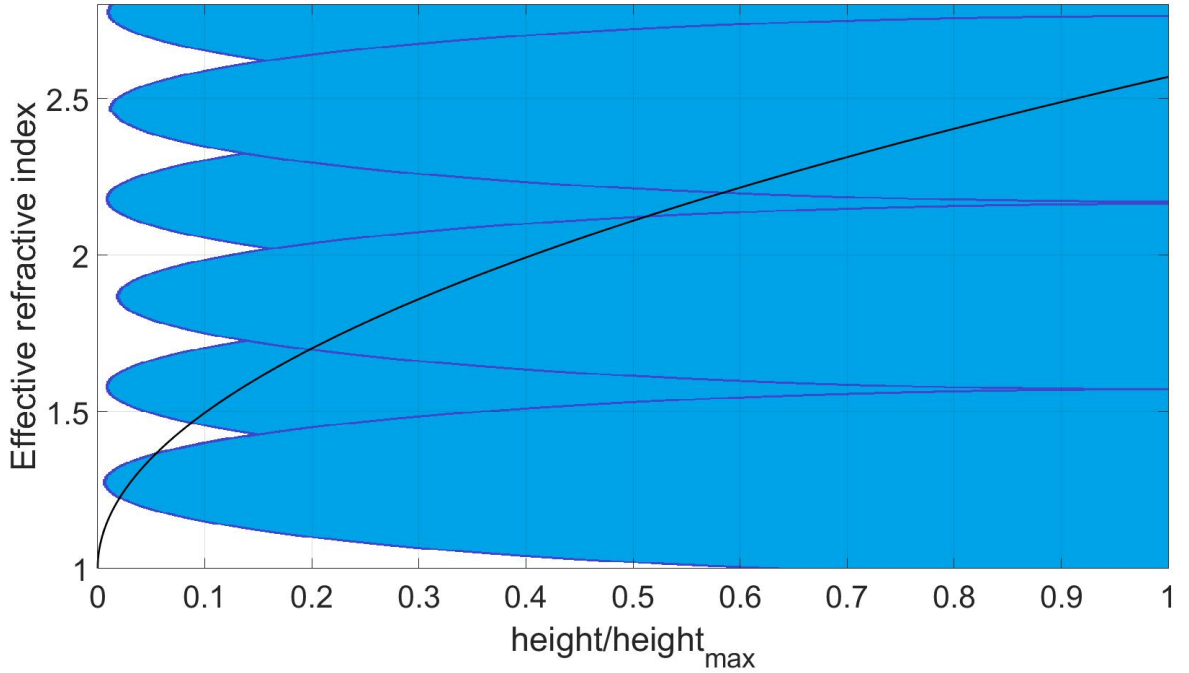
Figure 10:   *The effective refractive index for $(y = x^2)$ parabolic Moth-eyes, with $n_{ambient} = 1$ and $n_{substrate} = 2.73$ used as examples*

There are several different types of nano-structures one can choose from when designing an anti-reflective surface. This thesis will only follow up on Moth-eye structures, but it could be helpful comparing with others:

Moth-Eye: Moth-eye nano structures are inspired from the pillars on the surface of the eyes of nocturnal moths. These pillars provide a smooth gradient to the refractive index between air and substrate, and thus should as the theory describes be a low reflection surface. Typically, the pillars can be either truncated cones (1), rounded cones (2), or anti-moth-eye (3). All these structures will be investigated, and presented in the results.
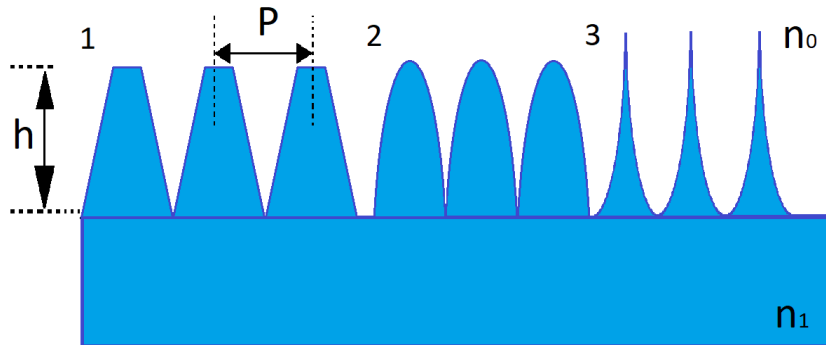
Figure 11:   *Different examples of what constitutes moth-eye AR structures. The first ones are called truncated cones, the second are referred to as rounded parabolic cones, and the last structures are either inverted moth-eyes, or spikes*

Sub-Wavelength Structures: Another structure technique for anti-reflection is by fabricating very small and dense posts, or holes in the surface. These *sub-wavelength*

structures are more like an array of posts or holes which provide anti-reflection by tailoring the effective index of refraction in the surface. This is done by manipulating the texture fill factor [25] - the relationship between open areas to solid material - by either making the posts/holes wider, or by packing them closer together. Then the structure height is set to be one quarter-wave optical thickness at the effective index [25]. Far more complicated structures can be made with dual and triple-band anti reflection performance by further deepening the structures and introducing more complexity, but the standard post design works by halving the boundary refractive index gradient, and the posts serve as higher surface area, which helps in omni-directionality. This structure is omitted from this thesis, as its predictions for transmission are lower than for moth-eye and colloids.

Figure 12: *Sub-wavelength post illustration. Here the holes effectively halve the effective refractive index in the surface, if the posts and hole are of the same sizes. This size relationship can be changed to tailor the effective refractive index.*

Colloids: An easier method of depositing micro-structures is by embedding spheres of high transmission material into the substrate, as illustrated in figure 13 below. The colloids only needs to be deposed and embedded in the substrate, and so could provide it self to be a cheaper and easier solution. As opposed to micro-structuring which requires a complete and difficult process. The literature presents good short-band results, and serves as proof of concept [3, 22, 23]. These structures are included in the results and discussion, as they seem to be a cheaper method of achieving *some* anti-reflection.
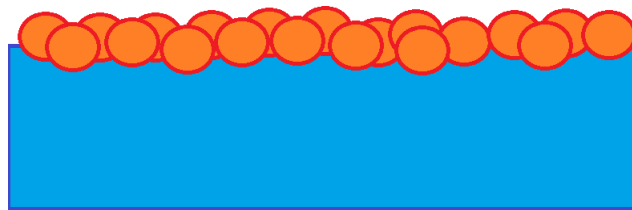
Figure 13: *An example of embedded colloids in substrate to generate both a graded refractive surface, and possible an anti-reflective coating. The colloids are deposed onto the surface and hence the substrate and the colloids do not overlap much.*

Random Texture AR Microstructures: A very similar approach as the Moth-eye, the random textures provide better broadband transmission, and lower interference and diffraction. This method uses a statistical distribution to make pillars similar to the moth-eyes, but with heights and widths randomized within the distribution. Because of the lack of periodicity, interference effects are reduced. Random-textured moth-eye structures have theoretically roughly the same transmission as standard moth-eye structures. Unfortunately, these structures are not included in the results, as drawing them

in a simulation program is quite time consuming. They are on the other hand, predicted to perform somewhat better than for normal ME.

n_0

h

n_1
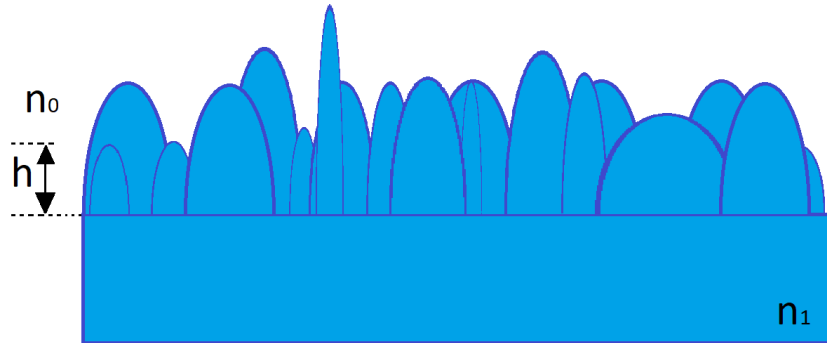
Figure 14: *Random texture structure illustration*

Nano-rods: A relatively new method which fulfils many of the same design characteristics as moth-eyes are deposition of nano rods. These can arguably be applied by simpler methods, and generate some of the same gradient refractive index, though often with a sharper curve. For nano-rods, as the structures aren't tapered them selves, it is the distance between the tops which help define the curve of the gradient to the index. Alternatively, the structures can be deposed at an angle, generating a little smoother curve, and leading to new angle-of-incidence effects. Unfortunately, these structures are not studied in this thesis.

n_0

h

n_1
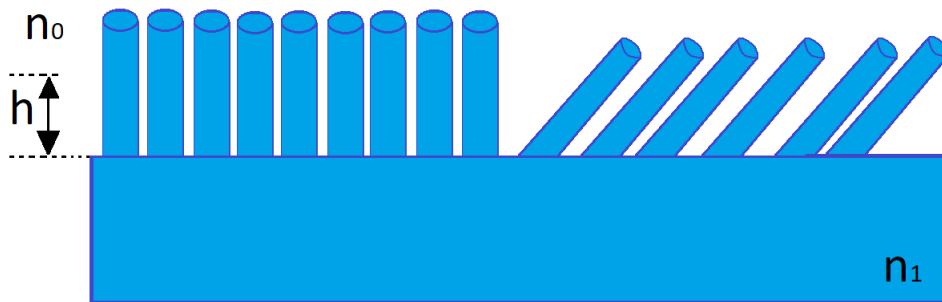
Figure 15: *Illustration of what nano tubes in the surface might look like. They can be normal-facing, or tapered at a certain angle.*

All of these structures have their own unique effective refractive index gradient, as well as some unique surface characteristics. It must be noted that the *exact* gradients for the refractive indices is dependent on the exact geometries, and so, the tapered cones for example, with a smaller top radius, would start from a lower refractive index.
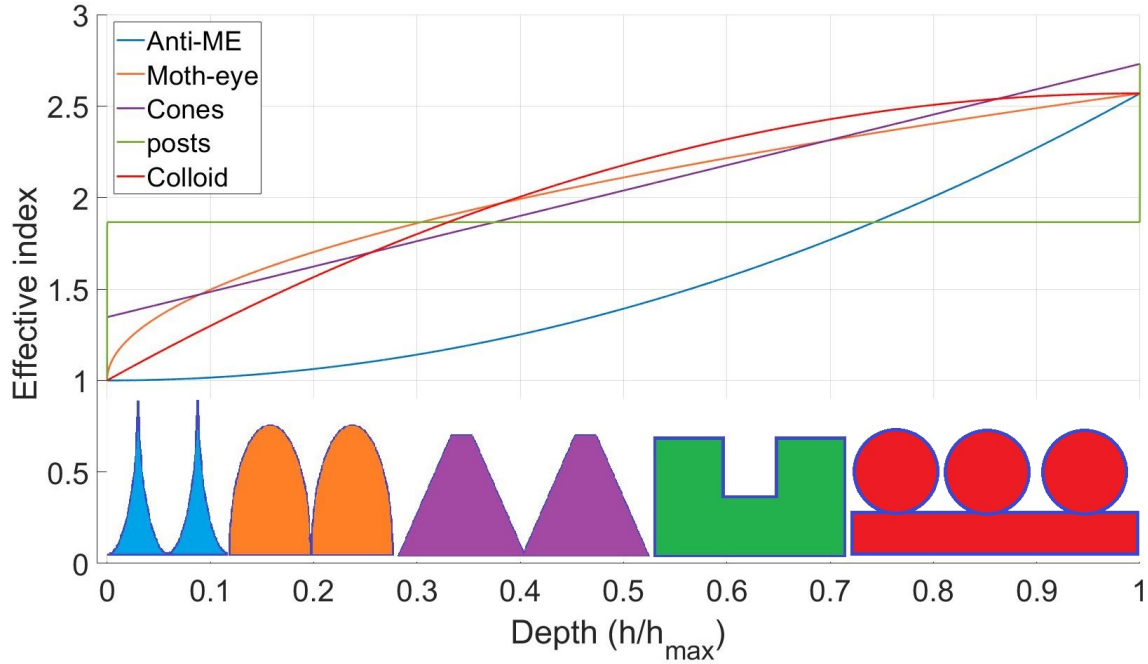
Figure 16: *Effective refractive index of the four most common geometries for ARMS, and an experimental method (colloids). Using the CdTe-air boundary ($n_{CdTe} \approx 2.63$ and $n_{air} = 1$) as examples for the refractive indices. Here the coating and substrate consist of the same material.*

Now, following the theory, some things can be said about the most important input parameters of the simulations - the radius and heights of the micro-structures. As figure 16 is normalized to a unit depth size, it does not illustrate the fact that the height of the structures determine the magnitude of the gradient at any point. A 7 μm high structure clearly has a smoother gradient than an identical but 1 μm one. In addition to this, the height versus wavelength relationship has a large effect on the bandwidth of the transmission. Short structures will not work as an AR for long wavelengths, as the waves will be too large to "perceive" the AR mechanism. This strongly suggest that the gradient will have slightly different shapes for different wavelengths, and become less "graded" for longer wavelengths.

Now, the radius on the other hand, will instead affect the packing fractions in different ways, and therefore affect the curve of the gradient. The different geometries can be viewed just as different radius relationships, and from figure 16, the different curves can clearly be observed. Now, if one holds the geometric shape constant and only varies the radius, the differences would not be dramatic as long as the sizes are within the size range of the wavelengths.

It should be noted that it seems that colloids have a smoother gradient than moth-eyes, but this can be misleading. The gradient for the two structures for the same height is indeed in the colloids favour, but one must remember that the moth-eyes are often much taller than the colloids, causing the gradient curve to be distributed over a typically much longer interval, than for colloids, yielding a generally smoother gradient for a typical moth-eye, compared to colloids when displayed in a truncated range as in figure 16. A complete figure containing all the relative gradients will be presented in the results containing all the proportional curves.

25

2.9   Fabrication and process techniques

One of the drawbacks of the materials discussed here are the expenses when it comes to production of high-purity single crystals. Luckily, high-quality bulk material is readily available from commercial vendors, though at a relatively steep cost. A lucky student can now acquire 6N (>99.9999%) [49] purity CdTe crystals, and in many cases even greater purity (9N), if one excluded the carbon, nitrogen and oxygen content.

2.9.1   Fabrication of CdTe bulk crystals

The production of CdTe in bulk crystals has not necessarily become easier, in spite of the technological advances in crystal growth. In of its relatively moderate melting point, and vapour pressures if its components, the growth of the crystal it self proves to be difficult [49]. An incredible amount of effort has been put into characterisation of the three phase diagrams of Cadmium Telluride - Temperature vs. composition (T-x), pressure vs. temperature (P-T), and lastly its full phase diagram (P-T-x) is assembled. Understanding its phase-diagram is imperative for the controlled crystal growth of CdTe. The stoichiometry of the crystals is *heavily* dependent on deviations in its growth, and hence affects the semiconducting properties of the finished crystal - and as such - heavily affects its optical properties [49].

In summary, just about all techniques of growth of semiconductor material has been applied to CdTe, yet only some specific methods are in use [49]. Roughly, the methods can be divided into classes: Stoichiometric- (melt-growth), and off-stoichiometric melts (solution growth). Vapour growth by sublimation or by chemical vapour transport, and lastly solid state growth. These will not be described in detail here.

2.9.2   Anti-reflective coatings

Coating a substrate with a new material requires material specific knowledge to make sure that incompatibilities are avoided. HgCdTe (MCT) for example has weak Hg-bonds, and so by applying heat to the material, the Hg atoms will begin to migrate and separate, meaning special considerations must be put into the process. The lower boundary for coating techniques for HgCdTe is 170°C, which is very low compared to most techniques. Fortunately, very few materials are as demanding as HgCdTe. CdTe is more forgiving. Still, some oxidation effects of Te has been observed [36], which are only accelerated at higher temperatures.

For each combination of materials, care should be taken into *which* deposition method is used, and as expected, there are *many* of methods: sputtering, sol-gel method, chemical vapour deposition (CVD), physical vapour deposition (PVD), atomic layer deposition (ALD), filtered cathodic vacuum arc, molecular beam epitaxy, thermal evaporation deposition, electron beam evaporation deposition, and pulsed laser deposition.

2.9.3   Anti-reflective micro-structures

There are many ways of creating microstructures into the surface of a material, and so only a few will be discussed here.

An easy and robust technique to print specifically moth-eyes or pillar-like structures is colloidal lithography. This method involves coating or deposing *colloids* - uniformly sized

spheres - of a different material (often silicon), which is used as an etch mask for the surface. The micro-structure resolution is then only limited by the mask-sizes, which can be in the nano-meter scale [9]. This technique allows for remarkably complex structures [9], but it is only the moth-eye-like pillars which are interesting for this thesis, so the method for these will be taken account of. *Monodisperse* (single-size) microspheres have the property that they self-assemble to single layers with a hexagonal close-packing (hcp) [55], which can be dispersed by capillary forces using a solvent, which later evaporates. This allows for even spacing of the spheres in the surface. As the sphere position will define the pillar distancing and width, this spacing is important to get precise [55]. There are several techniques of getting the sphere crystallization technique just right, like dip-coating, spin-coating, epitaxial growth, and many more Chan1. After the spheres are deposed on the surface, then etching is applied. This, too has several different techniques with different outcomes. The colloids act as shields for the substrate, and as such, all substrate that is in line of sight from the etch "gun", will be evenly etched away. A simple illustration is shown below in figure 17.
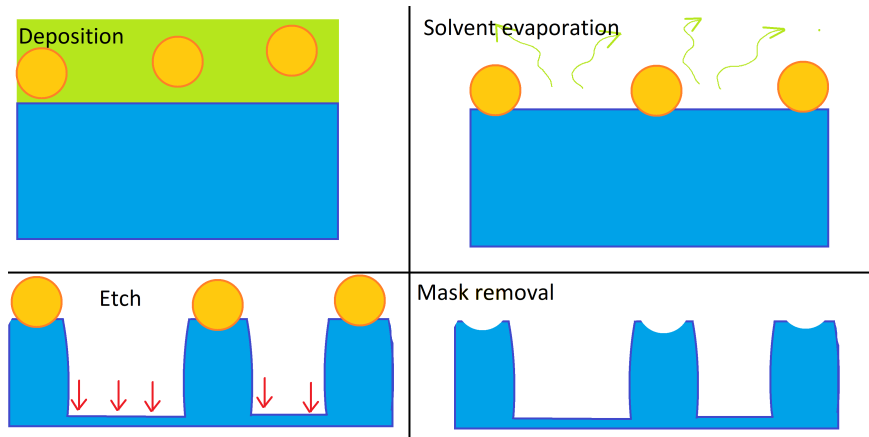
Figure 17: *Simple illustration of colloidal lithography process. The colloids are arranged by surface tension while submerged, then the solvent is removed. Then the reduction-process is performed which removed material, then finally the colloids are removed.*

2.10   Lumerical FDTD solver

To analyse the transmission for different materials and AR methods, a simulation package was used - namely Lumerical. This package was selected as the software has the capabilities of simulating in the FDTD (Finite Difference Time Domain) - which is a method of discretizing a time evolving process, such as propagation of EM waves. This means that Lumericals FDTD solver can predict how EM radiation propagates both in media and how they transfer through their boundaries [24]. This is extremely useful when solving Maxwell's equations for complex geometries such as micro-structures, as it allows a discrete solution for a continuos problem. The solver works by first solving Maxwell's curl equations in non-magnetic media:

$$\frac{\partial \vec{D}}{\partial t} = \nabla \times \vec{H} \rightarrow \tag{17}$$

$$\vec{D}(\omega) = \epsilon_0 \epsilon_r(\omega) \vec{E}(\omega) \rightarrow$$

$$\frac{\partial \vec{H}}{\partial t} = -\frac{1}{\mu_0} \nabla \times \vec{E}$$

With D, H and E as the displacement, magnetic and electric fields respectively. The $\epsilon_r(\omega) = n^2$ is the complex relative dielectric constant for the media in question, and n is the refractive index. It is assumed that in Ampère's law (17) that there are no free charges, and hence $J_f = 0$. This system is solved for a 3D structure, which will have six EM field components: E_X, E_Y, E_Z and H_X, H_Y, H_Z. If it is now assumed that the structure is infinite in the z-direction, and that the fields do not depend on z. That is:

$$\epsilon_r(\omega, x, y, z) = \epsilon_r(\omega, x, y)$$

$$\frac{\partial \vec{E}}{\partial t} = \frac{\partial \vec{H}}{\partial t} = 0$$

Then the equations are split into their transverse magnetic (TM)(E_X, E_Y, E_Z), and transverse electric (TE) (H_X, H_Y, H_Z) components. For the TM, for example, the system is this:

$$\frac{\partial D_y}{\partial t} = \frac{\partial H_y}{\partial x} - \frac{\partial H_x}{\partial y}$$

$$D_z(\omega) = \epsilon_0 \epsilon_r(\omega) E_z(\omega)$$

$$\frac{\partial H_x}{\partial t} = -\frac{1}{\mu_0} \frac{\partial E_z}{\partial y}$$

$$\frac{\partial H_y}{\partial t} = \frac{1}{\mu_0} \frac{\partial E_z}{\partial x}$$

The method then solves these equations on a discrete spatial and temporal grid - a Yee grid - which is basically a cube with the positions and directions of the magnetic and electric fields at each vertex, as can be seen in figure 18 below.
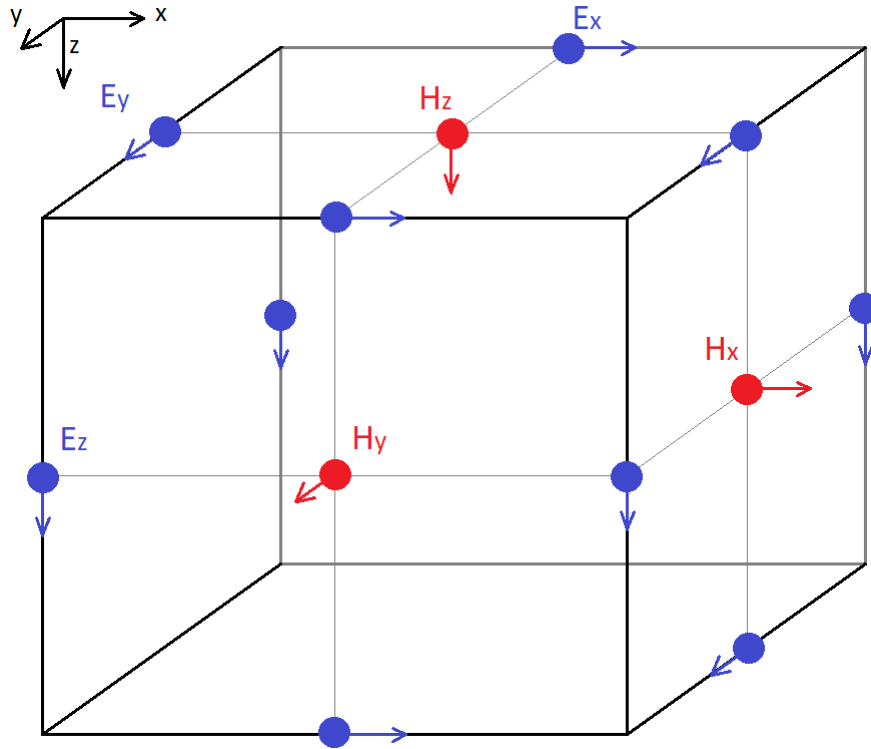
Figure 18: *A simple Yee grid where the magnetic vectors are the centre of the faces of the cube, and the electric vectors are on the edges of the cube. This is a method of discretisation for the FDTD method.*

After the values of each grid point is calculated, its value at the origin of the cube is interpolated so that the calculations acquiesce in the same point. To generate the Yee cells, the FDTD method uses a Cartesian style mesh which is automatically generated. The resolution of this mesh can be manually selected for higher spatial resolution, but with a steep trade-off in computation demand. Typically, Lumerical auto-generates a dynamically sized grid [24], depending on the structures in the grid itself, and this option is used. This was attempted, but this could sometimes dramatically increase the RAM requirements and the simulation time. It must also be mentioned for the results, that the transmission and reflection monitors calculate the solutions to the above problem *separately*, meaning that summing the values recorded in both monitors would not necessarily equate to 1. Some can be explained by absorption, but in several points, the sums are greater than 1: T + R + A > 1.

2.10.1   Index of refraction data

To solve Maxwell's equations, one needs to know either the spectrally dependent index of refraction, or the permittivity and permeability values. All of the data sets used here are extracted from data sheets from vendors [28, 30, 40, 41], from material databases [38], or from handbooks on optical constants [33]

2.11   Atomic-force microscopy

Atomic-force microscopy is a relatively easy, but extremely effective method of acquiring the surface topology of materials. It works by gracing a sharp tip over a surface, recording

the height of said tip. This creates an array of vectors containing the heights of each point on the surface. The needle is so light and the cantilever so sensitive, that the forces causes the cantilever to pivot towards the surface. A laser is mounted such that the cantilever acts as a mirror, and the pivot of the cantilever causes the laser focus to be shifted. The laser is reflected off the cantilever onto a target which works as a detector, which will measure the X-Y coordinates of the laser focus. An example of the images one can acquire can be seen in below. Figure 19 contains some aligned (in the plane), and reconfigured AFM data. The data needs to be realigned after the measurement as the substrate might be on a slope, for which post processing can compensate. A grey scale figure can also be seen in figure 20, for which a line can can be taken of the surface. The topology along this line can be seen in figure 21.
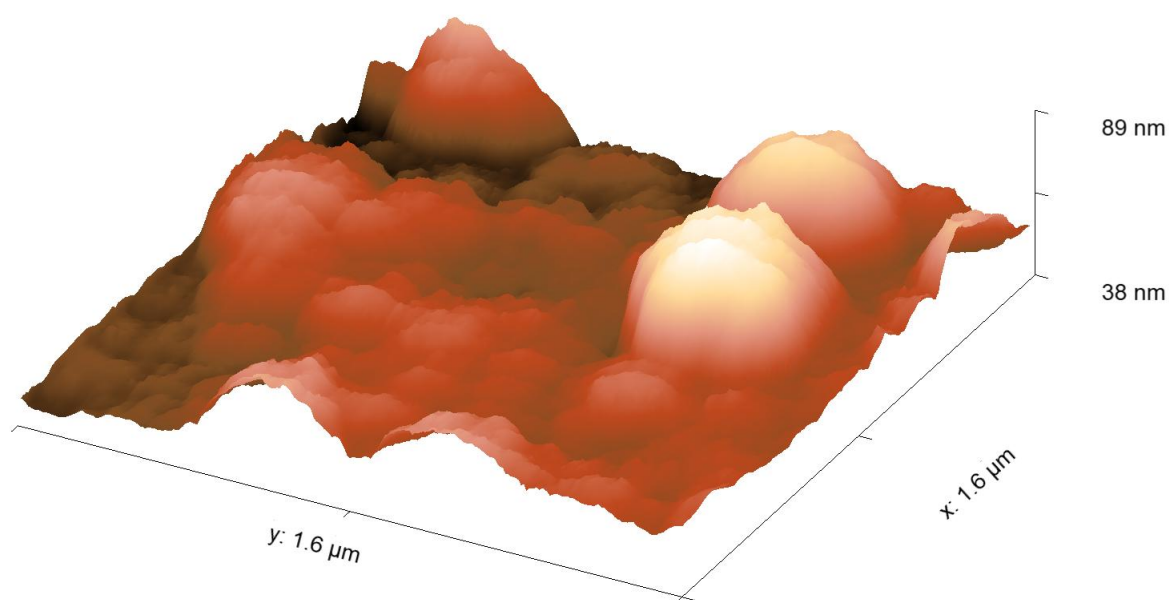
Figure 19: *Surface topology of a substrate for illustration.*

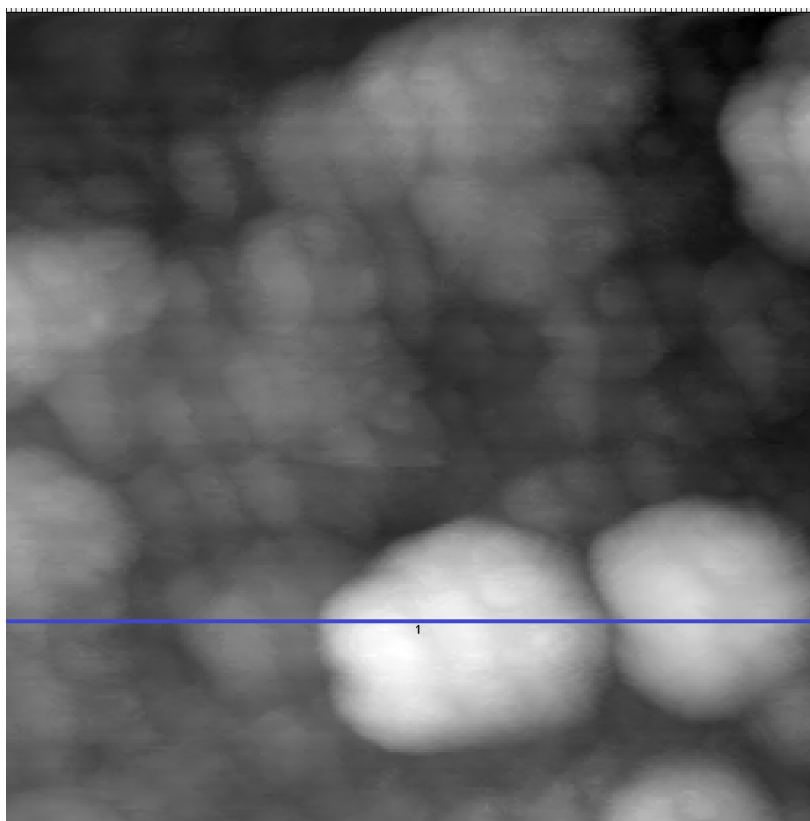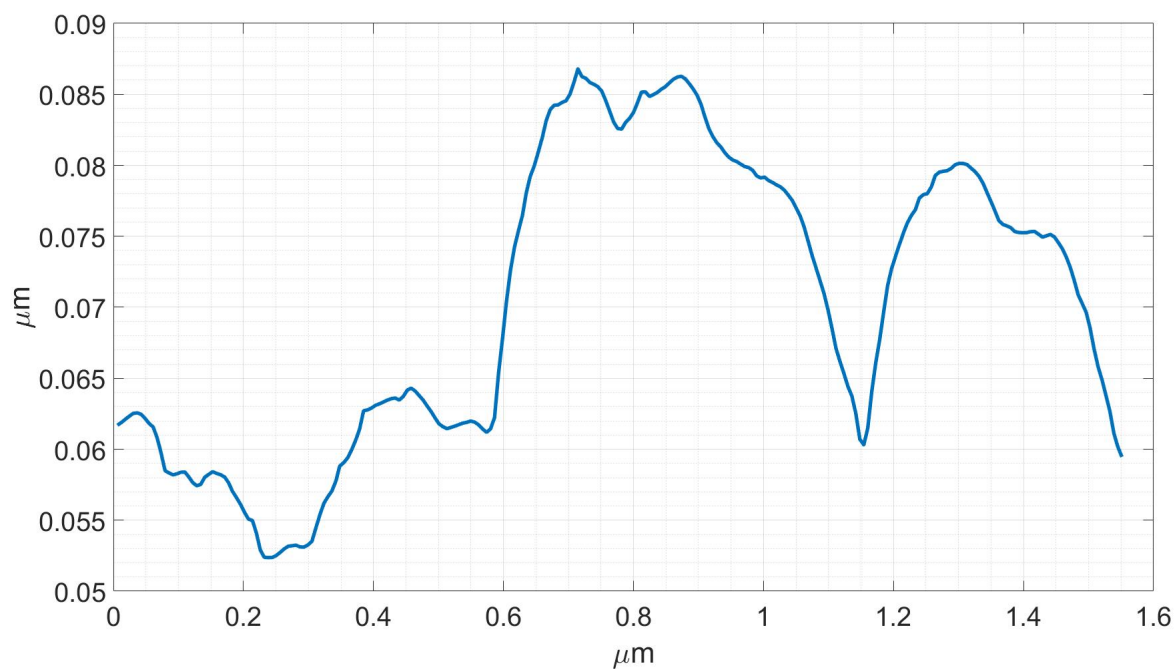**Figure 20:** *Surface of substrate in 2D.*

Figure 21: *Height profile of substrate along the blue line in the figure 20 above.*

The AFM has several different modes of scanning. Namely contact and non-contact mode, and static or vibration mode. Non-contact mode is the "safest" mode, as it will not affect with the surface in any way. In contact mode, the AFM needle will physically

be in contact with the substrate, which can give clues as to the composition of the surface (whether it is hard, sticky, soft and so on). In addition, one can turn on vibration mode, which will oscillate the needle close to the surface (in non-contact), and the amplitude differences will generate the height data. When in contact *and* vibration mode, one can generate a phase diagram of the vibration and the cantilever response, yielding even more data on the mechanical properties of the surface.

2.12   FTIR - measuring the transmissivity

Modern anti reflective technology allows transmission upwards of 99%, so when analysing the transmissions of these materials, a reliable and precise method is required. In this thesis, the FTIR apparatus was selected for measuring the most important characteristic for the detectors in question - namely the transmissivity. The Nicolet iS50 FTIR Spectrometer at the Departement of Chemistry was used for this purpose. The basics of a FTIR apparatus can be seen in the figure below. Rather than shining monochromatic light through a sample, as most other transmissivity measurements are made, an FTIR works by first having a broadband source emit into a interferometer. Using a moving mirror and a beamsplitter, the interferometer can control which frequencies constructively or destructively interfere when recombined in the beamsplitter. The constructively interfering frequencies are then guided towards the sample, and their transmission through the sample is measured. The measurements are performed in the time-domain, and hence must be (Fast) Fourier transformed to acquire the transmission data of the material.
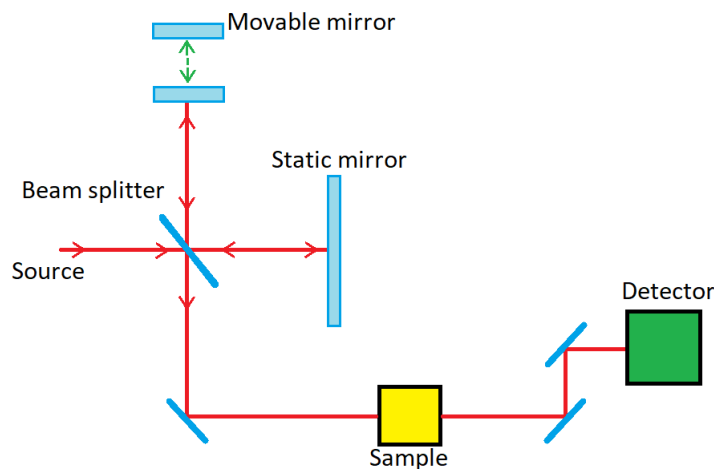
Figure 22: *A course illustration of a FTIR apparatus. The moving mirror controls the interference effects originating in the beam splitter.*

2.13   Effect of surface roughness vs. smoothness.

When designing materials in Lumerical, the surfaces of the shapes are - unless specified - unrealistically smooth (completely smooth). This is clearly not a good representation of a real world metal surface. Even after high quality polishing of real crystals, the surface will still have microscopic grooves and valleys, as seen in the AFM figure 23. The surface illustrated has a root-mean-square (RMS) for the structure height of 14.1 nm [48]. The RMS of a surface is one of the two parameters needed to represent a rough surface, as

it is described by a Gaussian distribution. The other parameter is the correlation length which defines the correlation between the heights of the structures.
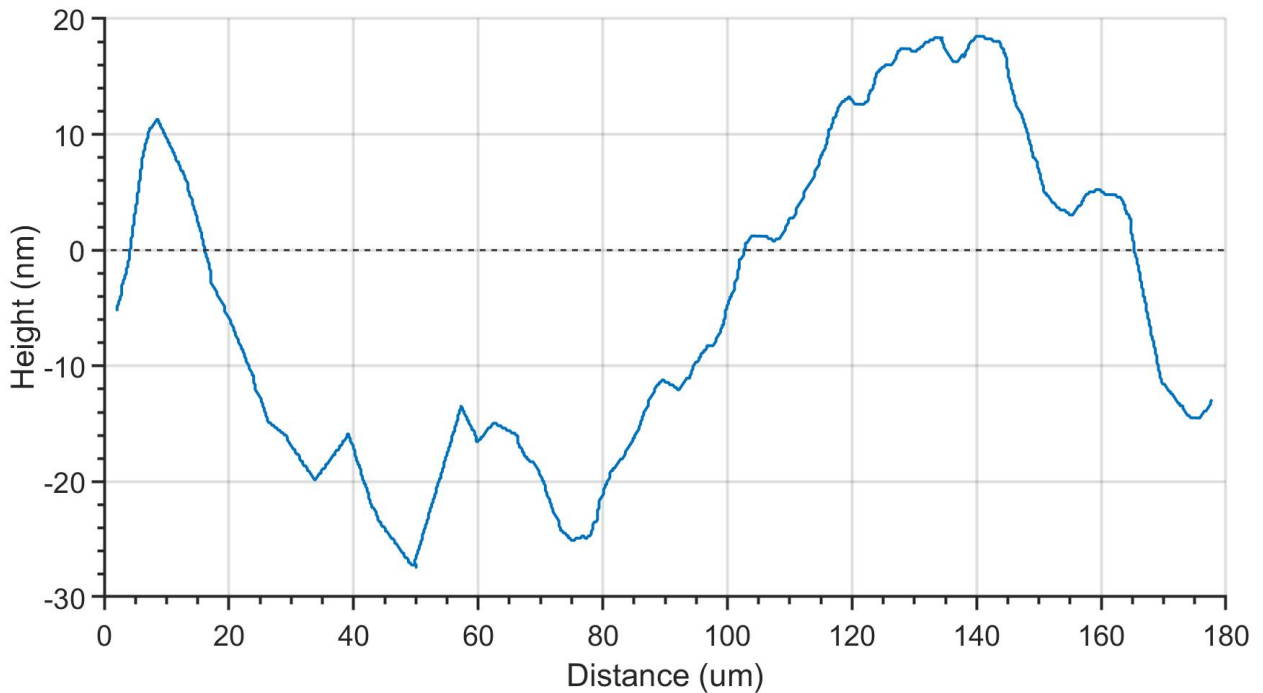
Figure 23: *Surface profile of a CdTe surface after polishing. Recreated from [48].*

As a rougher surface would have a somewhat smoother gradient to the refractive index, one would expect the EM transmission to increase slightly with higher roughness, and this has been confirmed in a number of texts [7, 34]. Applying the theory from earlier, the gradient of the index of refraction of a rough surface will be lower than for a smooth surface, as the protrusions will slowly increase the index almost linearly (depending on the curves of the structures) from $n_1 -> n_2$, instead of it being a steep leap, as seen in the figure below. The smoother the gradient, the higher the transmissivity of the material. This is the main principle behind nano-structured surfaces, and is illustrated in figure 24
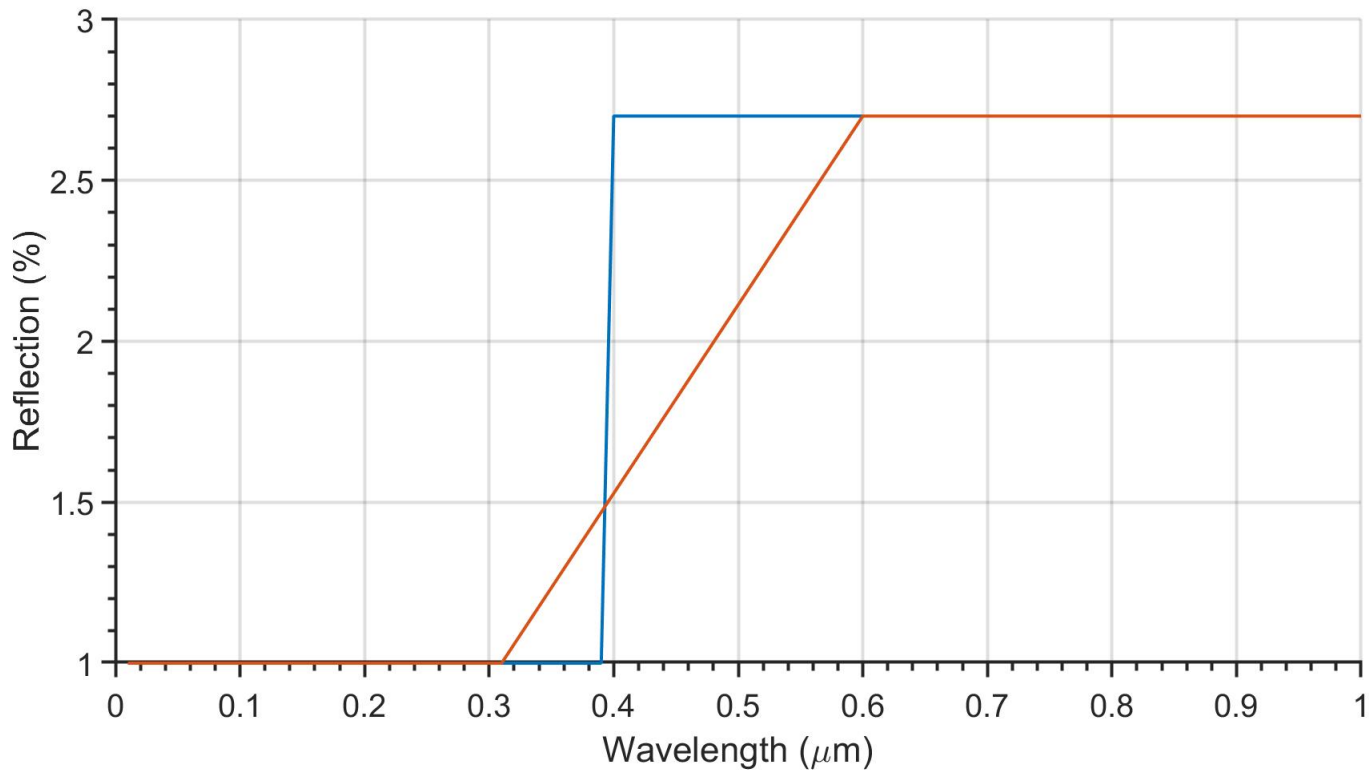
Figure 24: *Index of refraction gradient for smooth vs. rough surface. The gradient here is not precise, and this only serves to illustrate the difference only a little roughness can make.*

Even after polishing a surface with the best of efforts, one cannot avoid nanoscopic surface roughness. This roughness will contribute to diffuse reflection, and pseudo random interference patterns. Additionally, the surface will have more wavelength dependent transmission and reflection based on the relationship between the feature sizes in the surface and the wavelengths. Following the theory on mechanisms for EM transmission, a rough surface will have a slightly smaller gradient in the refraction index, thus allowing slightly more transmission into the substrate.

3   Methods

This section describes the methods used during this master thesis. To begin with, the simulation setup is examined, which is mostly identical for the bare, layered and nano-structured substrate. Then the fabrication method for the ARC and ARMS are examined, and lastly the experimental setup for measuring the transmissivity of the different materials.

3.1   Simulation setup

The simulations were set up in Lumerical as a simple source-target setup, as seen in figure 25 below. The simulation window contains the FDTD environment boundary, the target material, two 2D EM monitors which measure the relationship between the source output and the monitor input in percent, the EM source, and lastly a movie monitor which allows one to record the EM radiation traversing the simulation boundary, and view it in playback. The FDTD boundary ensures that only the relevant objects are included in the simulation calculations, such that no excess computation is performed. The source is set up to produce a plane wave, moving towards the target at normal incidence. The simulation boundaries were set as periodic in both the X and Y plane so that diffuse reflection is not lost by collision with the simulation boundaries, as this will account for some of the surface refraction. The periodic property will emulate an infinite array of the simulation setup, which would be the case in a real world detector, where the surface would likely be of much larger sizes. The boundaries in the Z direction (along the EM radiation) is set as a Perfectly Matched Layer (PML), which *perfectly matches* the amplitude of the EM radiation within the simulation, so that it is perfectly absorbed. This is so that all radiation that has passed through the monitors are absorbed properly to avoid counting a photon twice and false readings of interference effects due to back-reflections. The simulations were setup and run on a home computer with the specs presented in table 3.

Table 3: Specifications of the hardware for the computer used for simulations.

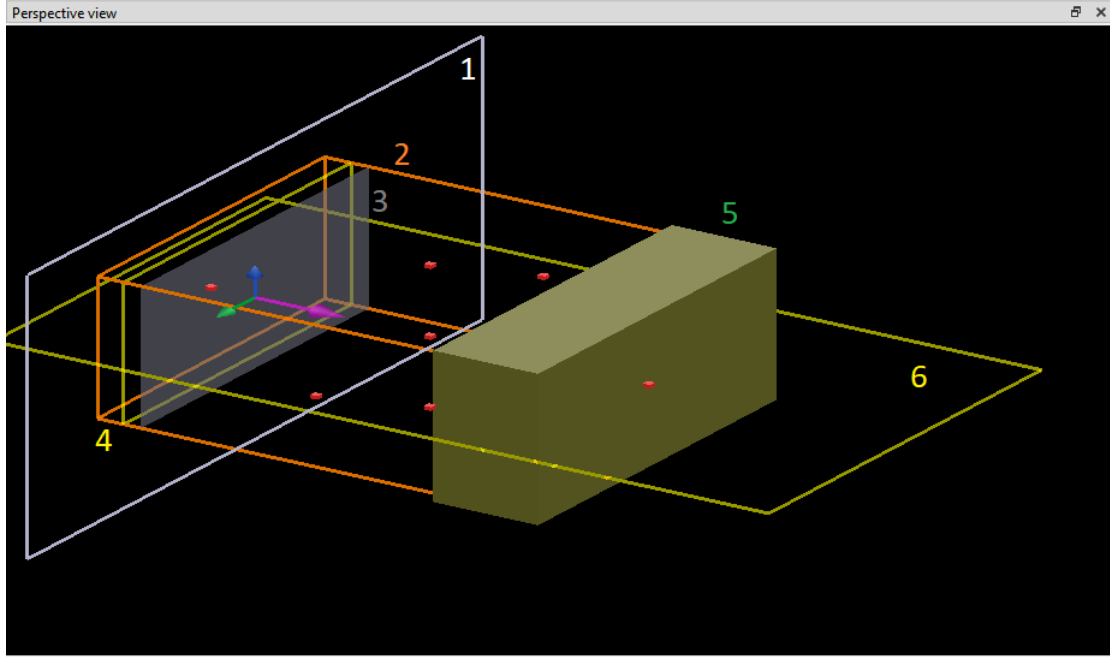| Component	Model	Memory	Speed
CPU	AMD Ryzen 5700X	512KB/4MB/32MB	4.2 GHz
GPU	RX Vega 56	8 GB	1156 MHz
RAM	Corsair Vengeance PRO	32 GB	3600 MHZ

Figure 25: *Overview of the simulation setup. 1.EM plane wave source. 2.Simulation boundary, which ends* inside *the material to avoid back-side reflections. 3.This is the overlap between the simulation boundary and the source - it is the output of the source within the simulation boundary. 4.This is the reflection monitor. 5.This is the material, which in this case is CdTe. 6.This is the movie monitor, which records the transversal amplitudes in the X-Y plane. Lastly, the transmission monitor, which is inside the material bulk (not visible in the figure).*

In the first setup which was designed for ARCs, the target is exposed to the EM radiation from the source placed 10 μm away, and the transmission monitor inside the material measures only the radiation *entering* the material. The reflection monitor placed behind the source will only be exposed to radiation travelling in the negative Z-direction, such that all radiation reaching the reflection monitor *must* have been reflected by the material boundary. This thesis only examines the amount of radiation transmitted *into* the material, and so interactions such as back-side reflections from the end of the substrate are not included in the results, as these would require application-specific solutions to compensate for. This means that the light transmission from the simulations performed here will be close to an ideal theoretical maximum, which can reach up to 99%, whereas if the back-side was included then the theoretical maximum would be $\approx 20\%$ lower, as the interference from the back-side can severely reduce the transmission. This difference will be attempted to be accounted for. The simulations were run with the source set to emit radiation in the 0.45-20 μm interval, which is the range this thesis will focus on.

Lumerical has an internal curve fitting tool used for fitting the complex refractive index (n,k), which was was used for the data sets used for the simulation. This tool has some caveats, as some data sets can generate singularities (where $n \to \infty$), or roots (where $n \to 0$) when fitted - though some customization of the fitting parameters is available, such as. CdTe clearly showed a spectral dependence for the refractive index, and as such, complete datasets must be gathered to emulate CdTe properly. Several datasets were found, as reported in the theory section, but only one was selected as the main

dataset. Namely the Hlìdek set, as this seems like the most consistent data set as it did not contain any fitting artefacts - no singularities.

An important aspect of these simulations which is not mentioned much in the literature is the reflectance of the *back-side* of the substrate. In this thesis, the back-side reflections are not included, as this would introduce further interference to the results. The literature reports a transmission of around 65% for CdTe, measured with FTIR, which includes the backside reflections. Assuming the front side and backside of the substrate reflects the same amount, and assuming air is the interface medium for both sides, one could assume that the front and backside account for half of the reflection losses each, and a test simulation presented below confirms this. This was simulated by first measuring the transmission *into* the medium, from the outside, then the transmission *out* from the substrate, by having the source inside the substrate, and measuring the radiation outside. The result of this is figure 26 below.
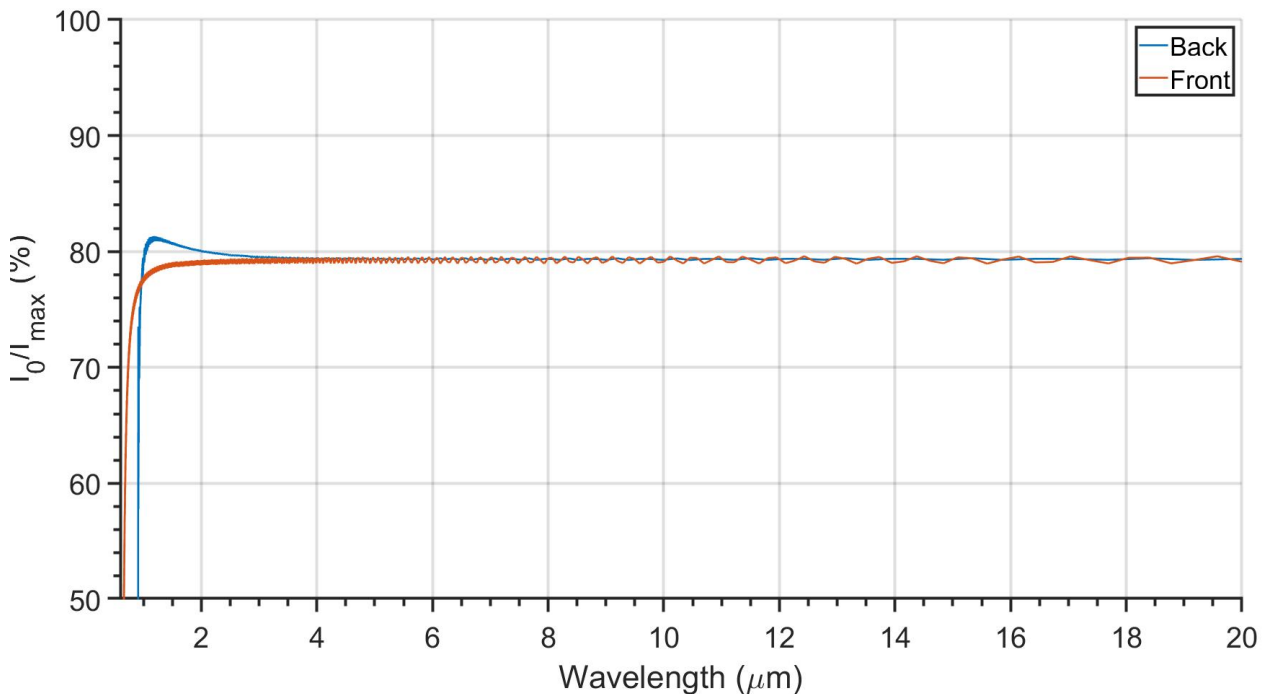
Figure 26: *Front and back reflection from the bare CdTe substrate. Showing that each boundary makes up about half of the reflection losses each.*

3.1.1 Substrate surface roughness

For the first simulations, the transmissivity of a smooth surface was investigated. This consisted of a simple rectangular cuboid of CdTe 6 μm thick. When simulating transmissivity through this surface, the boundaries between the media will be *completely* parallel to each other, as the surface is perfectly flat - which will never happen in the real world. Therefore, these initial simulations will represent ideal-world examples. These initial measurements were set up mostly go get acquainted with Lumerical, and ensure that the simulations were running as expected. But as the work developed, more complexity such as surface roughness had to be taken into account.

For the rougher surfaces, the geometry was set up using a script supplied by Lumerical, and then customized. This script is presented in appendix 1. The new substrate consisted of the same cuboid, but the side facing the source has a "roughness" structure included. This was done by setting up a 2D matrix describing the surface with random height values within a given range, and then applying a gaussian filter onto the matrix with the RMS and correlation lengths discovered from the AFM (see experimental section). In the simulation the correlation lengths were symmetric in the x and y direction. AFM measurements were performed to improve the predictions, and yielded an RMS of: $\sigma \approx$ 8 nm, and correlation length at around 100 nm. A reproduced surface used in the simulations can be seen in figure 27.
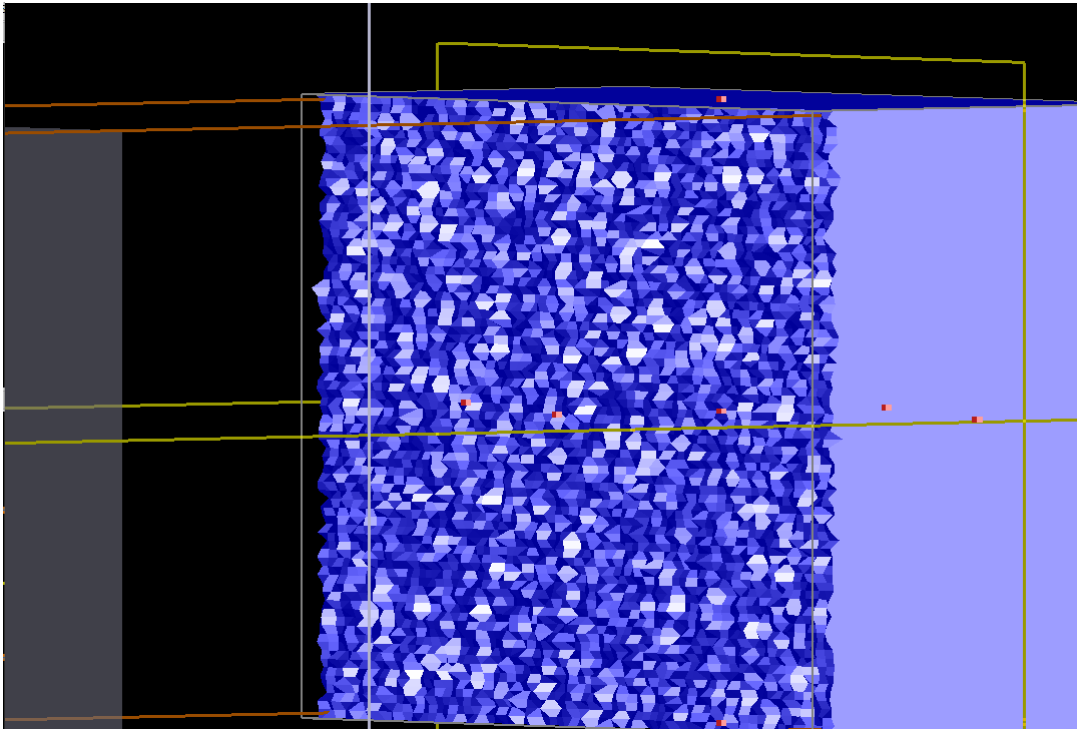
Figure 27: *Surface roughness emulated by a Gaussian distribution.*

After the first basic simulation was run with the parameters from the AFM measurements, some experimental simulations were set up to analyse *how* much roughness is needed to affect the transmission any substantial amount. The geometry script for the surface is set up in such a way that increasing the RMS will only generate sharper peaks, as seen in figure 28 below. These simulations are mostly to bridge the gap towards nano-structured surfaces, and can be used to compare with the nano-structures presented later, as they generate a graded refractive index for the whole surface.

Figure 28: *Surface roughness emulated by a Gaussian distribution with a very high RMS*

3.1.2   Anti-reflective coating - interference based AR

The anti-reflective coatings can be simplified as two overlapping materials in Lumerical, where the ARC material can be defined to have a higher "priority"(Mesh-order) - meaning that it is possible to choose which material that the overlapping area corresponds to. The ARC thickness was calculated using the thin-film formula described in the the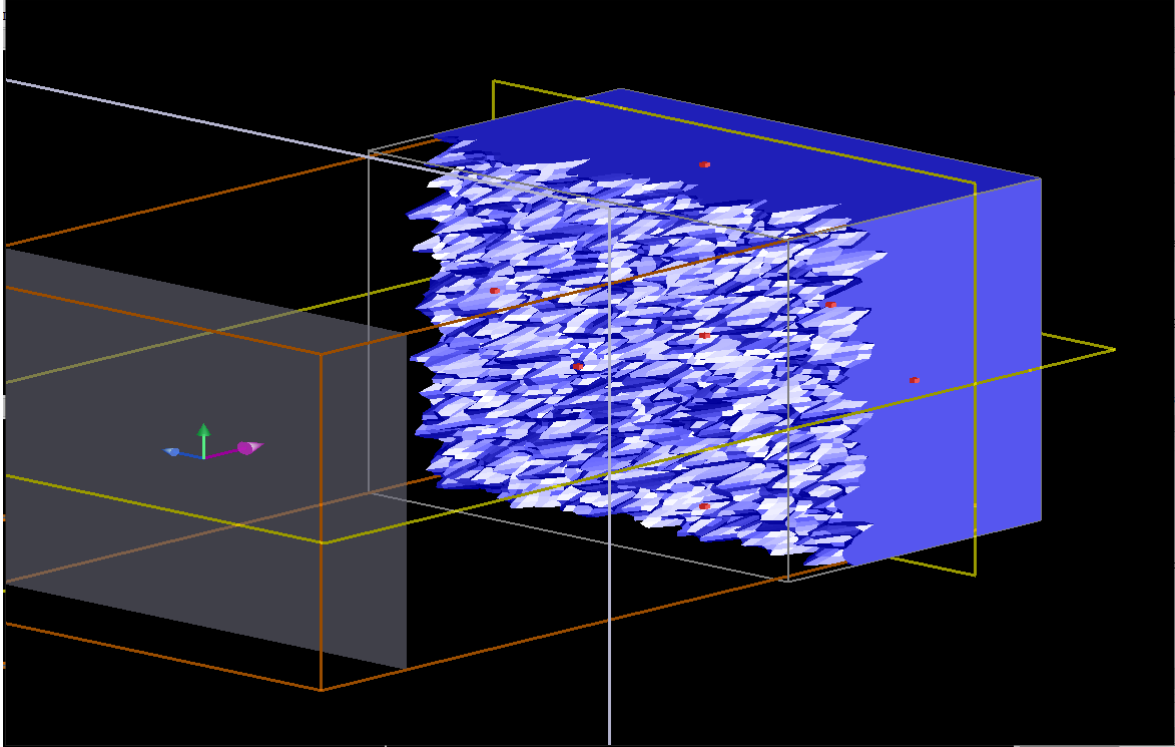ory, and then padded with some extra nano-meters, which would serve as the extra overlap width to compensate for the overlap between the ARC and the substrate. The transmission monitor was then placed still inside the substrate. Several different ARC materials was attempted, each designed for either the 3-5 or 8-12 μm range, or both.

3.1.3   Nano-structured surface - graded refractive index based AR

To generate the graded refractive index discussed in the theory, one can design the surface of a substrate to have fringes/pillars/textures for which the *effective refractive index* is dependent on the height/radius relationship of the structures, as discussed in the theory. The principles of the simulations for all of the methods presented in this thesis are generally the same:
Source→AR→Substrate→Transmission monitor. So the biggest difference between the ARC simulations (section 4.2.3) and the ARMS simulations is the design and implementation of the ARMS geometries. Several different geometries were implemented to be examined such as moth-eye (ME), truncated cones (TC), anti moth-eye (AME) and colloids, all of which were relatively simple to design in Lumerical through the use of scripts. These scripts were designed for the geometric specification of the structures, like how the moth-eyes - which are parabolic cones - were designed by implementing a $y = x^2$ conic

curve, and rotating it 180°, creating a full conic structure. The pillars were placed twice the base radius apart, so that there was no overlap at the base. The structures were placed in a grid such that they made up a hexagonal pattern, as seen in figure 29 below. The exact same procedure was performed for the other structures, but with a different function to be rotated. The truncated cones were made up of function describing a line, creating a full cone, for which the height was set to be lower than the height of the full cone to achieve the flat top. For the AME, the same procedure as for the moth-eye was performed, but with $y = \sqrt{x}$ instead. The colloids were designed as spheres, and not through a rotated function. The moth-eyes are shown in figure 30, and the script which generates them is presented in the appendix in listing 1.

Since the simulations for the ARMS are hexagonally symmetric, a simplified simulation boundary can be set up which works well with the periodic simulation boundaries, which "copy" the structures in the x-y plane and creates a large plane of the nanostructured surface. The boundary can be seen in the figure below.

$2(3)^{\frac{1}{2}}r_0$

r_1

$2r_0$

$2r_0$
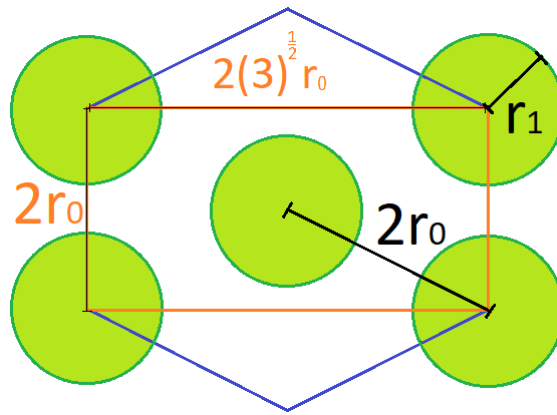
Figure 29: *Simulation boundary setup for periodic boundaries (in orange), where the structures are placed in a hexagonal pattern.*

This simulation setup would be the most compact way of describing the arrangement of the structures without including any excess material, therefore this setup would reduce the simulation times significantly. In addition, this ensures proper periodicity of the structures, as the contents in the simulation boundary would be completely line symmetric along all edges.

Figure 30: *The moth-eyes generated by script 1. Only 5 pillars are needed for the simulation, but the for-loops which generate the structures are cleaner like this. Additionally, it seems like the moth-eye pillars are outside the substrate, and this is correct, but these parts are not included in the simulation boundary (orange) as the setup follows figure 29.*

3.2 Experimental setup

Several experiments were set up to compare the simulation results with the substrates on hand. Two CdTe-chips were acquired from II-VI Inc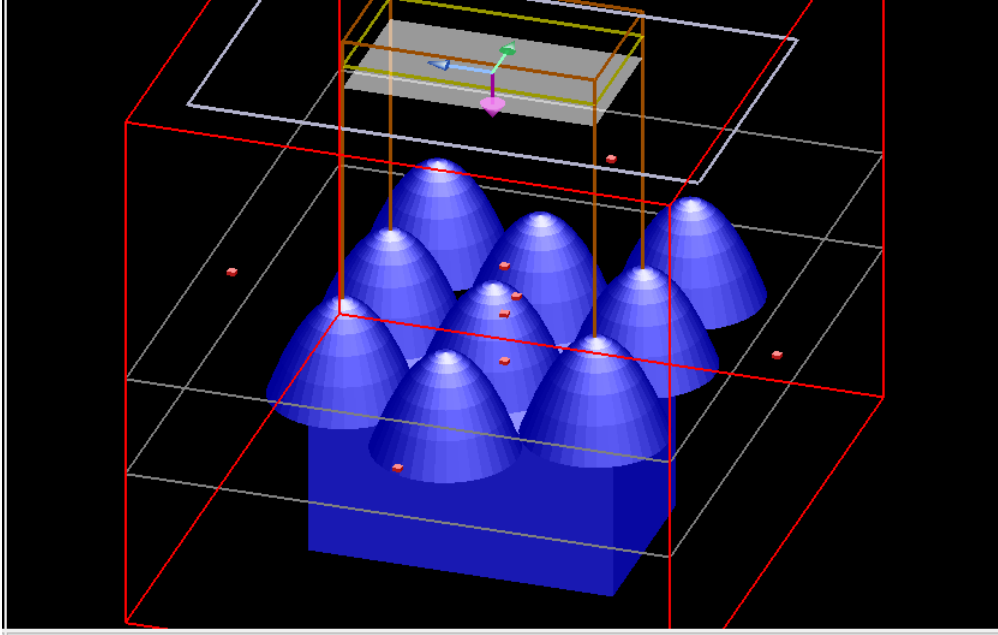orporated [51]. The first one was broken during experiment, but could still be used. The second one was chemically polished on one side, and mechanically polished (FG) on the other side. The AFM measurement was of the FG side. The optical properties were characterized using the FTIR to measure the transmissivity, and the AFM to measure the surface roughness. A double sided polished silicon substrate was also investigated as a reference to the CdTe, as silicon is more expendable with respect to price and availability, and it has good transmission properties in the IR.

3.2.1 FTIR spectroscopy

To acquire a meter to compare the simulations with, the Nicolet iS50 FTIR spectrometer at the Department of Chemistry at UiB was used. Several chips were measured - the bare silicon chips, as well as the silicon coated with ZnO.

3.2.2 AFM

The atomic force microscope at the faculty of physics and technology was used to measure a surface profile of the CdTe substrates. This would be used for the rough surface analysis, and as a precursor to the nano-structures, as roughness provides a lower gradient to the refractive index for a material.

4   Results and Discussion - Simulations

In the following chapter, the results following the material transmission simulations are presented and discussed. These are shown as transmission or reflection graphs exported directly from Lumerical FDTD simulations. First the data for CdTe is compared to other sources of transmission for this material. Silicon is used then as a substitute, as there is good documentation on this material. Second, the transmission for the bare CdTe substrate is presented, along with reference data from other sources. Then surface roughness is added to the CdTe substrate, and transmission is measured through the new surface and presented. ARCs were designed and simulated, with different coatings. Lastly different ARMS designs were applied to the substrate, with different geometries and feature sizes.

4.1   Parameter selection

4.1.1   General simulation parameters

For most applications of the anti-reflective methods used here, the IR source is often far away, and as such, the angle of incidence (AoI) of the IR radiation reaching the detector would be close to perpendicular to the substrate. For this reason, the AoI in the simulation is always perpendicular to the substrate. Additionally, the simulations only include the transmissivity into the substrate through only one boundary, namely the front. The back-side reflections is, as mentioned earlier, excluded, as the back-side boundary of CdTe is still unknown and interference effects from the back-side of the substrate would make the conclusions from these results much harder to determine. Therefore the z-direction was set as a PML. For application-specific simulations it is recommended to properly apply anti-reflective methods to the back-side as well. It must be noted that there *will* be additional losses in the completed design, and these losses will be *heavily* dependent on the electronics/materials that are connected to the back-side of the substrate, and their boundary. Often this will be HgCdTe, which if applied properly, should allow most of the radiation to pass through without loss. Therefore, including the full reflection losses before determining what the back-side will be connected to would be a rash decision. Therefore, it might seem like this thesis achieves higher than before results.

4.1.2   Wavelength range

The wavelengths used in these simulations were selected to be 0.45 - 20 μm. This is because this contains most of both of the atmospheric windows, meaning higher atmospheric transmission for the specified wavelengths. These are selected, as the goal is to categorize several IR transmission optimisations techniques, for the whole range. CdTe has a band gap at 1.52 eV ($\approx 0.8157\mu$m), which means it absorbs much more light below $\lambda \approx 0.82\mu$m, as the photons are energetic enough to move the valence band electrons into the conduction band.

4.1.3   Refractive index

The datasets used for the refractive indices were selected based on their ranges, and so the narrow-band precision might be compromised to some degree. In spite of this, three

good datasets have been gathered and compared, and the best one is selected. Namely, values from Hlìdek [18], Marple [26], and Palik [33] was used. It was found that Hlìdek had the most consistent values. A caveat to this dataset however, is that the curve fitting tool for refractive indices in Lumerical is either far too aggressive, or too passive on the dataset in the ranges around 0.6 μm. This "glitch" is also present in the Palik dataset. The Marple dataset on the other hand, does not cover the entire range.

4.1.4   Surface roughness

The only physical difference between the smooth- and rough-surface simulations were the way the surface of the substrate is generated, so the values here are the same as for the smooth surface simulations. To get better results from the rough-surface simulations, AFM profiles of the surface was made using the atomic force microscope from the Faculty of Physics and Technology, and then analyzed using the SPM software GWYDDION [29]. The profile of some 10x10 μm chip can be seen in figure 31 below as an example.
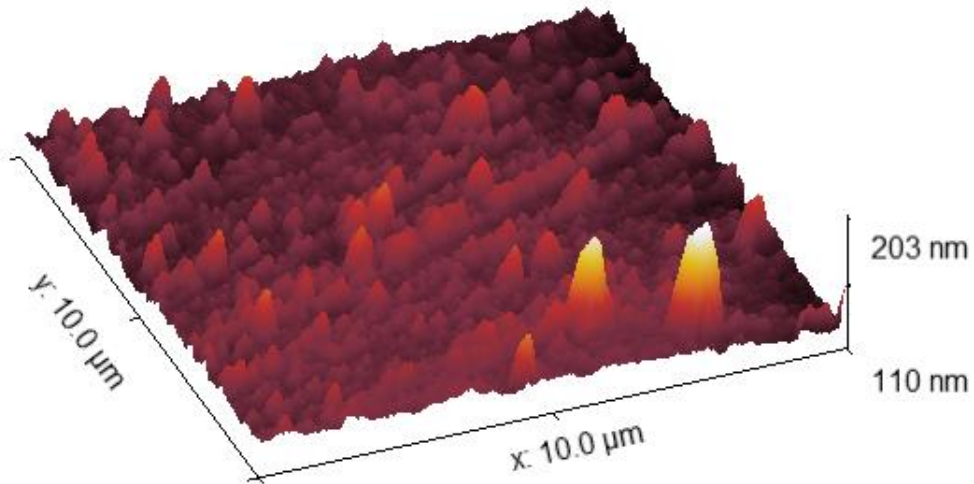

Figure 31: *AFM measurement of a polished 10x10μm CdTe chip.*

4.1.5   Anti-reflective coated surface

When selecting a thin-film, two parameters are the most important - namely the material it self, and the thickness of the film. The materials used here were selected from a large group of known anti-reflective materials. The thickness on the other hand, must be calculated from *where* one wishes the transmission peaks to be. In the case of these simulations, the film thickness was optimised based on the thin-film interference formula presented earlier. The transmission spectra for Al_2O_3, SiO_2, DLC (Diamond-like carbon) and ZnO are shown in the figure below.
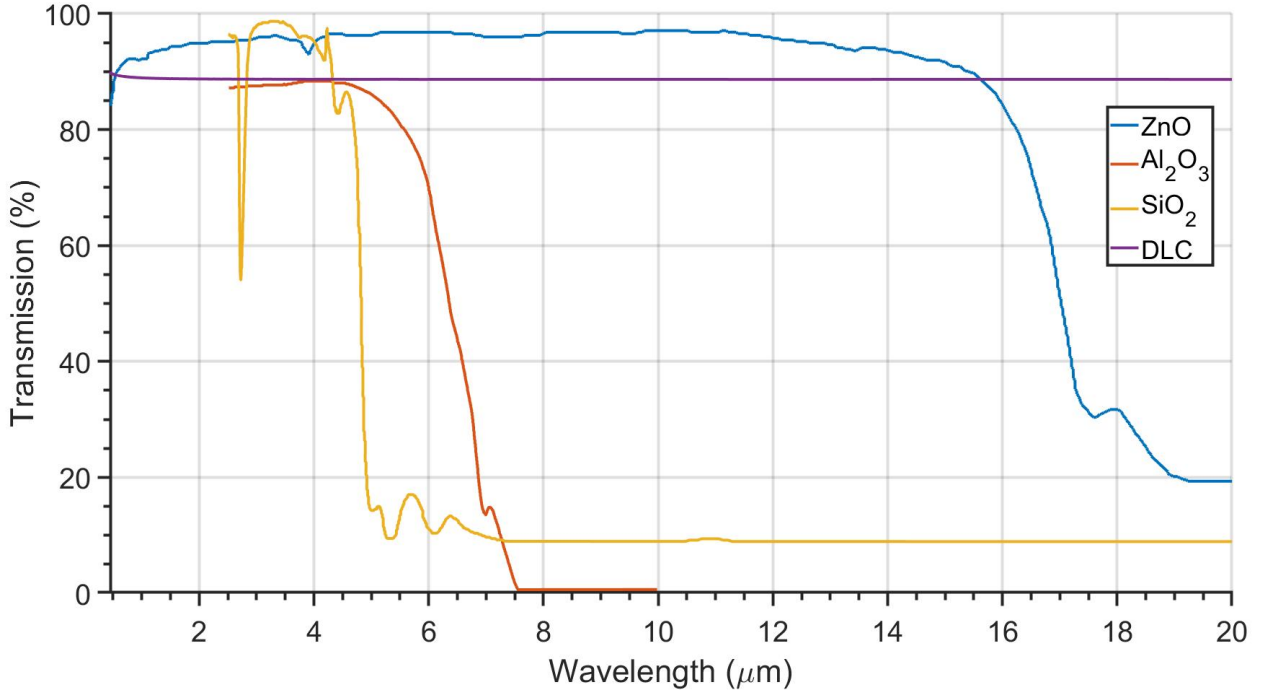
Figure 32: *Transmission spectra for the anti reflective materials as bulk materials, sourced from the literature. Since no complete dataset for bulk-transmission for DLC (Diamond-like carbon) was found, it was simulated(only narrow-band transmissions were found). This could be cause for an incomplete picture.*

To get the most relevant values for the atmospheric windows, one can *scale* the transmission of the material to the atmospheric windows. That is, $T_{total} = T_a * T_m$, where T_a is the atmospheric transmission, and T_m is the material transmission. The atmospheric window spectrum presented earlier is somewhat normalized, so this the resulting graph can help identify the best wavelengths to optimise for. Doing this results in what is presented in figure 33 below. Here it can be seen that many of the materials will complement the first atmospheric window between 3-5 μm, whereas ZnO and DLC would work well in the second window.
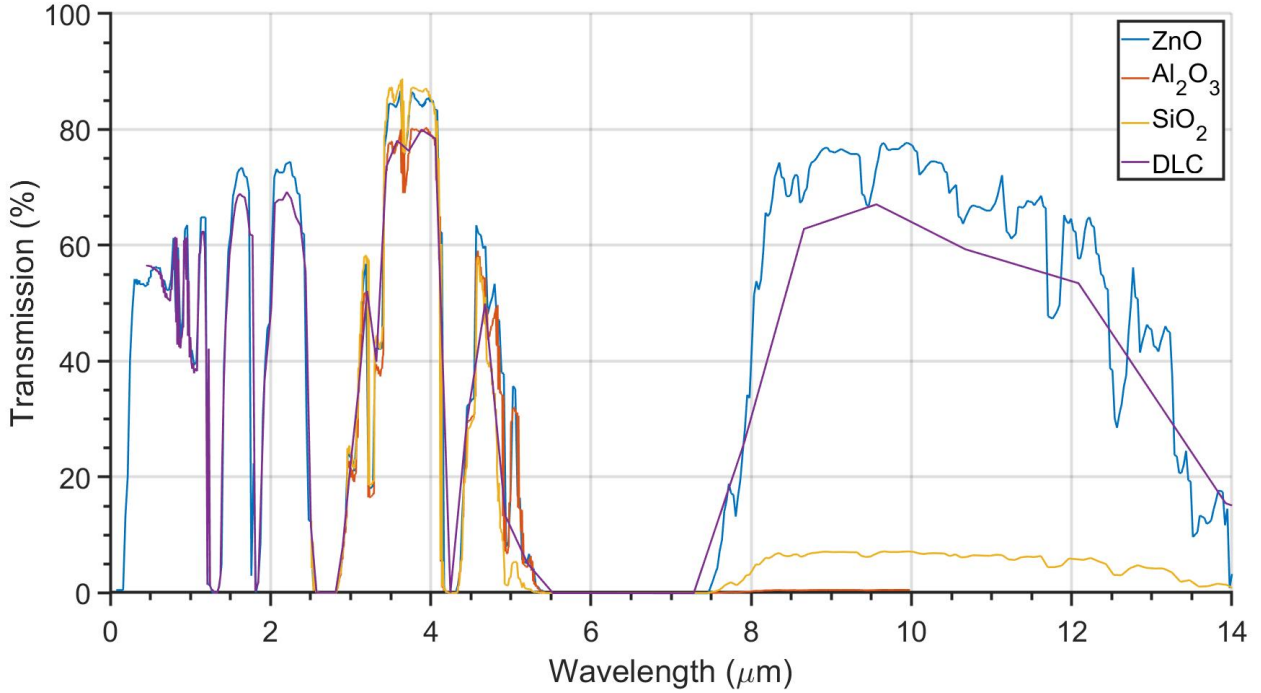
Figure 33: *Transmission spectra for the anti reflective materials as bulk material, but scaled in relation to the atmospheric windows.*

4.1.6 Micro-structures

The first part of the results presented for micro-structures is a collection of the results from a broad literature search for reference geometry. Since it is hard to calculate what parameters for the micro-structures would be closest to the ideal, examining published solutions was the best thing to start with. It can be observed from the literature that the radius and height ranges that are the most relevant are 2-4 μm for radii, and 2-9 μm for the heights. Several geometries from the literature were tested: Moth-eye, anti-moth-eye, tapered cones posts, and lastly deposed colloids.

4.1.7 Reference material

There is a big difference in cost and availability between CdTe and Si. As such, silicon was selected as a reference material as it also possesses IR transmission properties comparable to CdTe, and it is better documented than CdTe. Additionally, silicon chips are inexpensive, expendable, have well documented process techniques, and is readily available at the university.

4.2 Transmission simulations - CdTe

In this section, the transmission properties of CdTe is explored through FDTD simulations. A basic characterization of bulk CdTe had to be done before working with the anti-reflective techniques. Such as simulating the transmission of bare CdTe, and comparing with reference data. Then, surface roughness is added and compared, using the AFM measurements. Then the anti-reflective methods are explored. Several ARC designs were tested and simulated in Lumerical, with focus on improving the transmission in the

3-5 and 9-12 μm range. Then ARMS were sourced from the literature, and modified to achieve the highest average transmission in either of the two ranges.

4.2.1 Smooth surface

The transmission and reflection of a smooth 3 μm thick CdTe surface is shown in figures 34 and 35 respectively. Three different data sets were used to better determine which data sets would be used onwards. The three datasets have similar transmission curve in the 1-20 μm range, but they are different in the <1 μm range, as seen in figure 36, though this is outside the important wavelength ranges of 3-5 and 8-12 μm and therefore will not affect the end results much. Additionally, it is worth taking note of an unintended glitch in the data set after curve fitting. The Palik set shows a sharp peak at 0.85 μm, which originates from the curve fitting tool.
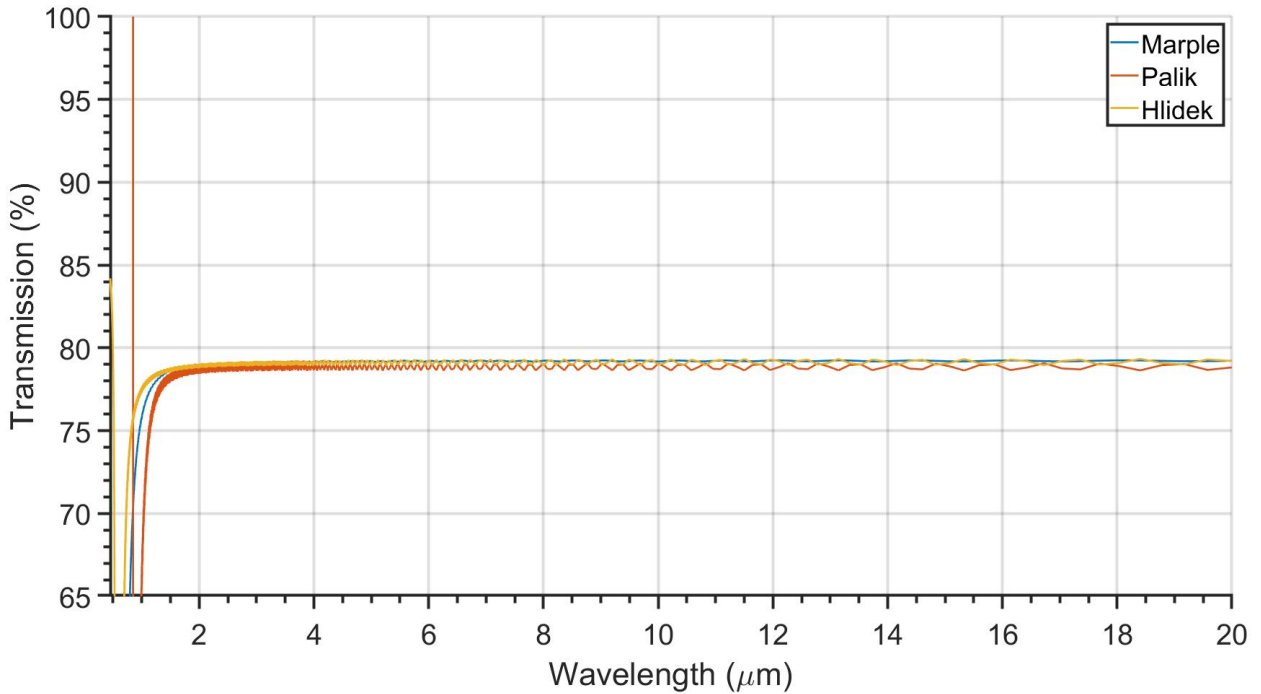
Figure 34: *Transmission for smooth CdTe surface for three different datasets for the refractive index*
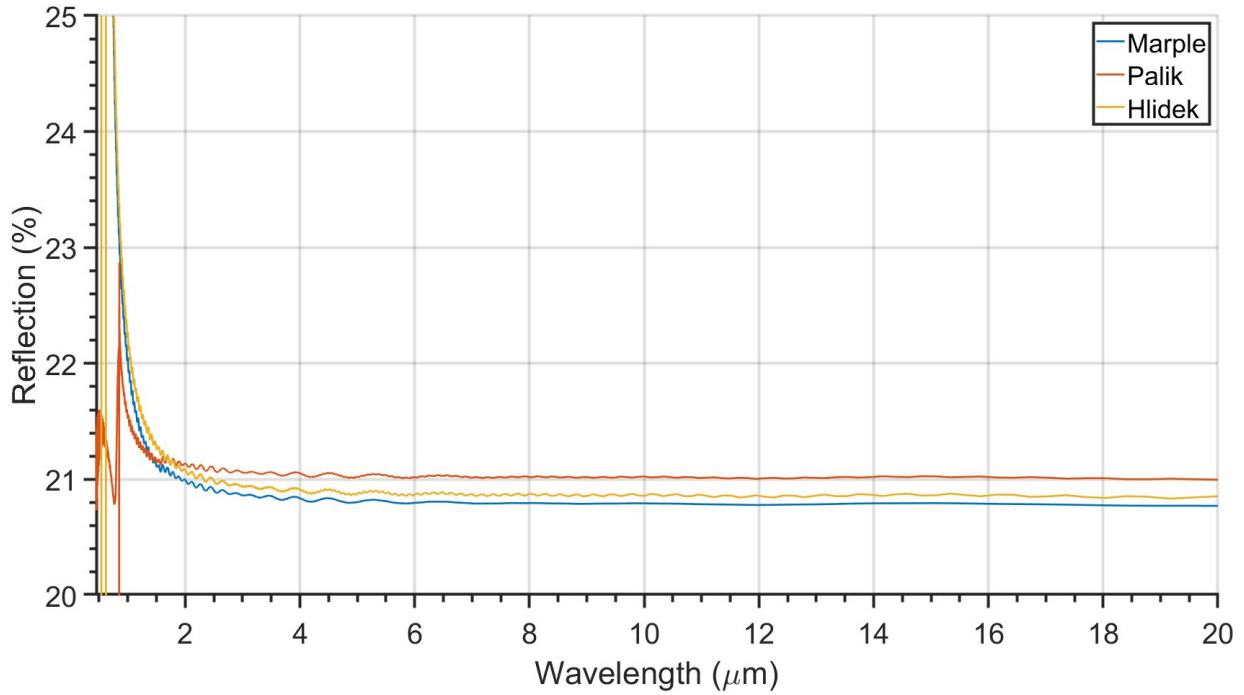
Figure 35: *Reflection for smooth CdTe surface*

Figure 36: *Transmission for smooth CdTe in the 0.5-1.5 μm range.*

Considering the simulations are performed with the transmission monitor inside the substrate, the back-side reflections do not produce interference, and hence the results may seem higher than they are. Assuming, as predicted by back-side reflection argument presented earlier (that including the back-side reflections would essentially double

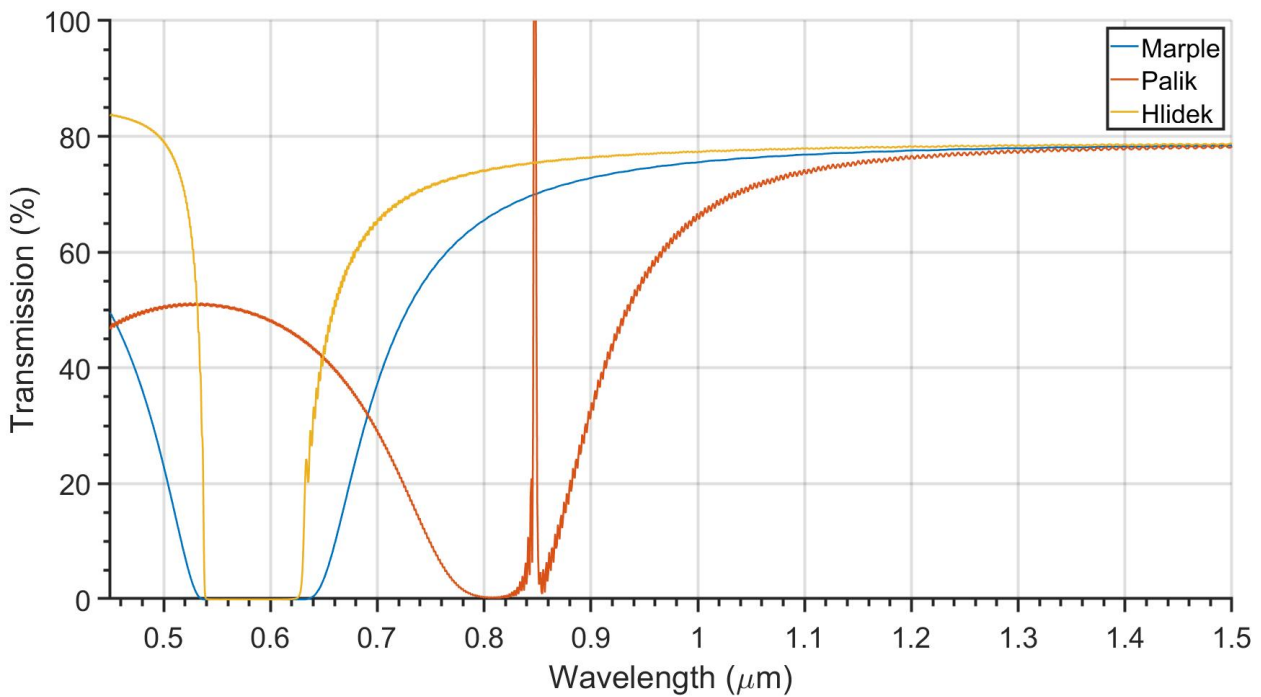the reflection losses), the transmissions measured by the providers without the back-side reflections should lie around 82%, whereas the average measured in simulation is approximately at 78%. Comparing these results to the FTIR measurements presented earlier, then these measurements show a difference of 4% between simulation and FTIR measurements, which is not entirely surprising, as even the FTIR measurements can have discrepancies of this size. The simulations use a set value (either refractive indices or permittivity) to emulate the CdTe crystal, but the crystals used in the literature can easily have different quality levels.

4.2.2   Rough surface

To investigate how the effects of surface roughness affects the transmission, simulations which included a randomized-height surface with Gaussian distribution facing the source were perfomed, and the results are presented in figure 37 below.
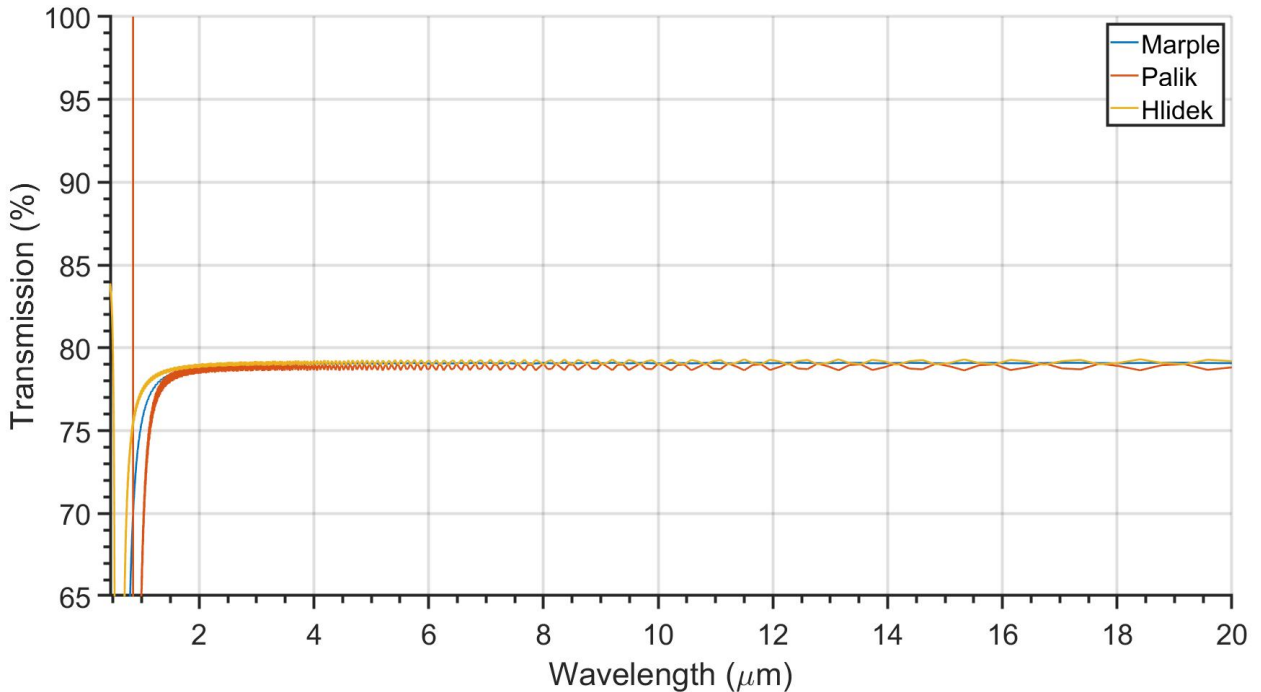

Figure 37: *Transmission spectrum for rough CdTe surface*

The transmission differences between these data are negligible ($> 0.025\%$). This is likely due to very low size differences between the rough structures. And so, simulations with even *rougher* (albeit unrealistic sizes) surfaces are performed and presented below. According to the theory presented in the theory section, the transmission should increase as the pillars, or "roughness" get more defined - with the radii mostly affecting the transmission *bands*, and heights affecting the transmission magnitude. At 0.3 μm and 0.8 μm RMS, the difference apparent, as seen in figure 38. It should be mentioned that the structures simulated do not correspond well to real surface roughness, and especially when the RMS is exaggerated. The structures manifested by the high RMS are closer to spikes, than to natural roughness. These spikes are hence conceptually closer to the desired moth-eye structures, in that they produce a smooth gradient to the refractive index, so they can therefore be used to compare with the ARMS.
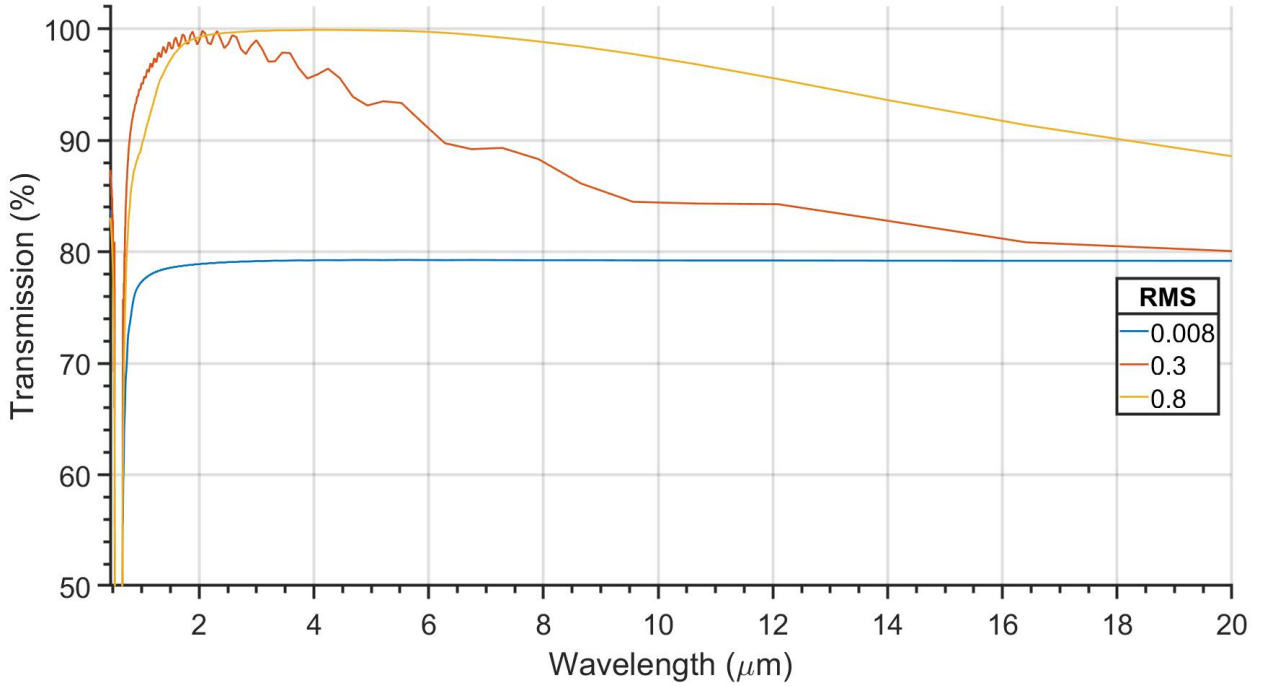
Figure 38: *Transmission spectrum for very rough CdTe surfaces*

As expected from the theory, the transmission increases with the roughness. The gradient for the last surface is excellent for broadband transmission, but is also mechanically unstable, as the peaks are extremely long and extremely thin. Yet these simulations illustrate the mechanics of a smooth gradient of the refractive index.

4.2.3   Polarization simulations

Some polarization simulations were made to make sure that there is consistency between the simulations, literature, and the theory. CdTe is not a polar material, implying that there should be no difference in the transmission based on the polarization of the incoming light. This was done by simulating the same setup, but with 0 ° and 90 ° polarization for the source. Cadmium Telluride is not a polarized material and has a low electro-optic effect [11], therefore little difference is expected in transmission based on polarization. The result is shown in figure 39 as a difference between transmission between the two polarizations (abs(T(0°) - T(90°))).

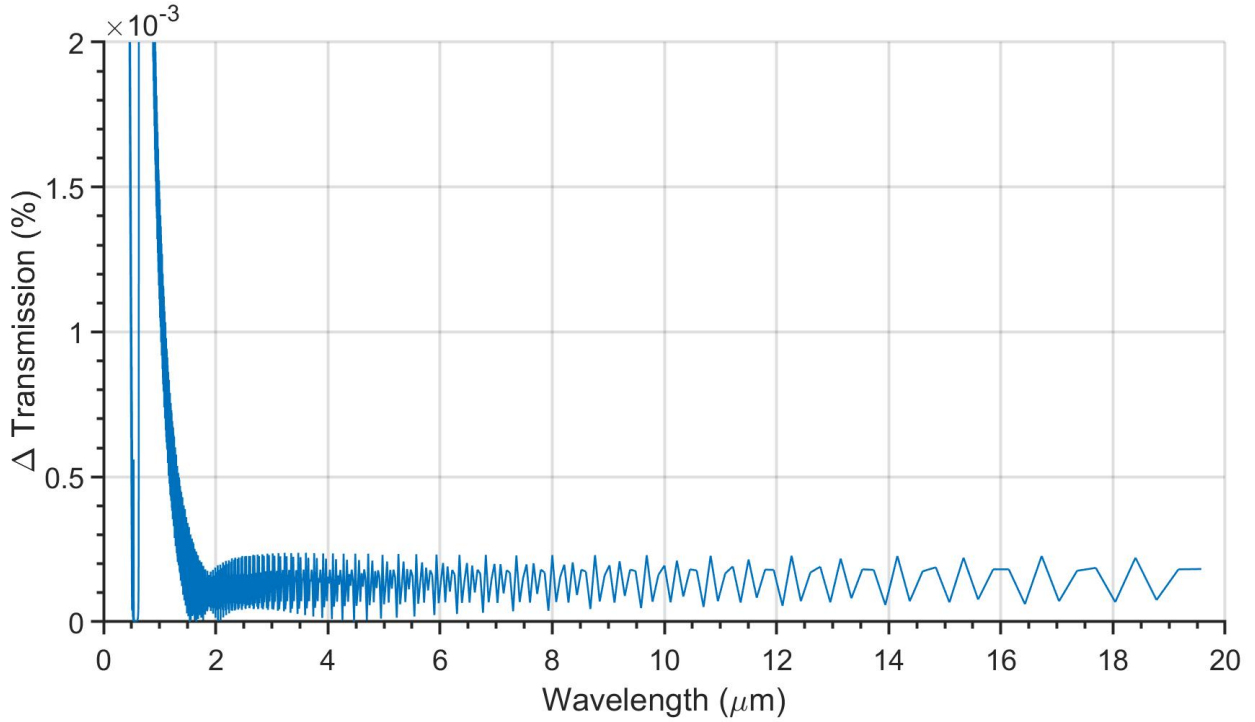**Figure 39:** ΔT in percent for $0°$ and $90°$ polarization

Additionally, when measuring the transmission with an FTIR, the backside reflections are included in the transmission spectrum, meaning the theoretical maximum for these measurements would never be 100%. This explains the discrepancy between the reported transmission by providers in figure 2, and the simulated transmission in figure 34.

4.2.4 ARC simulations

Four promising ARCs were found during the literature study, for which the thicknesses of the ARCs were optimised for the highest transmission within the atmospheric window peaks shown earlier in figure 33. The transmissions for these thicknesses are presented below in figures 40 through 42, with the optimised thicknesses from table 4.

Table 4: Parameter selection for ARCs. *Not a complete dataset for the entire range, but the values are *very* consistent, so the extrapolated value was selected by linear approximation. Note that the transmission maximum is taken from 32, but wavelengths are read from the 33.

Material	Peak (μm)	T max	n	t (μm)
$ZnO(1)$	4.08	96 %	≈ 1.9*	0.54
$ZnO(2)$	10.33	96 %	≈ 1.6*	1.61
Al_2O_3	3.93	88 %	1.57	0.62
SiO_2	3.88	96 %	1.40	0.69
$DLC(1)$	3.89	89 %	2.09	0.47
$DLC(2)$	10.68	89 %	2.09	1.28

As shown in figure 32 above, which shows the transmissivity for the ARC materials, the transmission for ZnO extends over almost the entire wavelength range. For this

reason, ZnO was attempted to be made into a dual-band transmission window for both the 3-5 and 8-12 μm atmospheric windows. But first, the coating which was optimised for transmission at 4.08 μm reached a peak transmission value of around 97%. The 1.61 μm thick coating on the other hand, which could work as a dual-band transmitter, as it shows two transmission peaks of $\approx$ 96% and $\approx$ 99% at 4.08 and 10.3 μm respectively. The results can be seen below in figure 40.
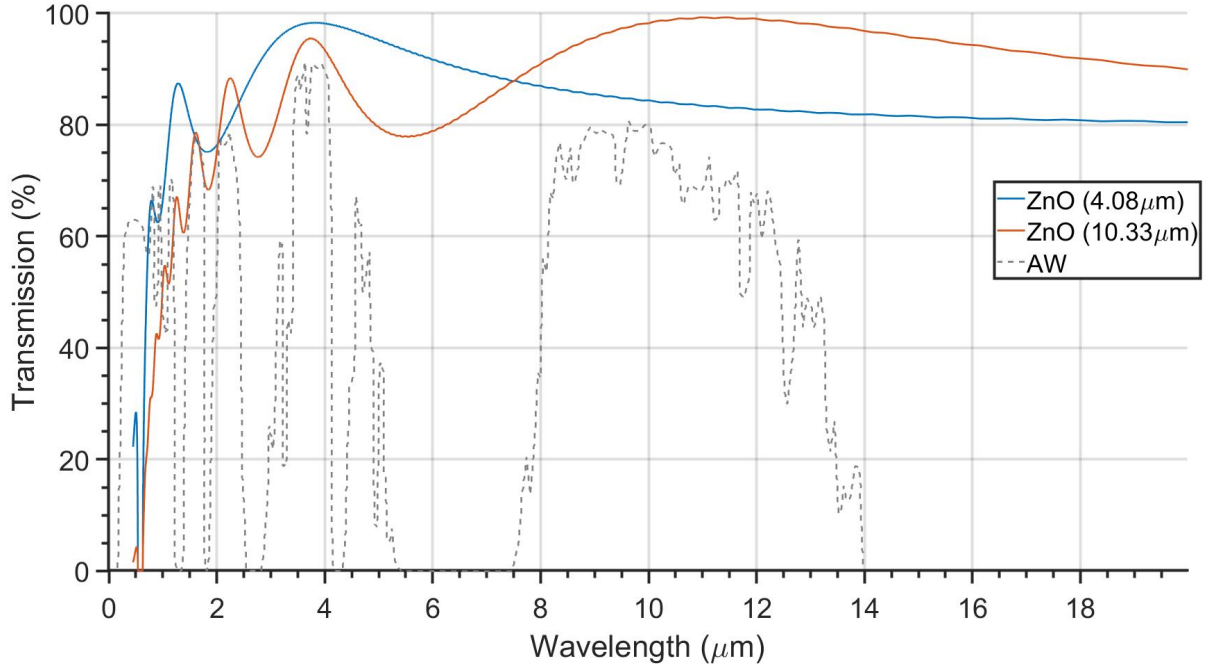
Figure 40: *Transmission spectra for CdTe with ZnO as ARC*

Both Al_2O_3 and SiO_2 showed in figure 32 that they have poor broadband properties, as they have high absorption beyond 7 and 5 μm respectively, but they still can be improved for the 3-5 μm range. After optimisation, the peaks could be generated by relatively thin films of around 0.65 μm each, and transmission results upwards of 99% and 95% for Al_2O_3 and SiO_2 respectively, as seen in figure 41. Both materials used for these coatings are remarkably damage resistant due to their high robustness, and so applications for these materials should not be hard to find.
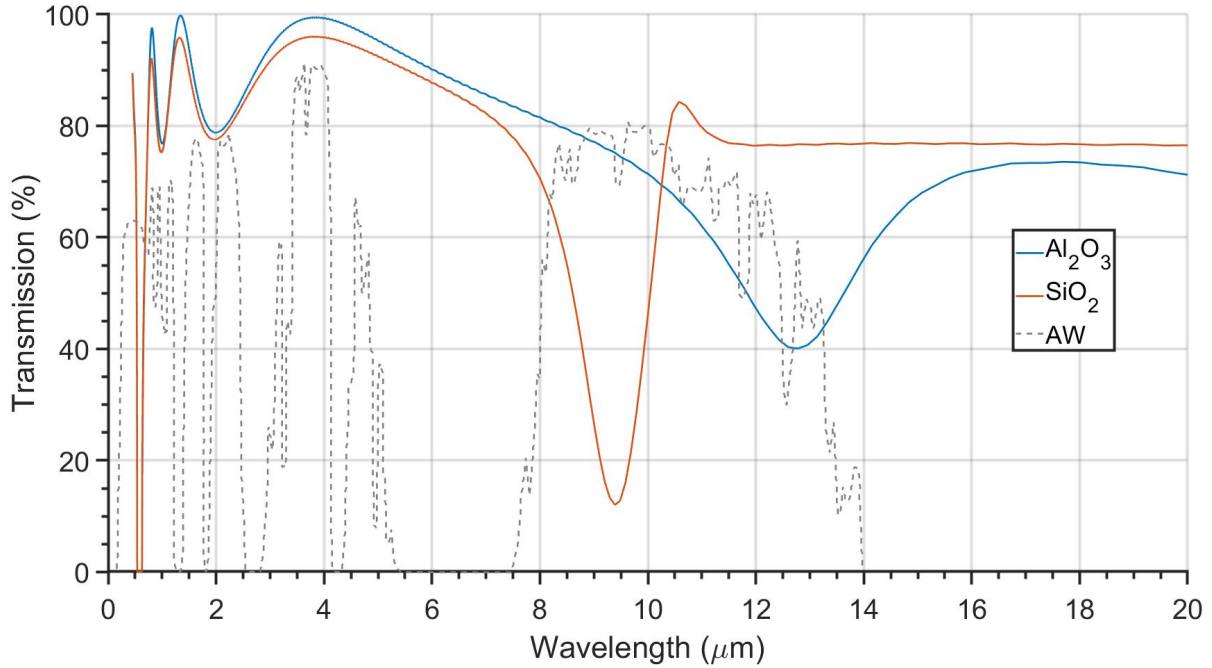
Figure 41: *CdTe with Al_2O_3 and SiO_2 as ARC*

Another damage resistant material, which is known as the hardest material, is diamond [17]. Making these measurements interesting, as the mechanical properties of diamond are top tier. The results below illustrate that DLC is a decent ARC for both the MWIR and LWIR bands, even as a dual-band ARC. All three desired peaks were measured to have a transmission of $\approx 96\%$, which for an ARC is good.

Figure 42: *Transmission spectra for CdTe with DLC as ARC*

Table 5: Averaged results for optimal thicknesses around optimal ranges (3-5 and 8-12 μm) for ARCs.

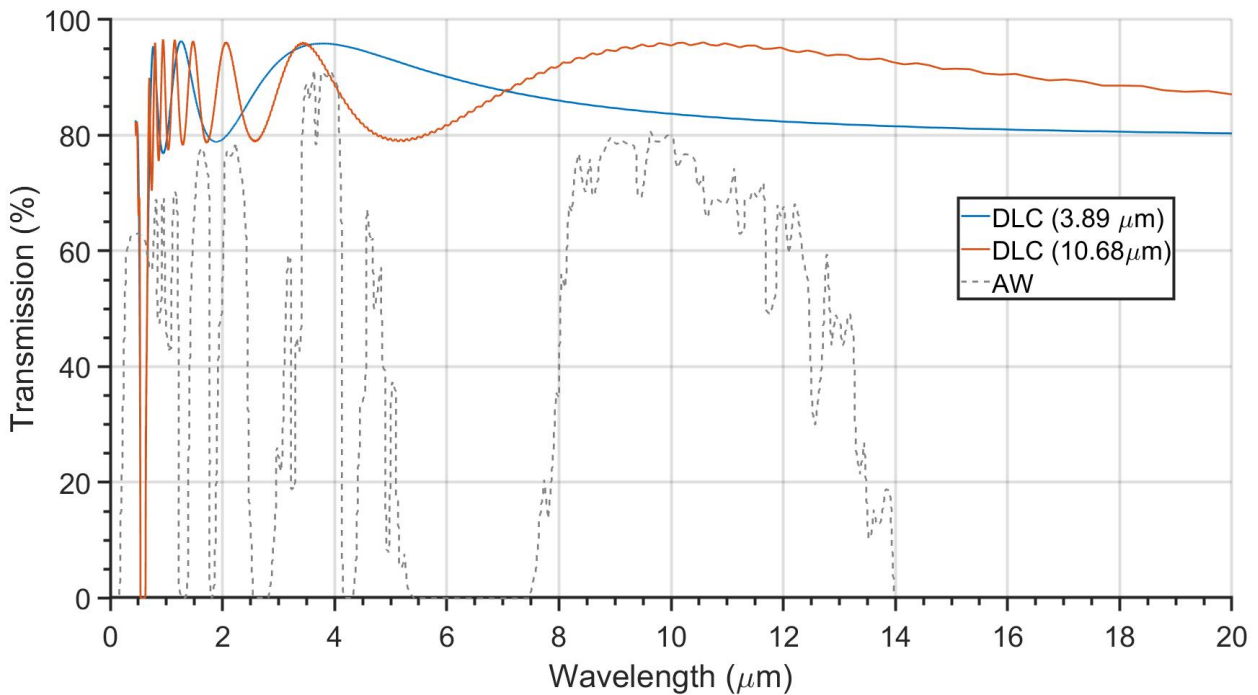| Material	t(μm)	$\mathbf{T}_{avg}$(3-5 μm)	$\mathbf{T}_{avg}$(8-12 μm)	$\mathbf{R}_{avg}$(3-5 μm)	$\mathbf{R}_{avg}$(8-12 μm)
$ZnO(1)$	0.54	97.05 %	84.80 %	1.54 %	15.07 %
$ZnO(2)$	1.61	88.24 %	96.58 %	7.90 %	2.76 %
Al_2O_3	0.62	97.79 %	71.1 %	1.83 %	22.90 %
SiO_2	0.69	94.62 %	54.24 %	3.72 %	30.09 %
$DLC(1)$	0.47	94.86 %	84.12 %	5.14 %	15.87 %
$DLC(2)$	1.28	89.40 %	94.8 %	10.59 %	5.20 %

All of the results presented for the ARCs reached values, as expected by the literature presented in table 2. Some minor improvements could be done by further precision calculating the substrate thickness and wavelength peak position for the atmospheric windows, but the difference in crystal quality and deposition technique would likely exceed the transmission difference in these optimisations.

4.2.5 ARMS simulations

For the first part of this section, several designs from the literature was adapted and simulated. This yielded a better understanding for the mechanisms, and a better overview before optimisation. The literature was selected based on material and wavelength range. The goal here is to find the geometry and size relationships which yield the highest transmission improvements for the 3-5 and 8-12 μm ranges.

Geometry from the literature
This first section serves as a proof of concept of how *much* more transmission is possible with ARMS with different geometries. The literature suggest a large range of configurations for different wavelengths, but even for broadband transmission the difference in design varies quite a lot. During the literature search, seven different structures were found, where four were tested here. The seven structures were moth-eyes, truncated cones, anti moth-eye, colloids, random-texture AR structures, nano-rods, and lastly sub-wavelength structures (like posts) - of which only the four first were simulated.

Moth-eye structures:
Moth-eye structures are as said a favourite from the literature, and it is easy to see why. The transmission spectra for a selection of geometries for moth-eye structures sourced from the literature is shown below. The structures display peak transmission of 99.9 % in narrow periodic bands. It can be observed that the transmission is affected by an interference effect, as the transmission show a periodic tendency. When the simulations were viewed through a "movie monitor", which plays back an illustration of the amplitudes of the EM waves as they interact with the ARMS, it became apparent that these interference effects could be from the X,Y-plane, as the pillars are symmetric. Fortunately, the magnitude of the effect is low, but yet the transmission varies with about $\approx$ 5%, which is potentially a quite large difference when trying to achieve transmission of up to 99%. On the other hand, these peaks could help focus the transmission bands at the desired wavelengths, with less transmission in less the desired wavelengths.
A band limit for the shorter structures (3.16 μm) can be observed for the 0.31, 0.7 and

1.5 μm radius structures (crimson, lime and cyan). This is the upper limit of the transmission properties for these heights it seems, as the height determines the steepness of the gradient of the refractive index - as observed in figure 43 and mentioned in the theory. *All* of these structures had an average transmission of $> 99.\%$ average transmission over the specified ranges, as can be seen in the figures 43, 44 and table 6.
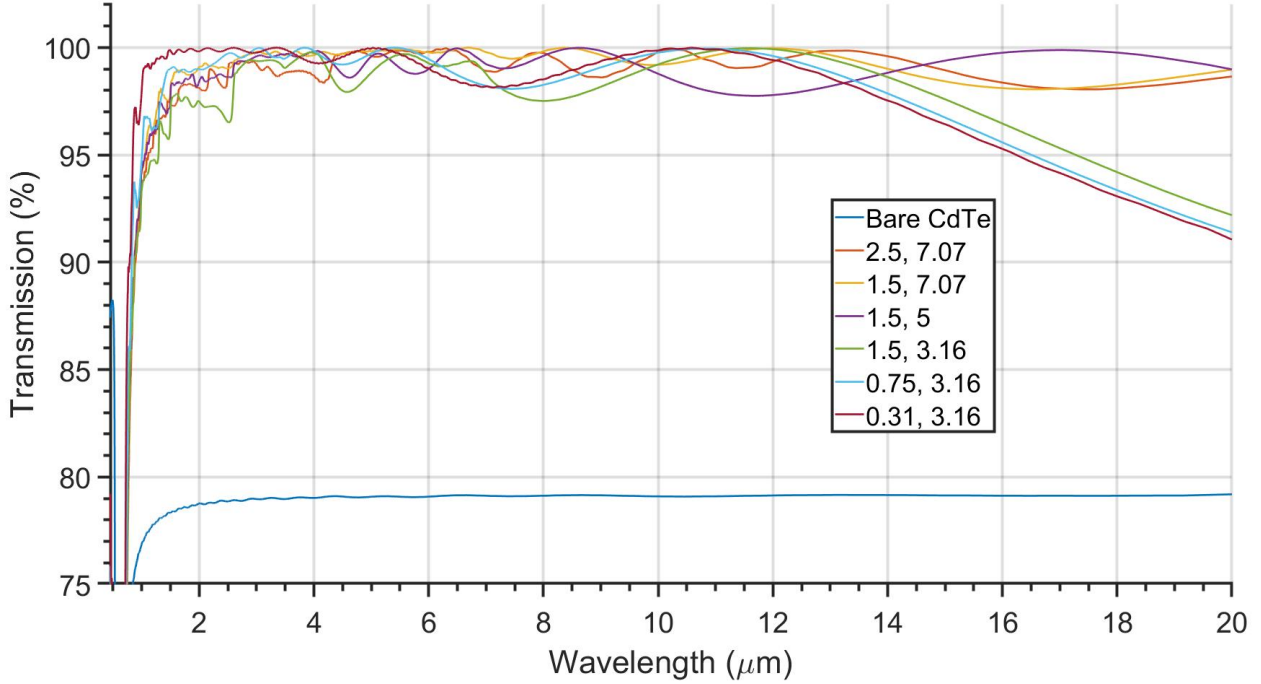

Figure 43: *Transmission spectra for CdTe different ARMS designs from literature, simulated in Lumerical. Note that all these are moth-eye structures. The transmission for bare CdTe is included as a reference. The units given in the legend are bottom radius and structure height respectively, given in μm.*
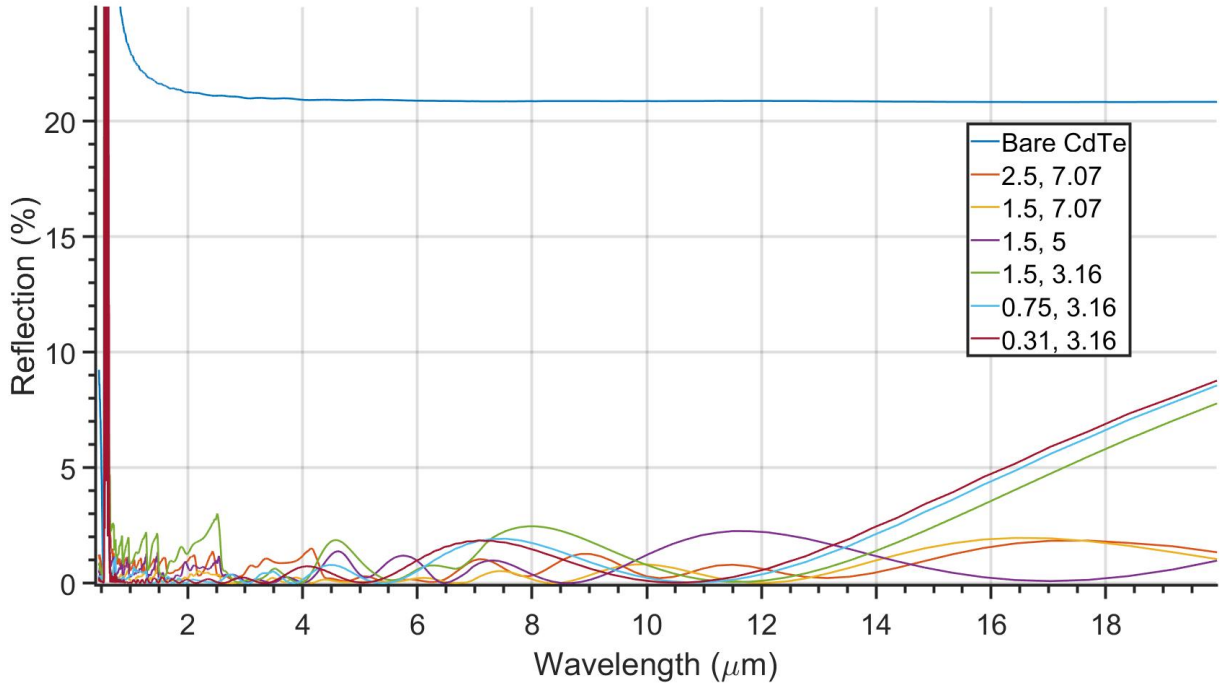
Figure 44: *Reflection spectra for CdTe different ARMS designs from literature, simulated in Lumerical. Note that all these are moth-eye structures. The units given in the legend are bottom radius and structure height respectively, given in μm.*

Table 6: Averaged results around optimal ranges (3-5 and 8-12 μm)

$\mathbf{R_0}$	$\mathbf{h_0}$	$\mathbf{T}_{avg}$(3-5 μm)	$\mathbf{T}_{avg}$(8-12 μm)	$\mathbf{R}_{avg}$(3-5 μm)	$\mathbf{R}_{avg}$(8-12 μm)
2.5	7.07	99.04 %	99.24 %	0.76 %	0.75 %
1.50	7.07	99.74 %	99.63 %	0.12 %	0.37 %
1.50	5.0	99.47 %	99.02 %	0.35 %	0.97 %
1.50	3.16	99.11 %	99.79 %	0.62 %	1.21 %
0.75	3.16	99.64 %	99.33 %	0.35 %	0.66 %
0.31	3.16	99.69 %	99.48 %	0.31 %	0.51 %

Truncated cones:

Truncated cones are extensively used as they are seemingly easier to fabricate, and they generate some of the same results. The transmissions spectra for three truncated cones, and one full conic shape is presented in figure 45 below. It can be observed that the truncated cones are also subject to interference effects, but of a higher magnitude. The transmission also varies more than for the moth-eyes, although the 1.25 μm radius structure show remarkable transmission results, with transmission of 99.9% at 8.2 μm, with a dip on the centre 8-12 range, but this can likely be designed to have a peak at around 10 μm. But, the same structure also had an average transmission in the 3-5 μm range of 99.4 %.

Figure 45: *Transmission spectra for truncated cone structures. The units given in the legend are all presented in μm. They are respectively bottom radius, top radius and structure height. 0 top radius means it is a completed triangle.*
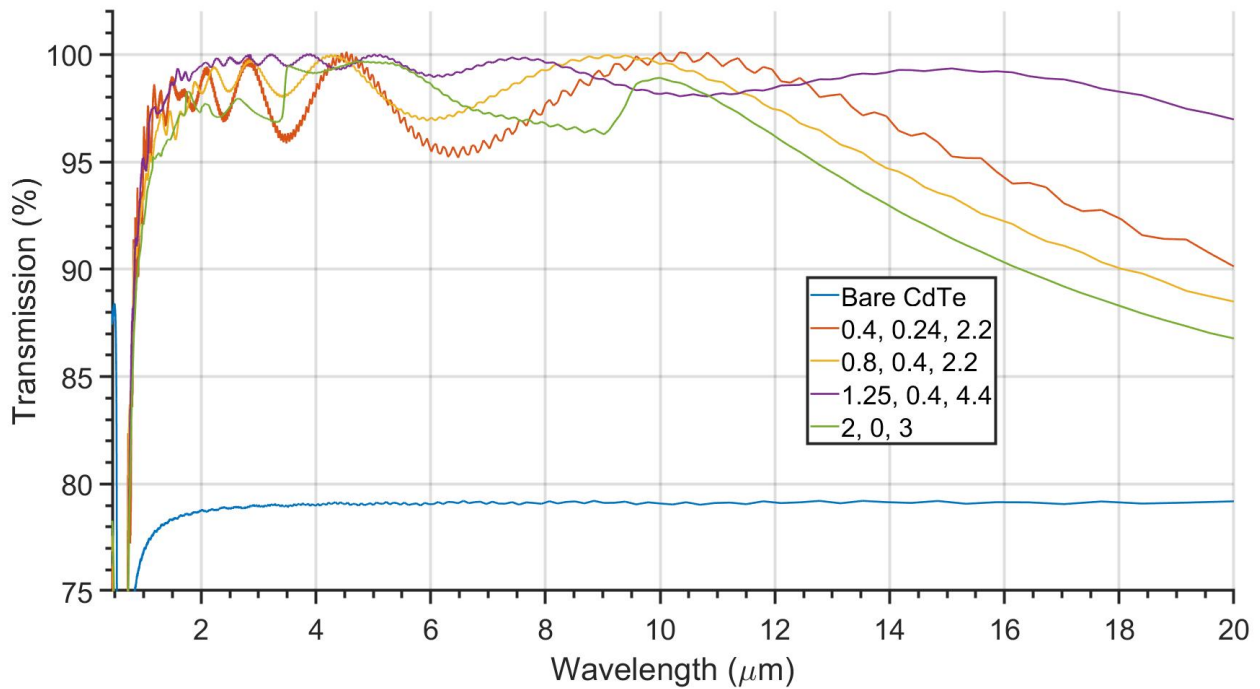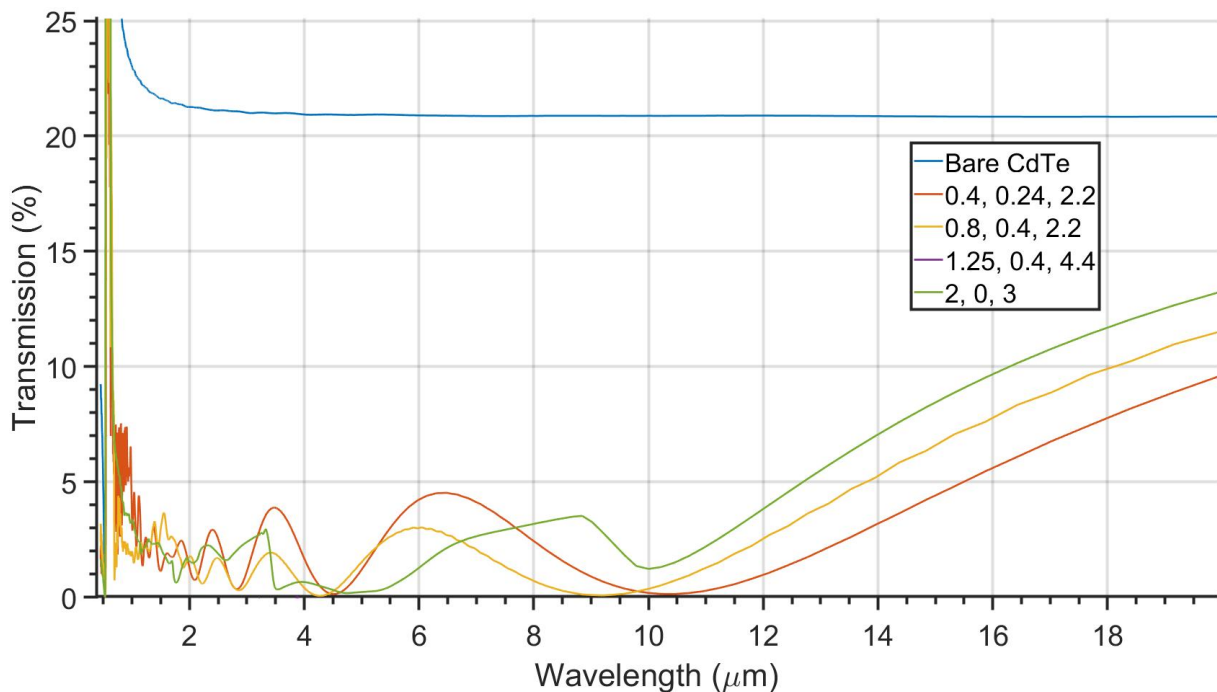

Figure 46: *Reflection spectra for truncated cone structures. The units given in the legend are all presented in μm. They are respectively bottom radius, top radius and structure height.*

Table 7: Averaged results around optimal ranges (3-5 and 8-12 μm)

$\mathbf{R}_{bottom}/\mathbf{R}_{top}$	$\mathbf{h}_0$	$\mathbf{T}_{avg}$(3-5 μm)	$\mathbf{T}_{avg}$(8-12 μm)	$\mathbf{R}_{avg}$(3-5 μm)	$\mathbf{R}_{avg}$(8-12 μm)
0.4/0.24	2.2	97.94 %	99.20 %	2.04 %	0.79 %
0.8/0.4	2.2	98.98 %	99.33 %	1.03 %	0.64 %
1.25/0.4	4.4	99.70 %	98.64 %	0.30 %	1.37 %
2.0/0.0	3.0	98.60 %	97.41 %	1.12 %	2.55 %

Anti moth-eye structures:

Anti moth-eye structures were presented in the literature with varying degrees of success, but it presented itself as an interesting structure regardless. When looking at the gradient of the refractive index (as presented in figure 16), the anti moth-eye structures surely have the smoothest curve, but it seems this is not the only important factor for good transmission. The reproduced results of four different structures from the literature is presented in figures 47 and 48. The yellow plot in figure 47 shows a >98% transmission in the 3-5 μm range, but with a very early transmission limit, as the transmissions drop towards $\approx$ 80% quickly. It seems that at longer wavelengths, the structures are not observed by the waves as AR structures, but rather as bare substrate.
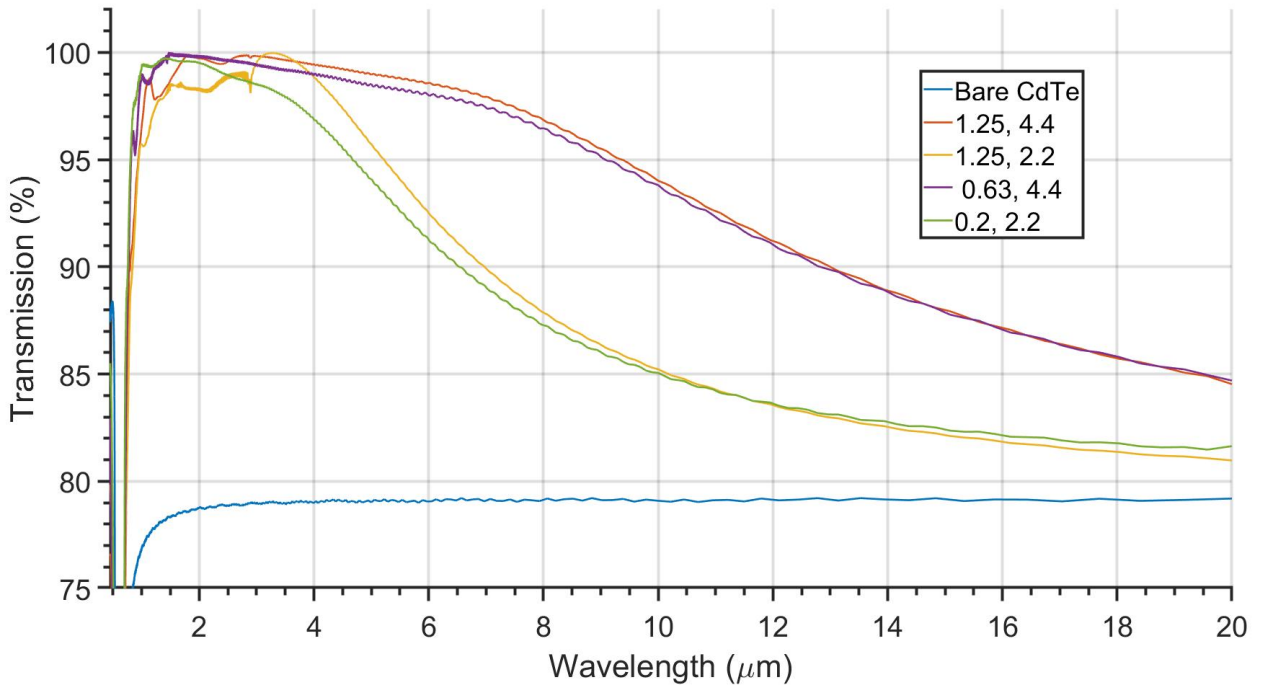

Figure 47: *Transmission spectra for Anti-moth-eye structures. The units given in the legend are all presented in μm. They are respectively bottom radius and structure height.*

Figure 48: *Reflection spectra for Anti-moth-eye structures. The units given in the legend are all presented in μm. They are respectively bottom radius and structure height.*
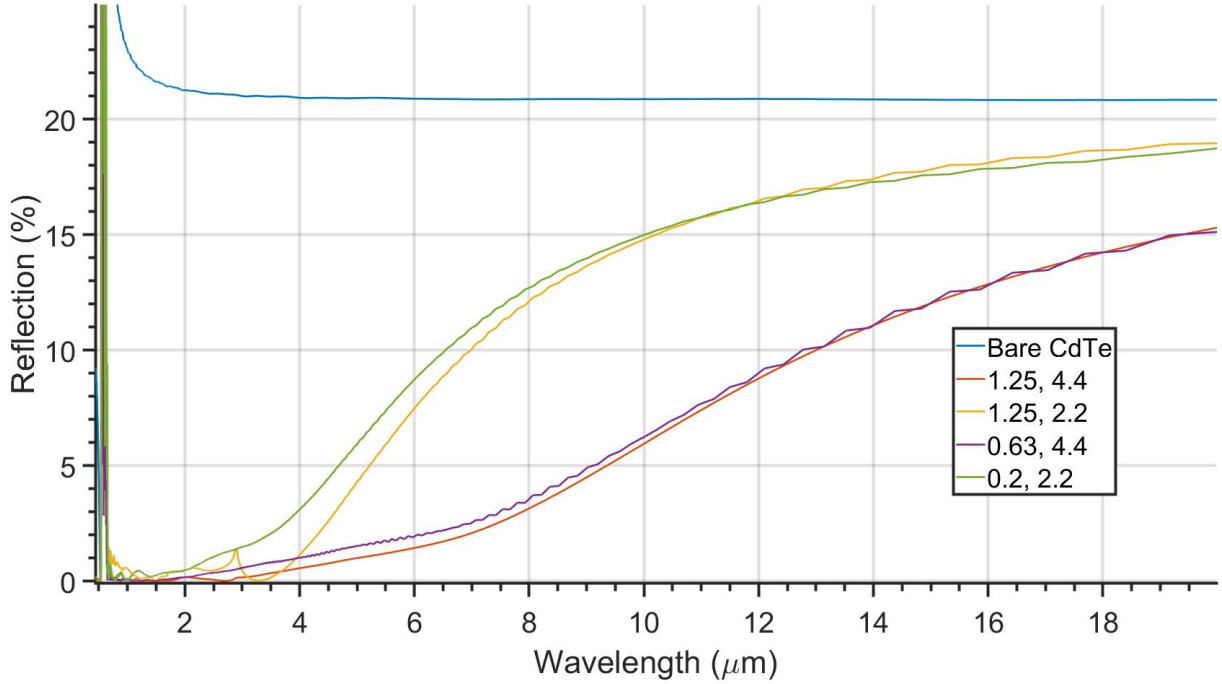
Table 8: Averaged results around optimal ranges (3-5 and 8-12 μm)

$\mathbf{R_0}$	$\mathbf{h_0}$	$\mathbf{T}_{avg}(\text{3-5 }\mu\text{m})$	$\mathbf{T}_{avg}(\text{8-12 }\mu\text{m})$	$\mathbf{R}_{avg}(\text{3-5 }\mu\text{m})$	$\mathbf{R}_{avg}(\text{8-12 }\mu\text{m})$
1.25	4.4	99.51 %	94.46 %	0.50 %	5.53 %
1.25	2.2	98.86 %	85.67 %	1.17 %	14.33 %
0.625	4.4	99.04 %	94.13 %	0.96 %	5.86 %
0.2	2.2	97.08 %	85.41 %	2.95 %	14.59 %

Colloid structures:

Colloids were not necessarily believed to have as much potential as the other structures, but serves as a potentially cheaper and easier method of reaching > 90% transmission over the 3-5 and 8-12 μm ranges. It is believed cheaper and easier as the deposition of colloids is already used extensively in colloidal lithography, which is one one the common techniques of etching micro-structures [43]. From the transmission spectra presented below in figure 49, it is possible to see that the three structures have the same transmission "fingerprint", but dragged out over a longer range for the larger structures. Observe the yellow peak at 2.3 μm, and see that this is the same peak as the purple at 5 μm. This implies that it is possible to design a structure size where these peaks are present in the desired intervals (3-5 and 8-12 μm). The purple 2.5 μm structure already peak around 5 μm, so reducing the sizes somewhat, will allow it to peak at 4 μm. Additionally, increasing the size could generate another peak closer to 10 μm. This design is attempted later in this section.

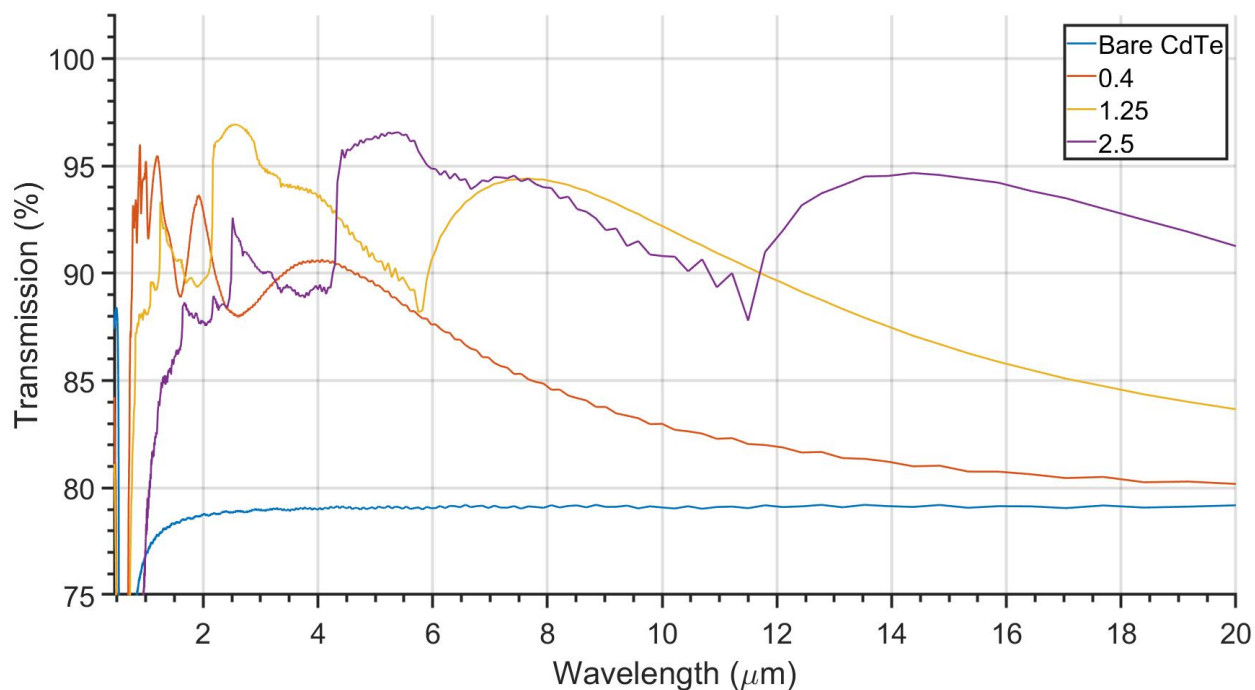**Figure 49:** *Transmission spectra for colloid structures. The units given in the legend are the radius for the colloids.*
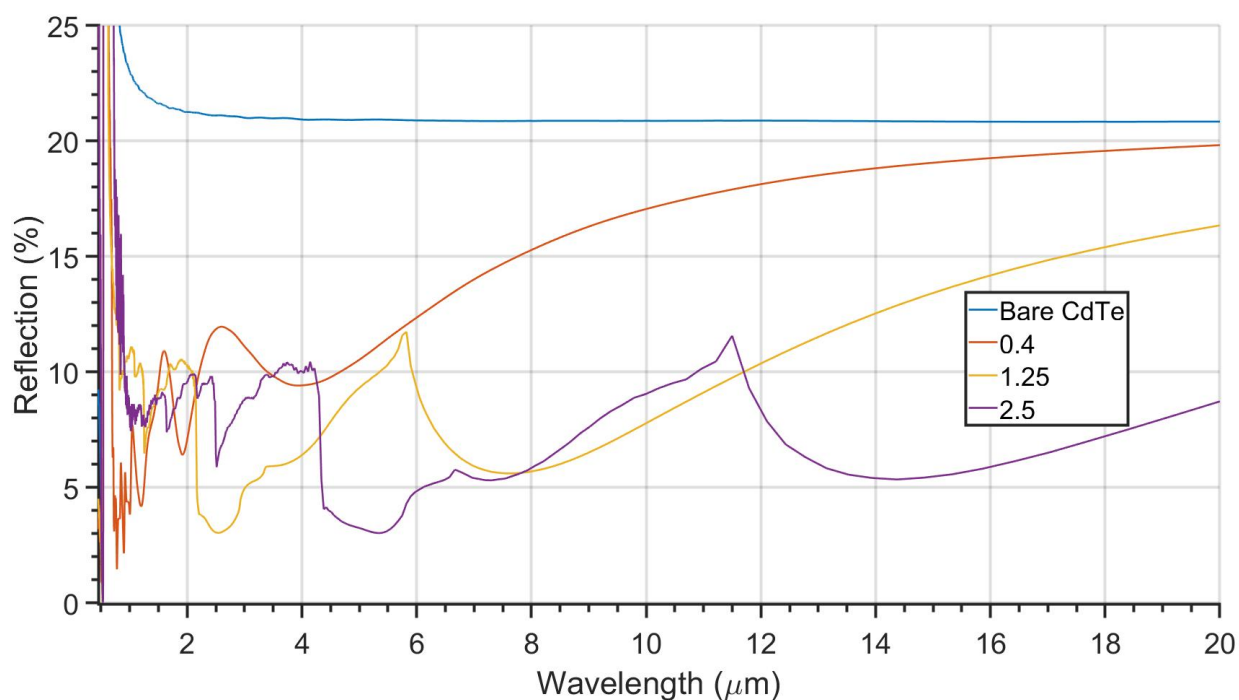

Figure 50: *Reflection spectra for colloid structures. The units given in the legend are the radius for the colloids.*

Table 9: Averaged results around optimal ranges (3-5 and 8-12 μm) for colloid structures

R	$\mathbf{T}_{avg}$(3-5 μm)	$\mathbf{T}_{avg}$(8-12 μm)	$\mathbf{R}_{avg}$(3-5 μm)	$\mathbf{R}_{avg}$(8-12 μm)
0.40	90.03 %	83.26 %	9.97 %	16.74 %
1.25	93.49 %	92.51 %	6.50 %	7.49 %
2.5	91.00 %	91.45 %	8.27 %	8.42 %

4.2.6   Optimal parameters for ARMS in the 3-5 μm and 8-12 μm range:

Using the results presented above, it was possible to tailor further improvements to the micro-structures by slightly changing the radius or heights to place the transmission peaks at more favourable wavelengths, and as such the results of this optimisation is presented below. Some of the earlier results can qualify as optimal results, and so some earlier simulation results are presented as well, as their transmission levels are excellent.

Optimal moth-eye:
The moth-eye structures simulated and presented in table 43 were already very good, and little improvement was done to achieve the optimal structures presented below in figures 51 and 52. The only change was making the structures taller so that the total transmission increased, and an "optimal" height was chosen such that the interference patters peaked in a more optimal wavelength.
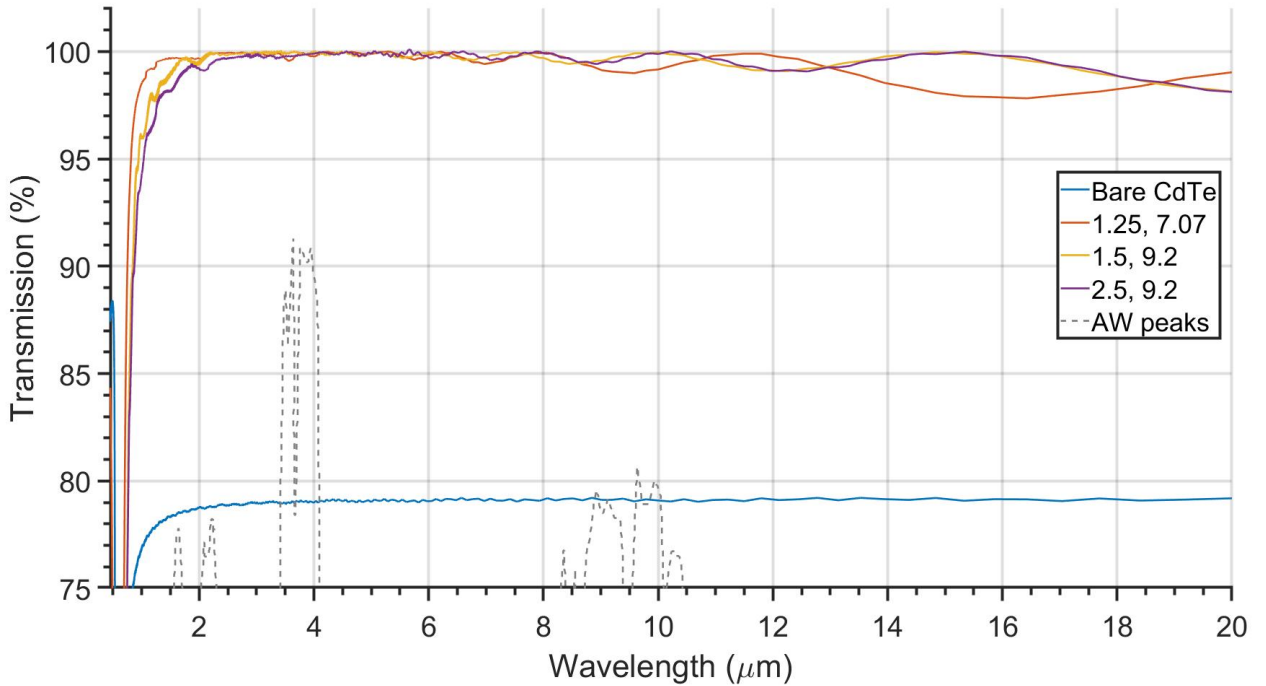

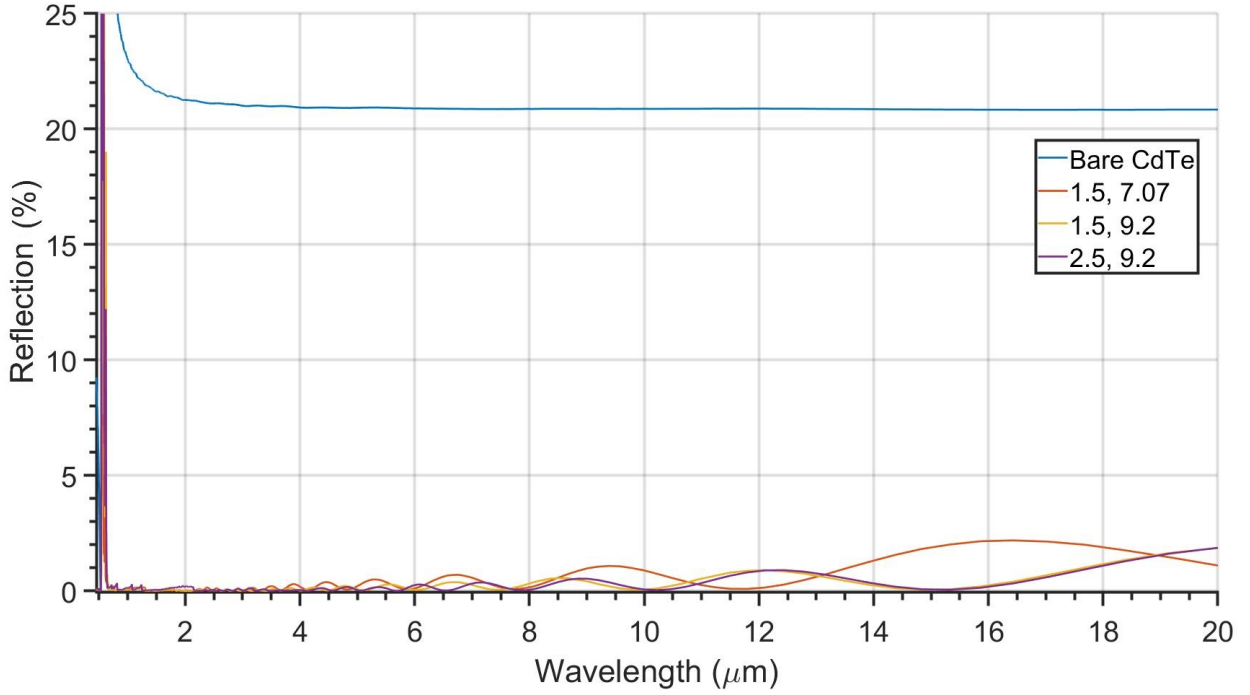***Figure 51:*** *Transmission spectrum for the best moth-eye ARMS.*

Figure 52: *Reflection spectrum for the best moth-eye ARMS.*

Table 10: Best averaged results around optimal ranges (3-5 and 8-12 μm) for moth-eye structures. *These are presented earlier, and deemed optimal for these ranges.

$\mathbf{R}_0$	$\mathbf{h}_0$	$\mathbf{T}_{avg}$(3-5 μm)	$\mathbf{T}_{avg}$(8-12 μm)	$\mathbf{R}_{avg}$(3-5 μm)	$\mathbf{R}_{avg}$(8-12 μm)
1.5	9.2	99.92 %	99.60 %	0.07 %	0.40 %
2.5	9.2	99.84 %	99.66 %	0.05 %	0.33 %
1.5*	7.07	99.74 %	99.63 %	0.12 %	0.37 %

Optimal truncated cones:
The truncated cones sourced from the literature and presented above show surprisingly high transmission, and competes with the moth-eye structures, at least in the 3-5 μm range. The improvements made on the structures to optimise them were to find the best ratio for top and bottom radius, and optimise the height with the interference. The fruits of this labour is presented below in figures 53 and 54, and in table 11.
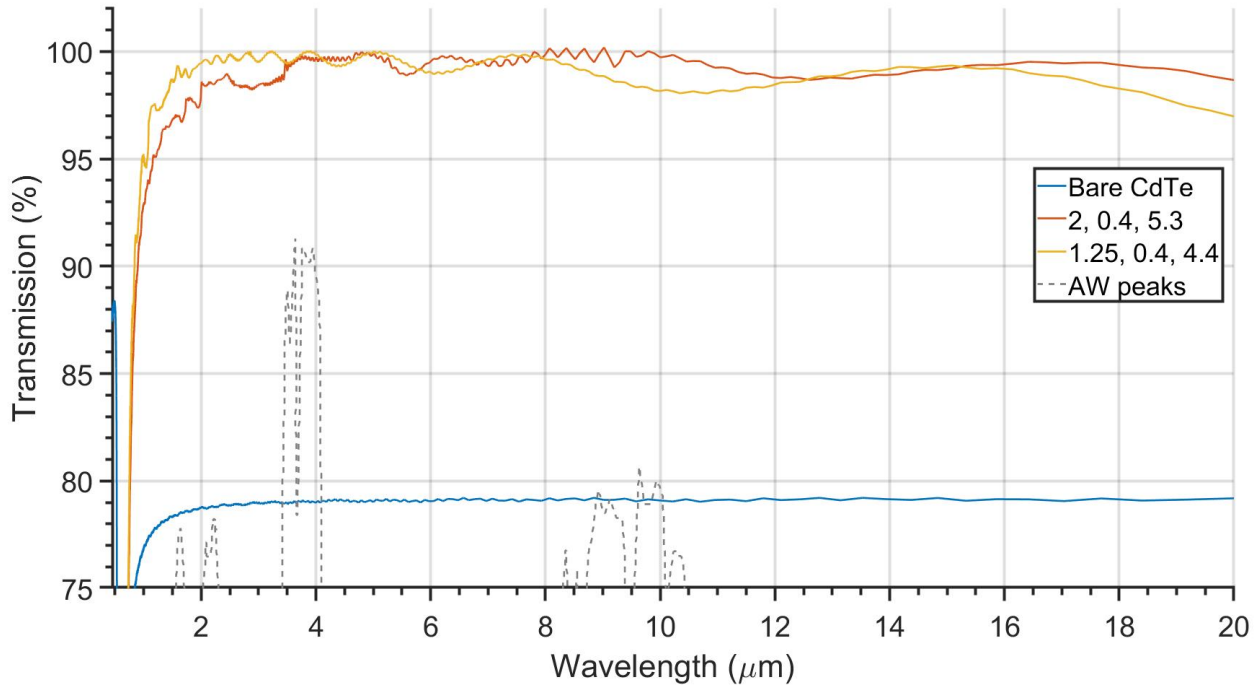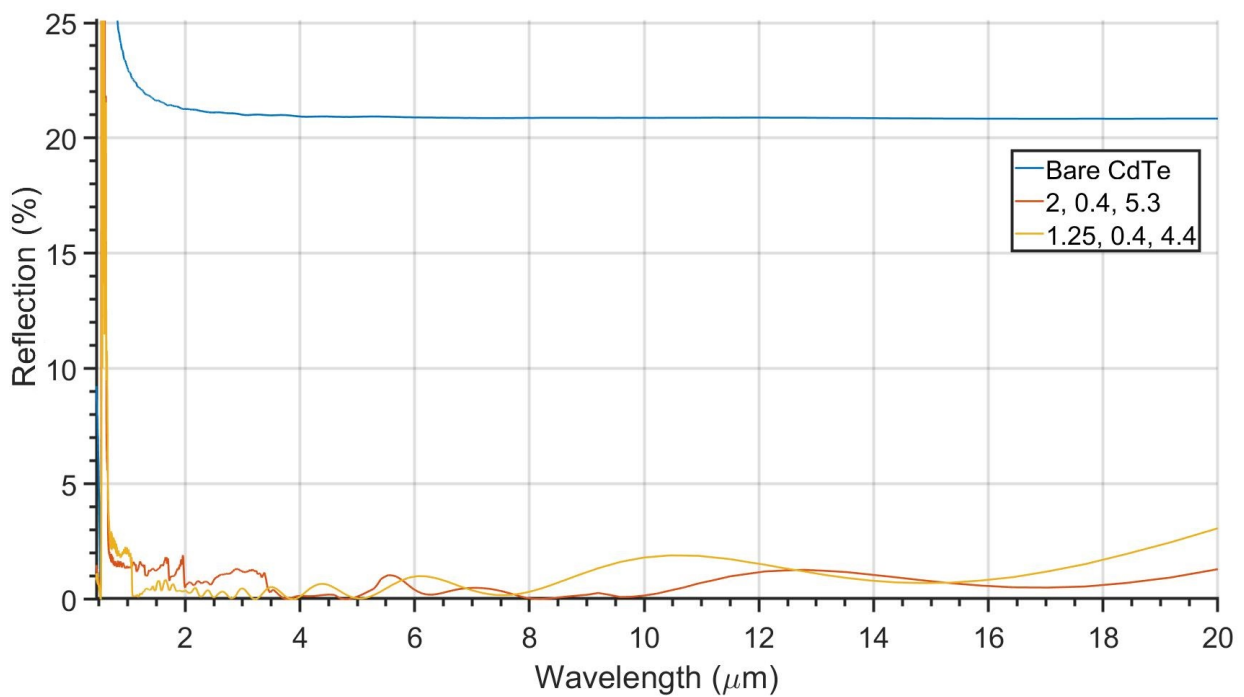
Figure 53: *Transmission spectrum for the best TC ARMS.*

Figure 54: *Reflection spectrum for the best TC ARMS.*

Table 11: Best averaged results around optimal ranges (3-5 and 8-12 μm) for truncated cone structures. *These are presented earlier, and deemed optimal for these ranges.

$\mathbf{R}_{bottom}/\mathbf{R}_{top}$	$\mathbf{h}_0$	$\mathbf{T}_{avg}$(3-5 μm)	$\mathbf{T}_{avg}$(8-12 μm)	$\mathbf{R}_{avg}$(3-5 μm)	$\mathbf{R}_{avg}$(8-12 μm)
2/0.4	5.3	99.30 %	99.65 %	0.46 %	0.33 %
1.25/0.4*	4.4	99.70 %	98.64 %	0.30 %	1.37 %

Optimal anti moth-eye:

The anti moth-eye structures showed bad broad-band transmission over the range, as it the transmission quickly decayed towards the substrate transmission-levels of around 70%. For all the other structures, increasing the height seemed to increase the transmission over the whole ranges, but showed to improve transmission in low-transmission areas even further. Therefore, this was used on the AME structures, and the broadband transmission increased, as seen in figures 55 and 56, and in table 12.
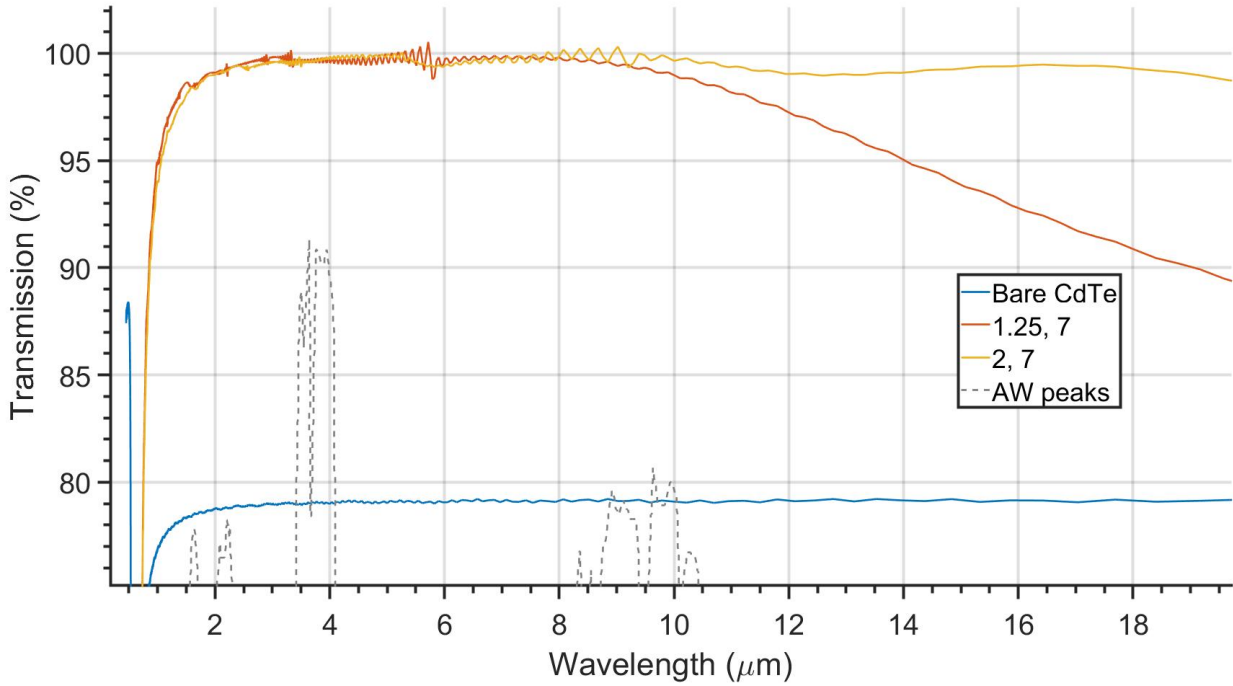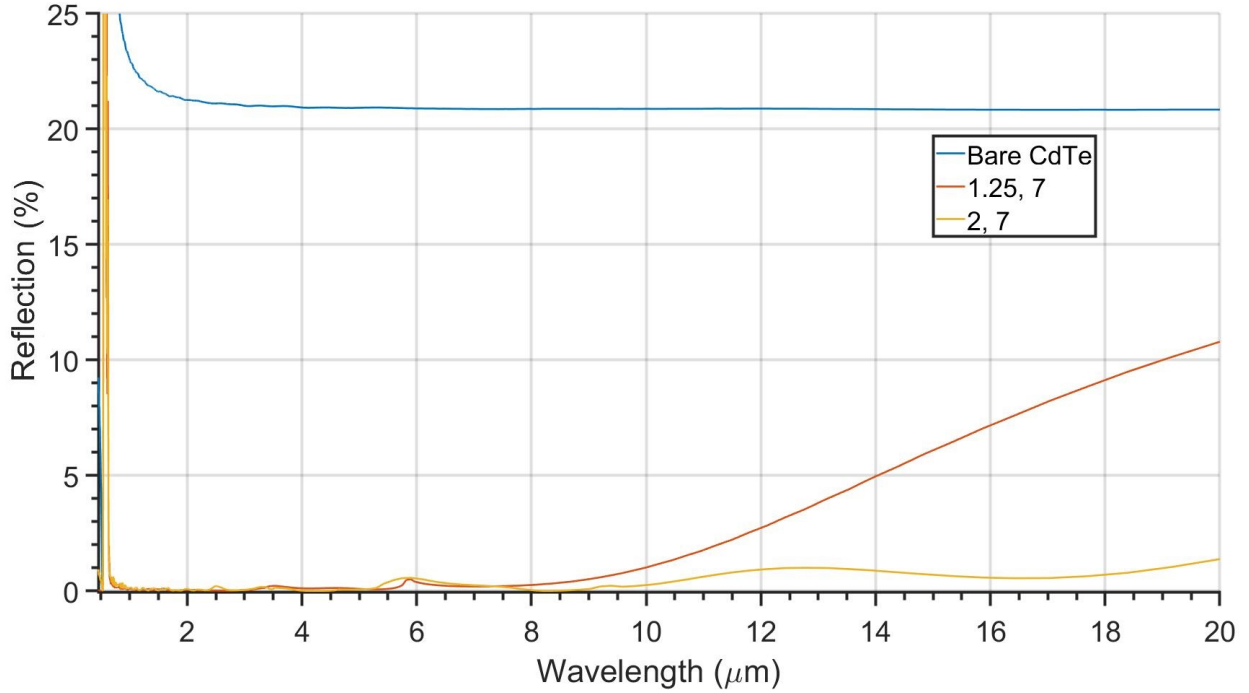

Figure 55: *Transmission spectrum for the best AME ARMS.*

Figure 56: *Reflection spectrum for the best AME ARMS.*

Table 12: Averaged results around optimal ranges (3-5 and 8-12 μm) for AME structures

$\mathbf{R}_0$	$\mathbf{h}_0$	$\mathbf{T}_{avg}$(3-5 μm)	$\mathbf{T}_{avg}$(8-12 μm)	$\mathbf{R}_{avg}$(3-5 μm)	$\mathbf{R}_{avg}$(8-12 μm)
1.25	7.0	99.7 %	98.98 %	0.13 %	1 %
2.0	7.0	99.70 %	99.69 %	0.07 %	0.29 %

Optimal colloids:
The method of depositing colloids into the substrate as an ARMS proved itself to be a relatively good choice for IR transmission, with $> 90\%$ transmission in most of the optimal ranges. For the colloids, there is only one free parameter to change for optimisation, and observing that the transmission spectra for the colloids in figure 49 show a specific "fingerprint", it is possible to place this fingerprint such that the two highest peaks land on the optimal ranges (3-5 and 8-12 μm). This was done by trying different radii for the colloids, and the results of this optimisation is presented below in 57 and 58, and in table 13.
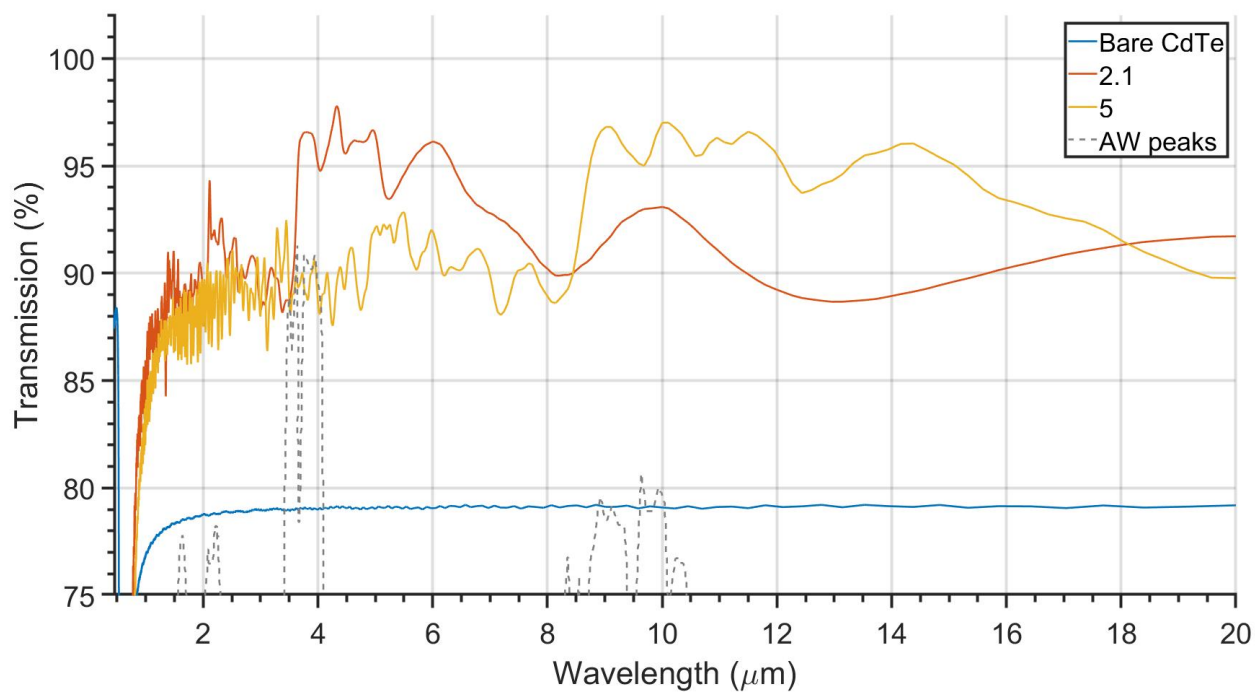
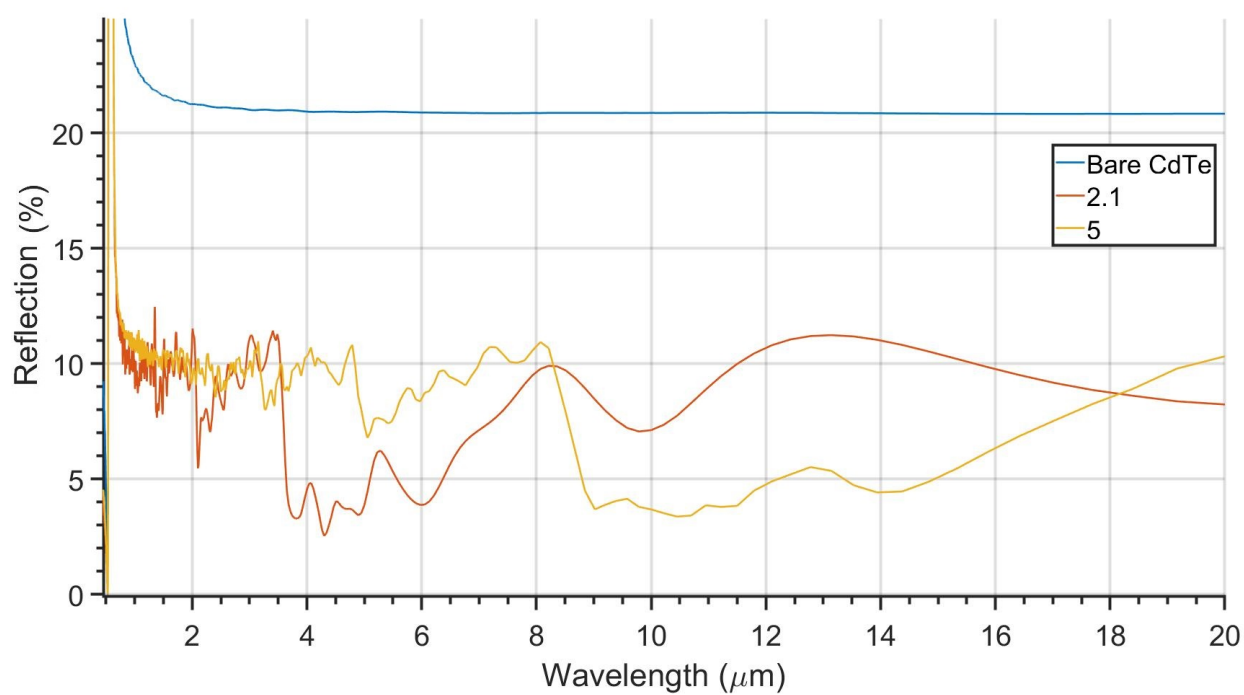**Figure 57:** *Transmission spectrum for the best Colloid ARMS.*

Figure 58: *Reflection spectrum for the best Colloid ARMS.*

Table 13: Averaged results around optimal ranges (3-5 and 8-12 μm) for colloid structures

R	$\mathbf{T}_{avg}$(3-5 μm)	$\mathbf{T}_{avg}$(8-12 μm)	$\mathbf{R}_{avg}$(3-5 μm)	$\mathbf{R}_{avg}$(8-12 μm)
2.1	93.18 %	91.25 %	6.54 %	8.64 %
5.0	89.59 %	94.6 %	9.51 %	5.15 %

4.3 Reference material - Silicon simulations

Silicon was selected as a reference material as it is cheap and expendable, as compared to CdTe. The simulation results for the same setups as for CdTe is presented below. The refractive index dataset was sourced from Palik. Silicon is used as experimental substitute for CdTe only for the anti-reflective coating part. And as such, the same foundation up to and not including ARMS are presented below.

4.3.1 Smooth surface

To first compare Silicon to CdTe, Si was simulated with a smooth surface with the same parameters as for the CdTe simulations such that broadband transmission and reflection spectra was acquired. The simulations showed that the higher refractive index of Si (n$\approx$ 3.43) prevent about 8% of the broadband transmissivity as compared to CdTe (n$\approx$ 2.73).
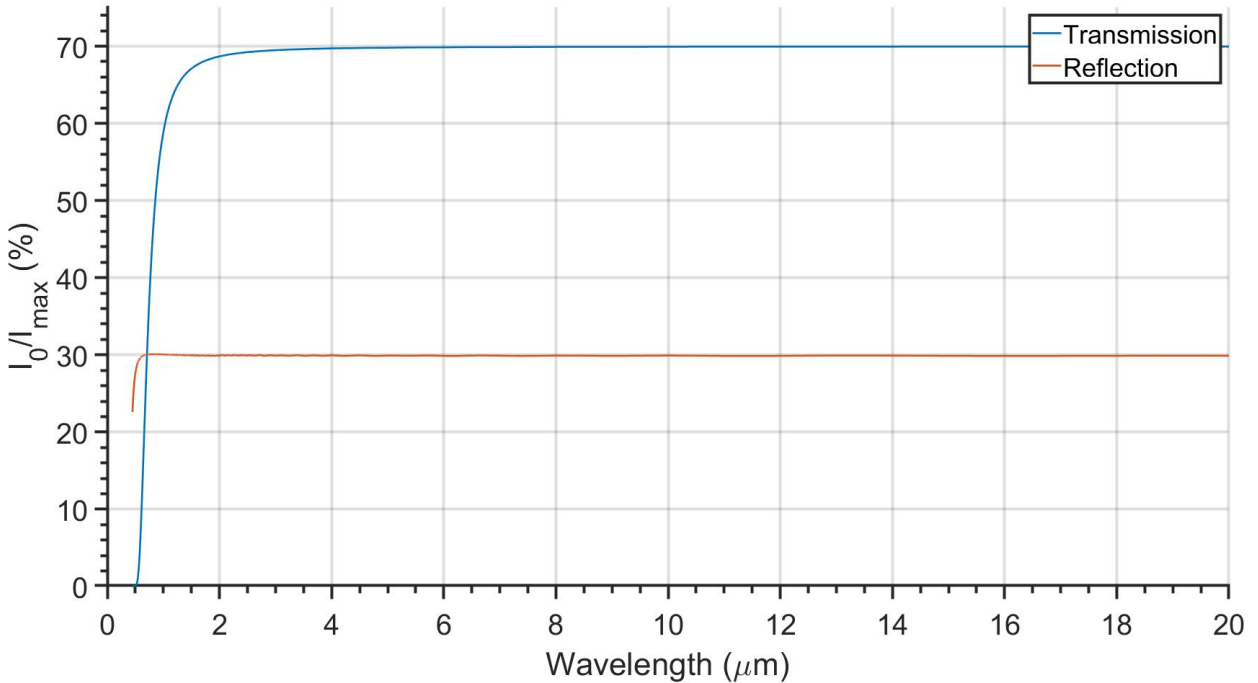

Figure 59: *Transmission and Reflection simulation results for smooth Si surface*

4.3.2 Rough surface

Just as with CdTe, higher roughness causes better transmission, depending on the roughness. A very rough surface Si substrate is plotted below with 0.3 μm RMS. The same

effect is observed here as for CdTe, and as expected. The transmission increases over ranges determined by the sizes of the surface structures in the rough surface.
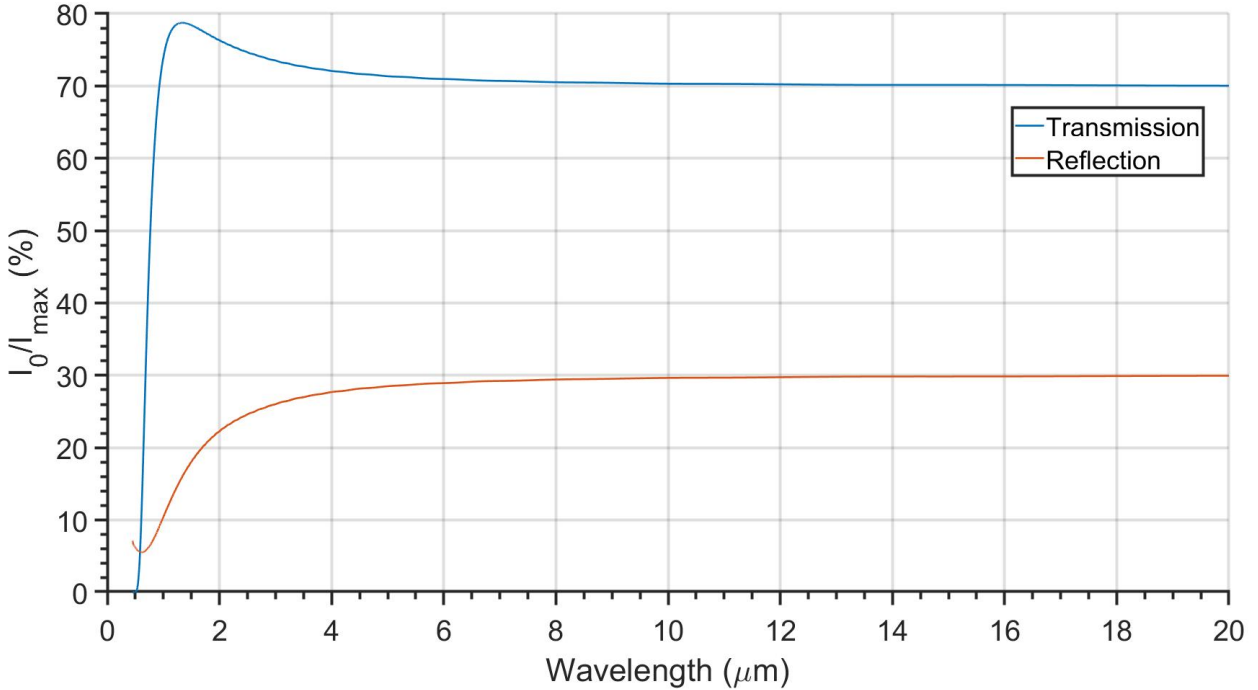
Figure 60: *Transmission and Reflection for rough Si surface*

4.3.3 Anti-reflective coating

Here, the same procedure as for CdTe is performed for Si, and the parameter selection table for ARCs is again included with the simulations results for the transmission. The atmospheric window is included in the background to illustrate the alignment of the transmission peaks of the atmosphere and the peaks from the ARC. Both DLC and ZnO showed promise to work as a dual-band transmitter, as high peaks were observed on both sides of the H_2O absorption band at 6 μm, and so it must be mentioned that they were here optimised for two wavelengths in the 10.33 μm peak optimisation. The 4.08 μm and 10.33 μm peaks have a coinciding thickness of 1.61 μm, and so two peaks will be visible on each side of the atmospheric window.

Figure 61: *0.45-20 µm transmission spectra with Silicon as substrate, and ZnO as thin-film*
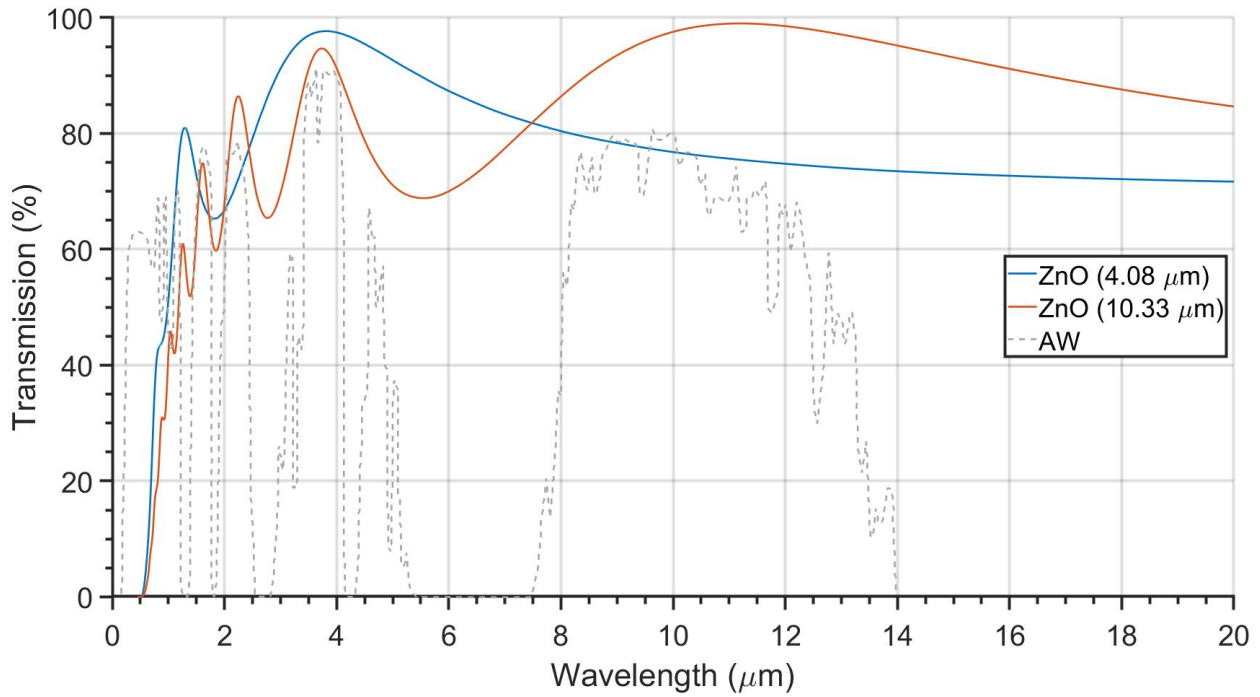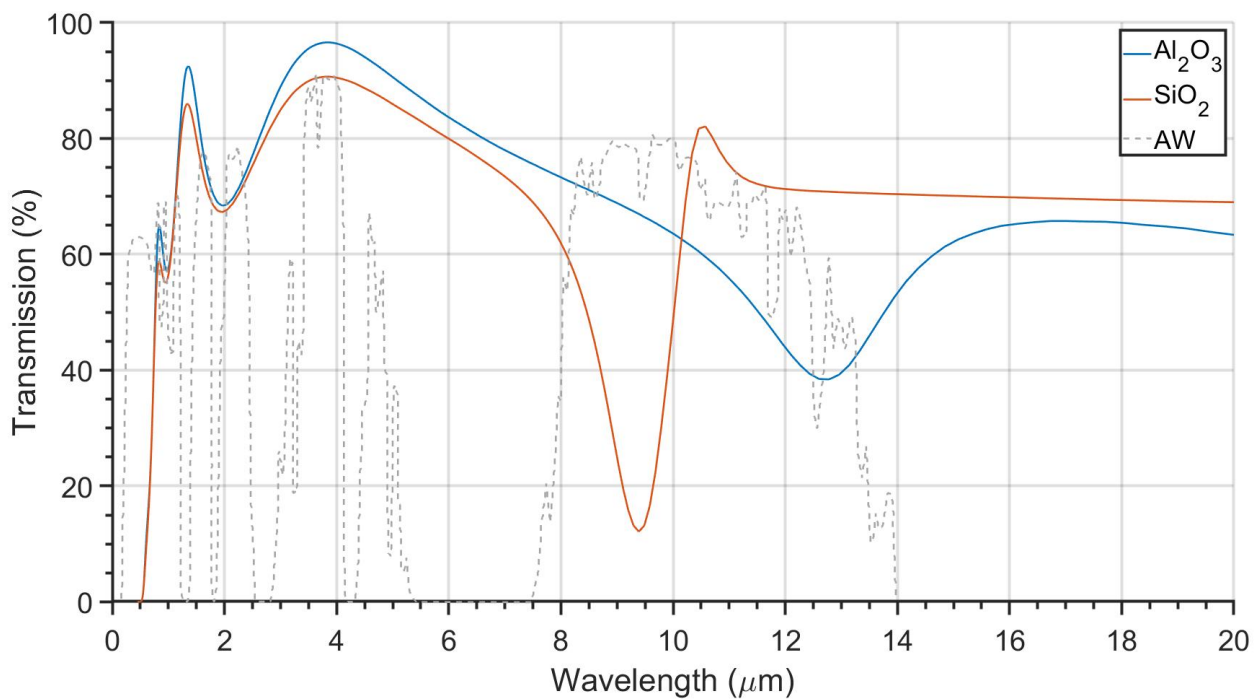

Figure 62: *0.45-20 µm transmission spectra for Si with Sapphire and quartz as ARC.*
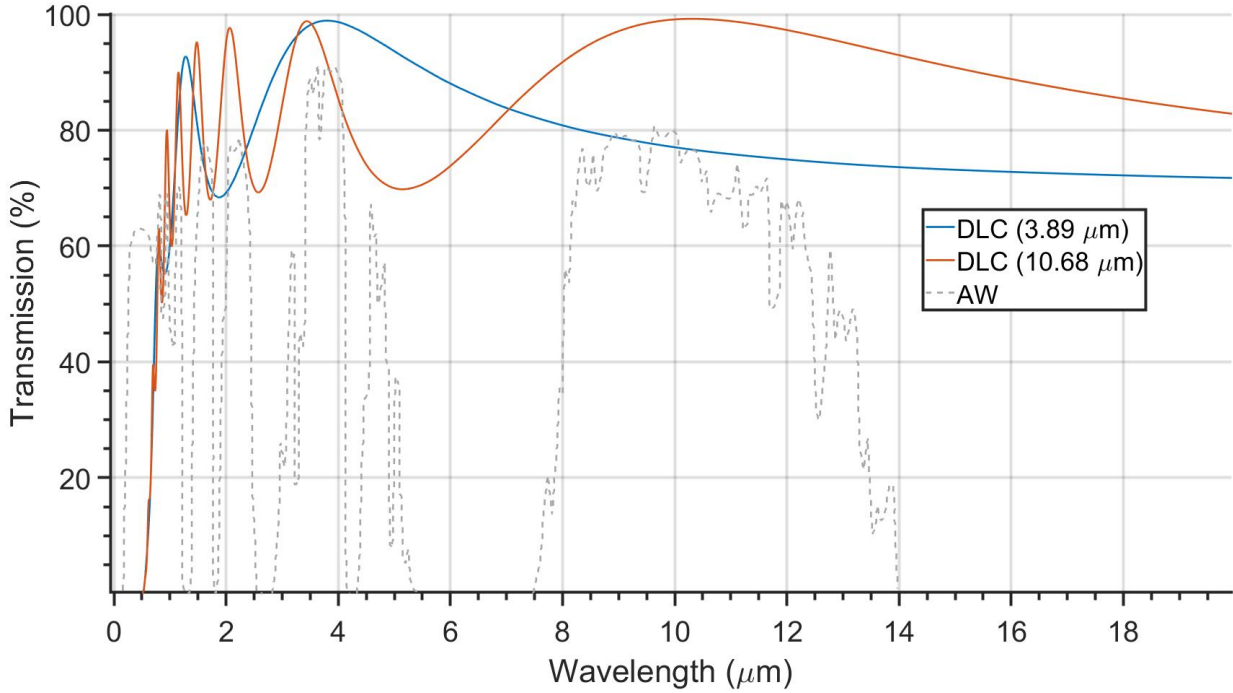
Figure 63: *0.45-20 μm transmission spectra for Si with DLC as ARC.*

Table 14: Averaged results for optimal thicknesses around optimal ranges (3-5 and 8-12 μm) for ARCs.

Material	t(μm)	$\mathbf{T}_{avg}$(3-5 μm)	$\mathbf{T}_{avg}$(8-12 μm)	$\mathbf{R}_{avg}$(3-5 μm)	$\mathbf{R}_{avg}$(8-12 μm)
$ZnO(1)$	0.54	95.68 %	77.47 %	2.36 %	22.38 %
$ZnO(2)$	1.61	83.87 %	94.89 %	11.63 %	4.31 %
Al_2O_3	0.62	94.18 %	63.74 %	5.01 %	31.29 %
SiO_2	0.69	88.85 %	51.21 %	8.95 %	34.02 %
$DLC(1)$	0.47	96.87 %	77.76 %	2.73 %	22.19 %
$DLC(2)$	1.28	87.01 %	97.17 %	12.62 %	2.77 %

Comparing these results to the ones for CdTe, they are extremely similar, with some differences, but with no consistent changes. For this reason, Si shows it self to be an excellent replacement for CdTe for these materials and these thicknesses, at least in simulation. Transmission results from experiments will follow up on this.

71

5 Results and Discussion - Experiments

The simulation work done here is mostly to prepare for the experimental part. This is where the ideas presented are tested, and analyzed. The goal is to develop better transmission results for CdTe, by using simulation and a cheaper substrate to acquire the best solution. After the simulations were done, FTIR-spectra were taken of the different substrates. The CdTe chips have roughly the same roughness as the simulated roughness, and so the FTIR measurements will be compared to the rough samples.

5.1 CdTe measurements

CdTe is a very expensive material, and hence few experiments were performed with CdTe as a substrate, though some are presented below. AFM measurements were taken of the surface to more precisely determine the structure of the surface for the transmission simulations. Additionally, FTIR transmissivity measurements were taken of the substrate so a comparison between simulated and experimental FTIR measurements can be made.

5.1.1 CdTe surface structure after polish - AFM

The very first data collected was the AFM measurements of the surface of a polished CdTe substrate. This was to acquire the correct surface structure data for the rough-surface simulations. The results were used during simulations and predictions, but they are presented properly here. A AFM measurement of a 10x10 μm area of a CdTe substrate. The measurements were taken the AFM at the faculty of physics and technology, with a CSC17, 8nm silicon tip with force constant k = 0.18 N/m. This was done in non-contact dynamic mode with a driving voltage of 0.1V and tip oscillating at $\approx$ 310kHz.
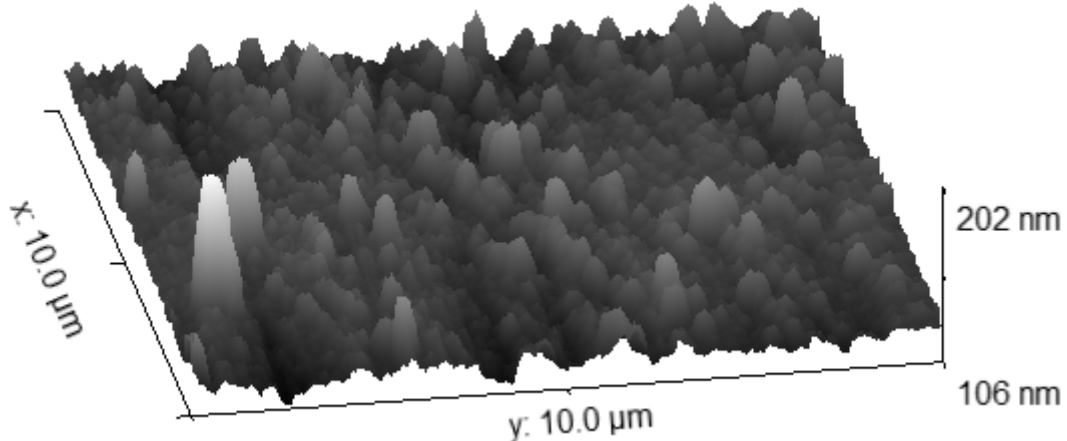
Figure 64: *AFM measurement of a CdTe substrate.*

The AFM measurements were mainly taken to extract the root-mean-square(RMS) value for the heights in the substrate, as well as the correlation length for the heights. These values are the most important ones in order to characterize the surface [7]. The RMS value extracted from figure 64 with GWYDDION was $\sigma = 7.140$ nm, and correlation length $\approx$ 100nm. These measurements were taken with dynamic non-contact mode, with a driving voltage of 0.1V and a tip oscillating at $\approx$ 310kHz.

5.1.2   Transmissivity of bare CdTe substrate - FTIR

Cadmium telluride has relatively good transmission properties without any treatment, as can be seen in the simulations results. Here the FTIR measurements of bare CdTe are presented. The absolute transmission is clearly lower than was predicted by the simulations, but it is almost as consistent as predicted. The lower transmission is explained mostly by the exclusion of back-side reflections in the simulations, as these generate quite a lot of interference noise. The predicted transmissions with back-side reflections included are approximately 20% lower than the presented transmissions above. It can therefore be argued that the simulated transmissions predict a transmission of around 58% in the $0.45 - 20\mu$m range. The correlation between simulation and experiment is therefore adequate.
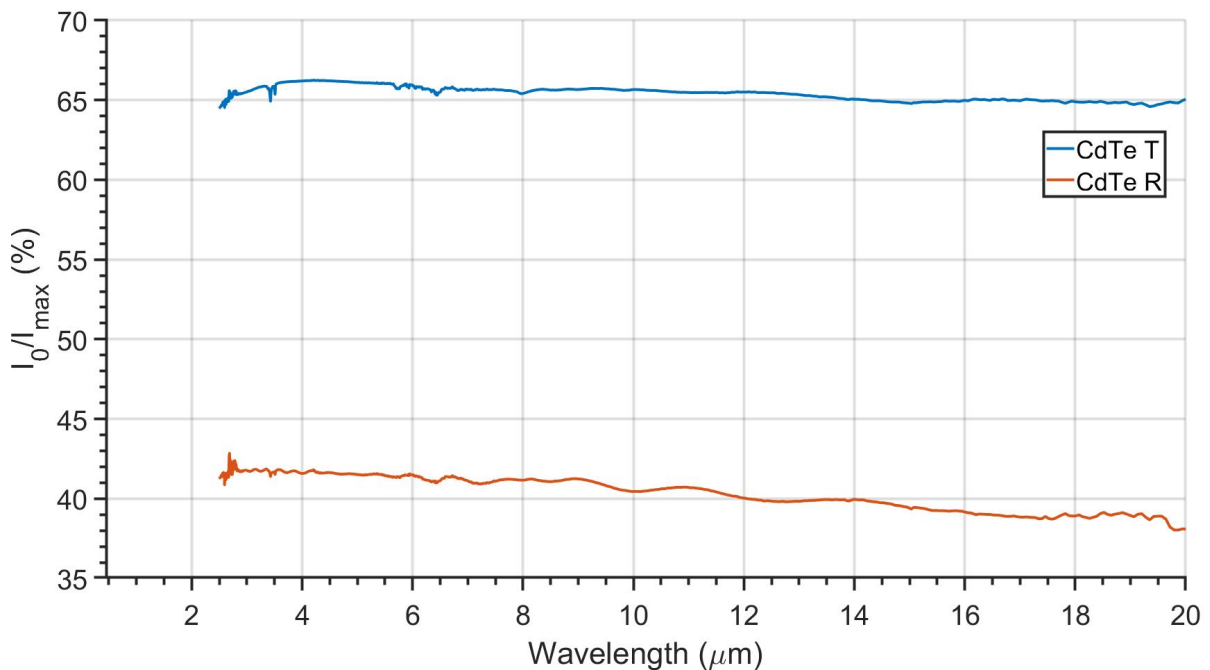
Figure 65: *Transmission and reflection spectra for the CdTe chip, without any AR treatment.*

5.2   Silicon measurements

Silicon was used as a substitute for CdTe in the experimental work, as it was expected that several substrates were to be designed and used, and this would be too expensive to attempt with CdTe. Therefore, the same experiments done on CdTe was also performed on silicon, such that the results can be used for comparison. AFM measurements were performed so that the surface roughness could be emulated more precisely. FTIR transmission measurements were done to observe the different transmission bands for the bare material as compared to CdTe. And lastly, a anti-reflective coating was applied to a silicon substrate by magnetron sputtering, at 600W, $2.4 * 10^{-2}$ mBar with a flow rate of 1.0 sccm with Argon. After this, FTIR and AFM measurements were performed on these samples.

5.2.1 Silicon surface structure - AFM

AFM measurements were taken of a silicon substrate to be used in the simulations to better defined the surface roughness for the simulations. The measurements were taken with the AFM at the faculty of physics and technology. Using a CSC17, 8 nm silicon tip with a force constant of 0.18 N/m, in dynamic non-contact mode with a driving voltage of 0.1V and a standard tip oscillating at ≈ 310kHz. The RMS for the surface was found with the help of GWYDDION analysis software to be around 12 nm. These results are presented in figure 66 below. The image has been aligned around its average to account for skewness, and each line-scan from the AFM has been realigned with the help of GWYDDION.

Figure 66: *AFM measurement of a silicon substrate that was used as substrate for ZnO ARC.*

5.2.2 Silicon transmissivity - FTIR

The simulated transmissions for Silicon lie consistently around $\approx 70\%$, whereas the measured transmission by FTIR are presented in figure 67. The large absorption differences over the IR range is due to the sharp absorption edges of silicon. At 16 μm, one such edge is clearly visible.
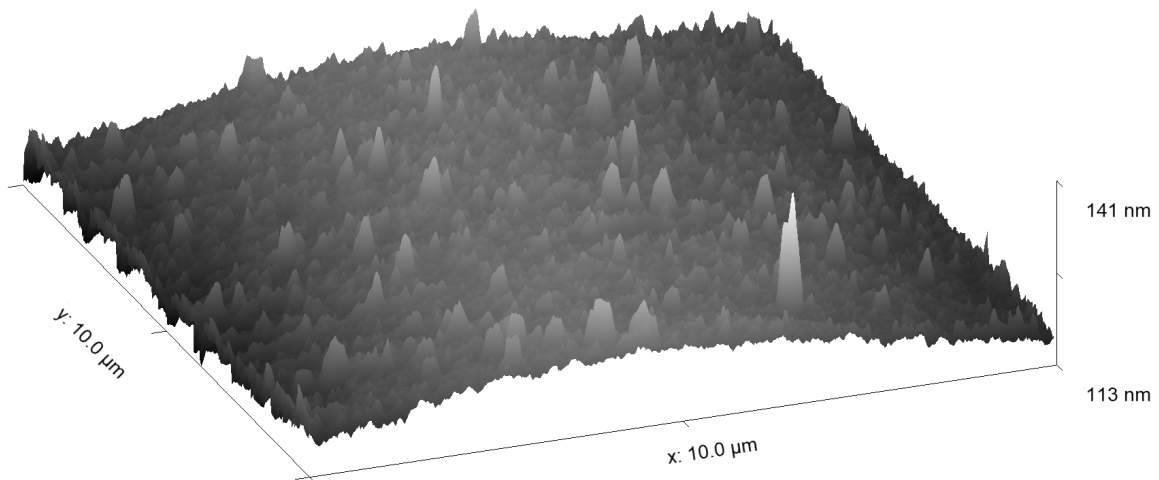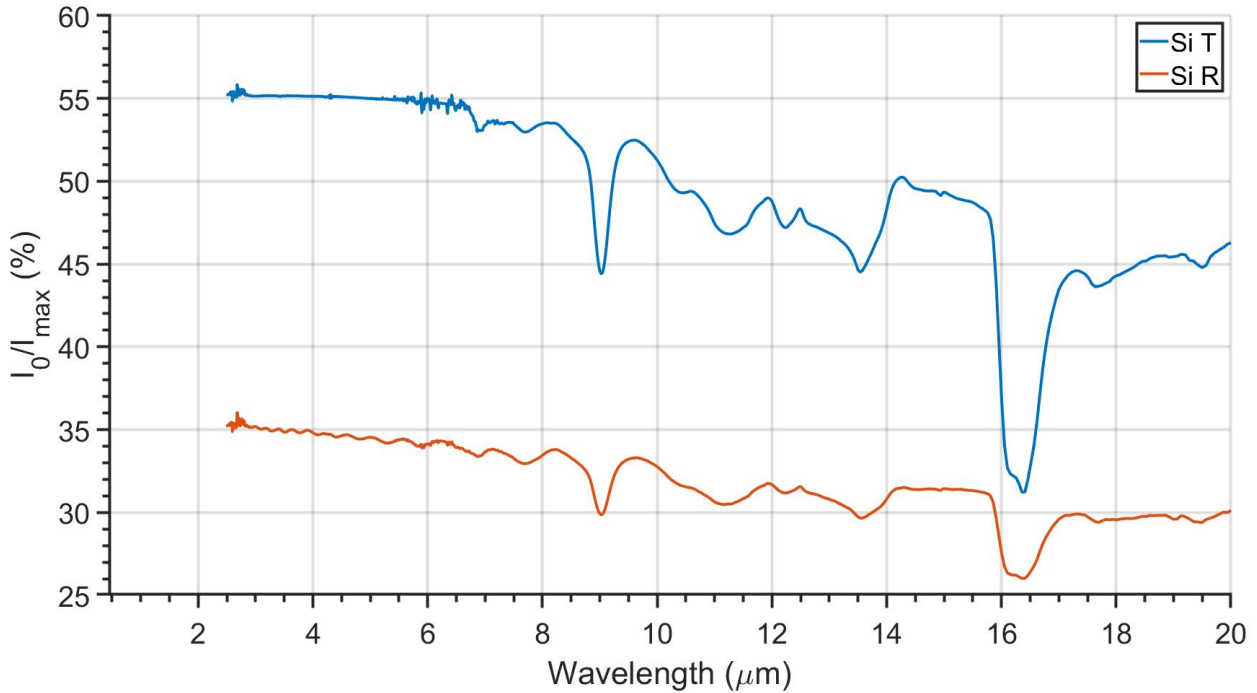
Figure 67: *Transmission and reflection spectra for the Si chip, without any AR treatment.*

5.2.3   ZnO Anti-reflective coating - FTIR

ZnO is relatively cheap, and is well known to be used as an anti-reflective coating. ZnO was deposited onto two 500μm thick silicon substrates, with coating thicknesses of $705 \pm$ (65) nm and $348 \pm$ (12) nm. These chips will be referred to as (1) and (2) respectively. A FTIR transmission measurement was then performed on the chips, and these are presented in figure 68, where only chip (2) had reflection measurements done as well. A clear improvement in transmission in the 3-5 μm can be seen for both chips, with a maximum difference of 13% above 5 μm. The transmission improvement visible *should* have been centered above 4 μm, which imply that the deposited film is either slightly too thick, or the predictions are slightly skewed on the x-axis. In any case, comparing with the simulated transmissions for the ZnO ARC, and applying the same argument for back side reflections, then the simulations still seem somewhat optimistic. The comparison can be seen in figure 69 below.
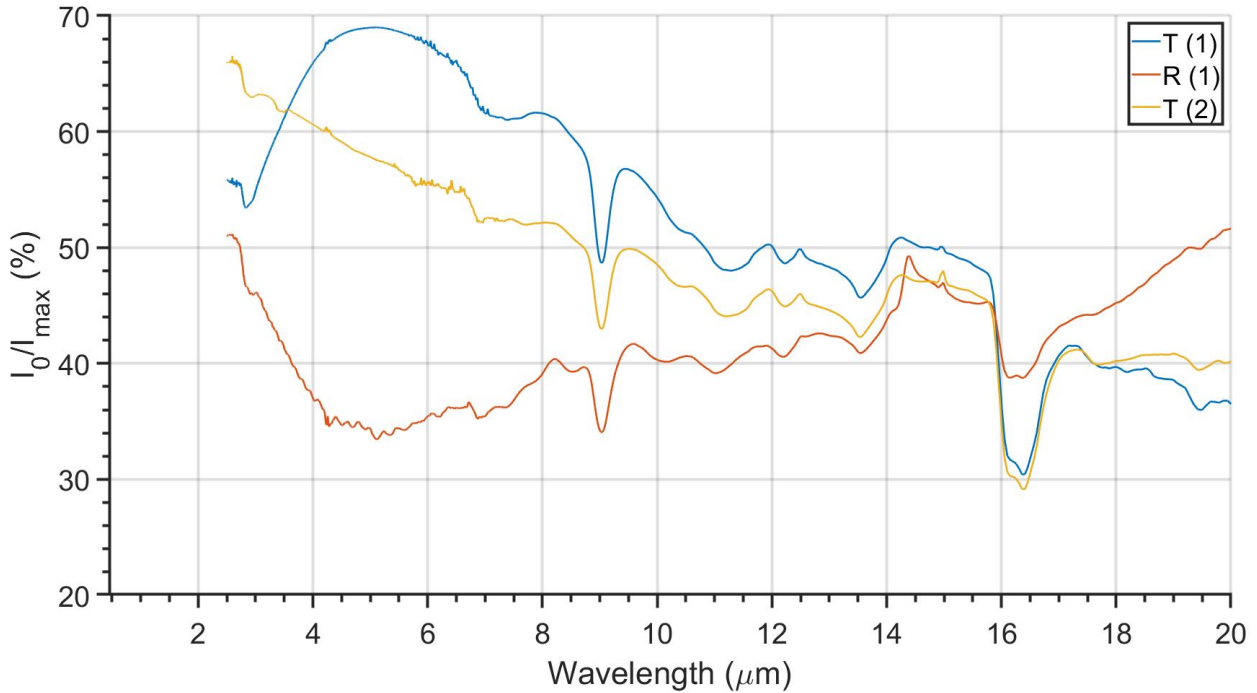
Figure 68: *Transmission and reflection spectra for silicon substrate with ZnO as ARC. Lumerical calculates the transmission and reflection independently of each other, and as a consequence, the sums of these can be > 100% in places, as discussed in the Lumerical chapter.*

The desired thicknesses for the substrates were 0.54 μm and 1.56 μm, instead of the measured 0.348 μm and 0.705 μm. This meant that new simulations had to be run to compare properly with these data. New simulations were run with the exact setup as in the ARC simulations performed earlier, but with ZnO ARC thickness of 0.348 μm and 0.705 μm. The results of this is presented in figure 69 below.
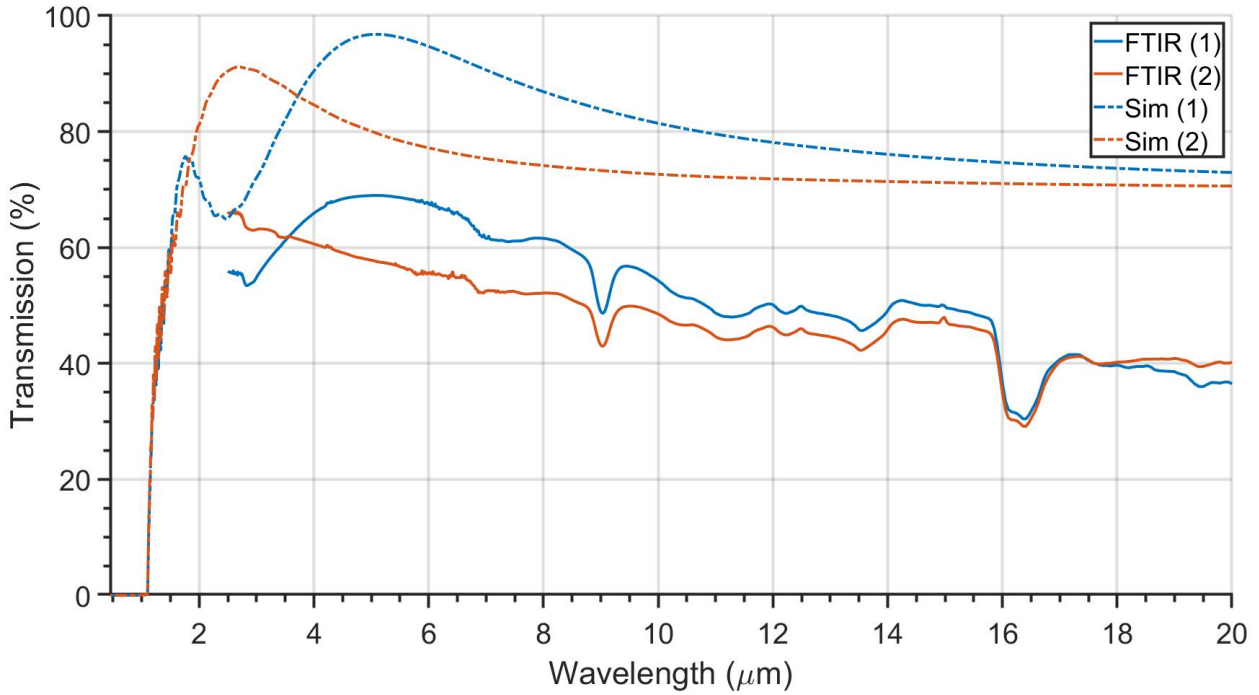
Figure 69: *FTIR measurements of silicon with ZnO ARC, and simulations of the same ARC thicknesses.*

In this spectrum, (1) is compared to the 348 nm simulation, and (2) to the 705 nm one. To better see the improvements of the ARCs to the transmission, one can subtract the FTIR spectrum of silicon from the spectrum including the ARC. This yields the difference in transmission, and is plotted below in figure 70. The improvement in transmission is clear - an increase of $\approx 12\%$ and $\approx 14\%$ on (1) and (2) respectively. Both of the chips miss the 3-5 μm window for which the transmission peak was intended, but these results still serve to show that these methods work well.
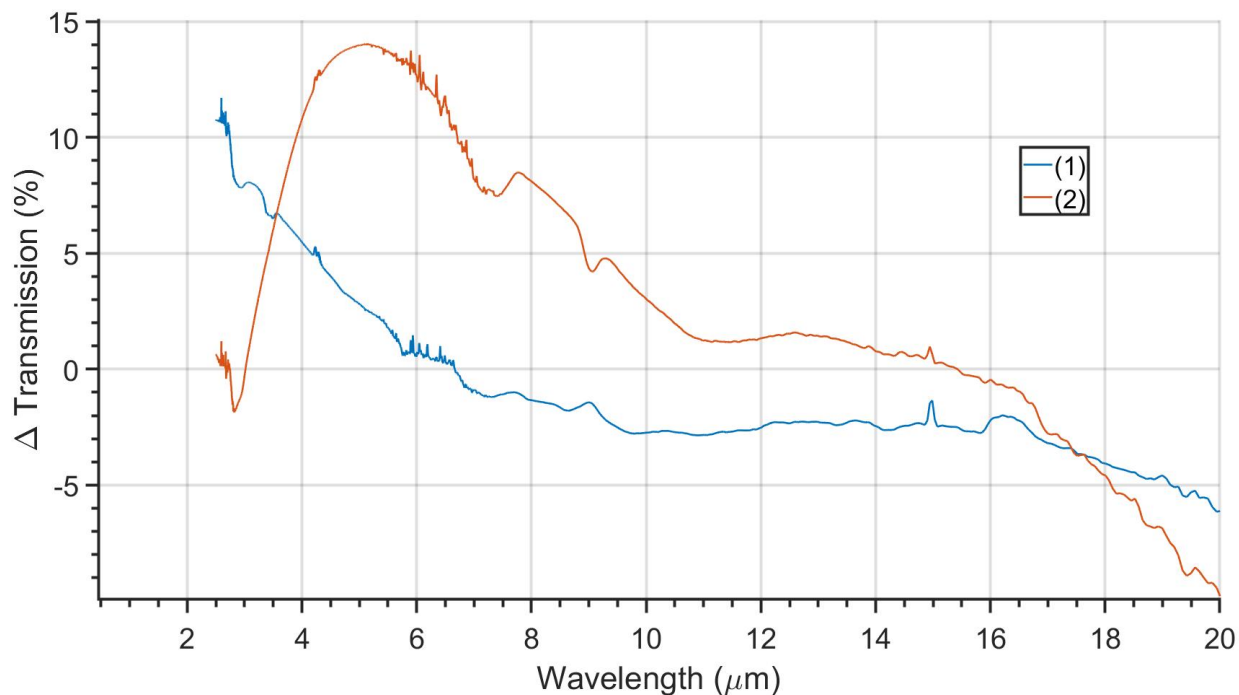
Figure 70: *Transmission difference between bare silicon and silicon coated with 348 nm and 705 nm ZnO.*

5.2.4   SEM measurements of ZnO ARC on Si

To achieve the precise measurement of the thickness of the ZnO ARC on Si, a SEM was used. Two coated chips were measured by snapping the chip in half, and then measuring the cross-section of the chip. The chips were found to have a relatively even thickness of $348 \pm (12)$ μm and $705 \pm (65)$ μm.
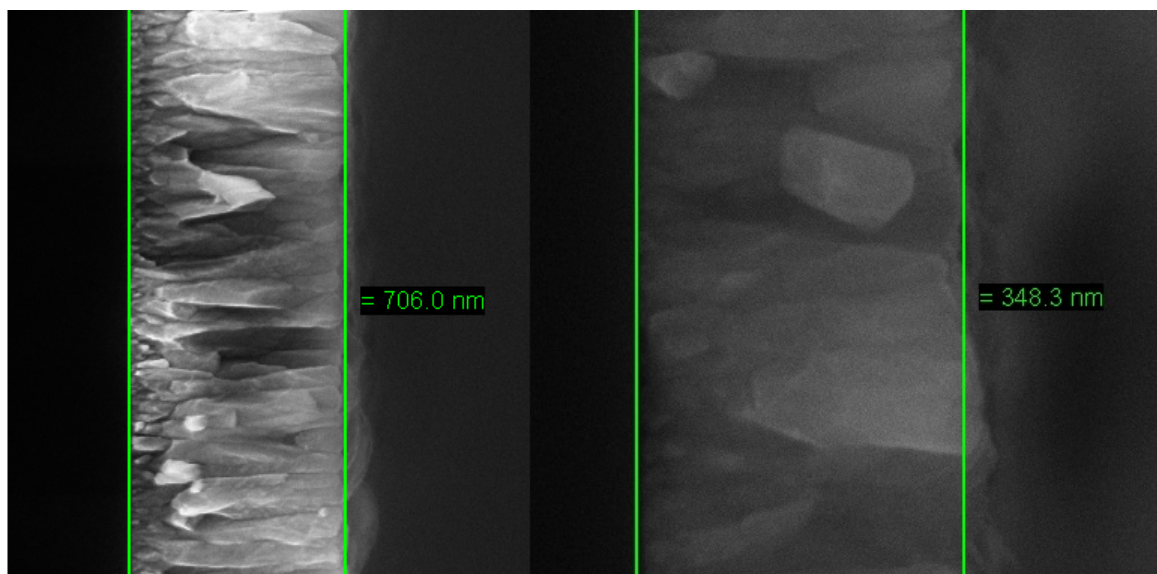
Figure 71: *ZnO ARC thickness measured with a SEM.*

6   Literature comparison

Some improvement results were sourced from the literature to compare to the improvements presented in this thesis. Comparable results with regard to wavelength range and feature sizes were found for moth-eye structures as well as for truncated cones, but good source data on anti moth-eye and deposited colloids was not found. In addition, no comparable results for ARCs were found, as most of the sources found were for solar applications, and usually in the < 1 μm range. A comparison for four results in the literature is presented below in figures 72 to 75.

Transmission results for moth-eye structures made with CdTe can be found in [8], and are presented in figure 72. These structures were fabricated with colloid-lithography, and were successfully measured with SEM to confirm correct structures sizes. Transmission improvement of up to $\approx 12\%$ was achieved at 5 μm, with some even improvements across the 3-18 μm range. The simulated results show an average of 19% improvement, which is higher over the whole range, but is comparable, yet higher around 5 μm. It was expected that the simulated results produces somewhat higher numbers, and so it seems that there is good correlation between simulated improvement and expected improvement through the literature.

Figure 72: *Comparison between the simulated results obtained in this thesis to experimentally measured transmissivity for moth-eye structures of similar sizes.*

The second structures to be compared is for HgCdTe (MCT) moth-eye structures found in [37]. Cadmium telluride, and its mercury alloy have very similar properties [43], and so are comparable. This paper presents 3.0-3.5 μm diameter, 6.1 μm high moth-eye structures with the reflection spectrum presented in figure 73. The reflection spectrum for 2.5 μm diameter, 7.07 μm tall CdTe moth-eye structures are presented in the same spectrum. The geometries for these structures is similar enough for them to be compared,

as it has been found here that the radius does not affect the transmission so long as it is of proportional size to the wavelengths, and the heights are of comparable sizes. The reported improvements from this paper is of the same size as that of the simulations. The calculated average transmission improvement for the literature for this structure is 19.4%, and the improvement for the simulated results is 23.5%, both numbers calculated in MATLAB.
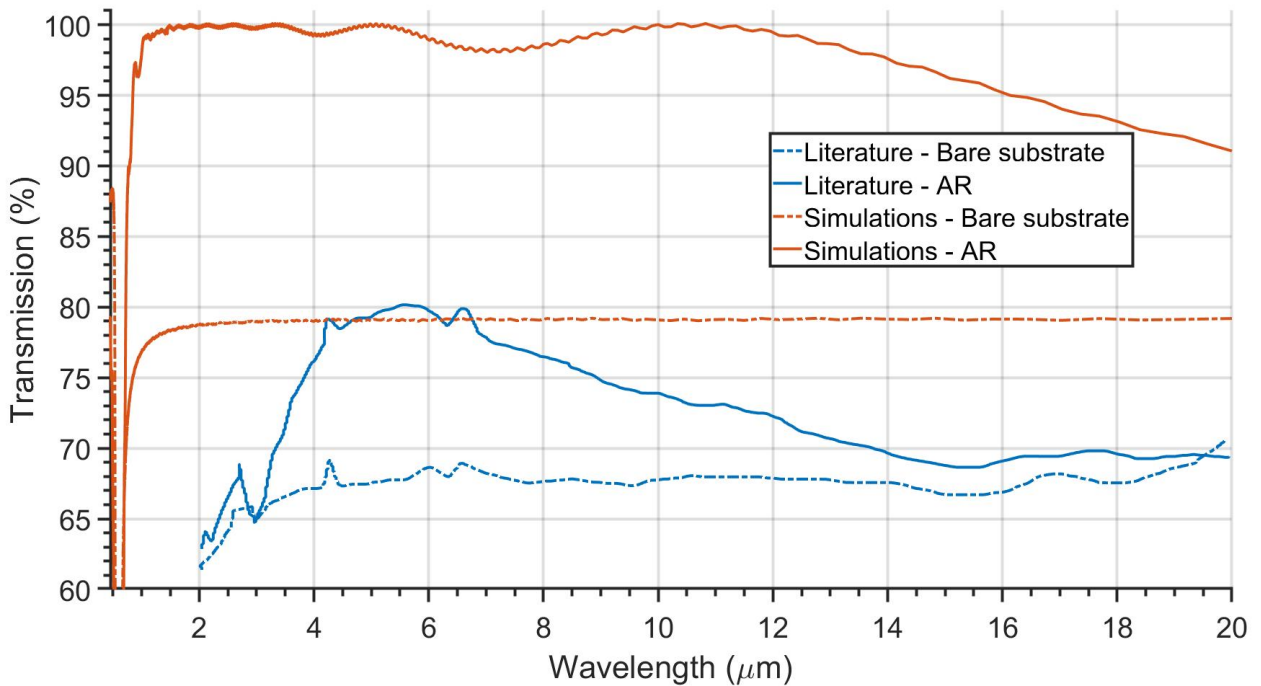

Figure 73: *Comparison between the simulated results obtained in this thesis to experimentally measured reflectivity for moth-eye structures of similar sizes.*

The next two comparisons are made to the same simulation, as the structure sizes in the literature sources are very similar and of the same material. The results are acquired from [19] and [25]. The first reported transmission is of CdZnTe (CZT) truncated cones which for figure 74 has $r_0 = 1.2$ μm and $h = 4$ μm, with a flat (unknown radius) top, and for figure 75, $r_0 = 1.15$ μm and $h = 3$ μm. The simulations are of CdTe with $r_0 = 1.25$ μm, $r_{top} = 0.4$ μm and $h = 4.4$ μm. The average transmission improvements for the two reported results are 11.6% and 10.8% for figures 74 and 75 respectively. The average transmission improvements for the simulations are 21.1%. The correlations here look good, as the back-side reflections are not included in the simulations, causing their results to be generally higher.

Figure 74: *Comparison between the simulated results obtained in this thesis to experimentally measured transmissivity for truncated cone structures of similar sizes.*

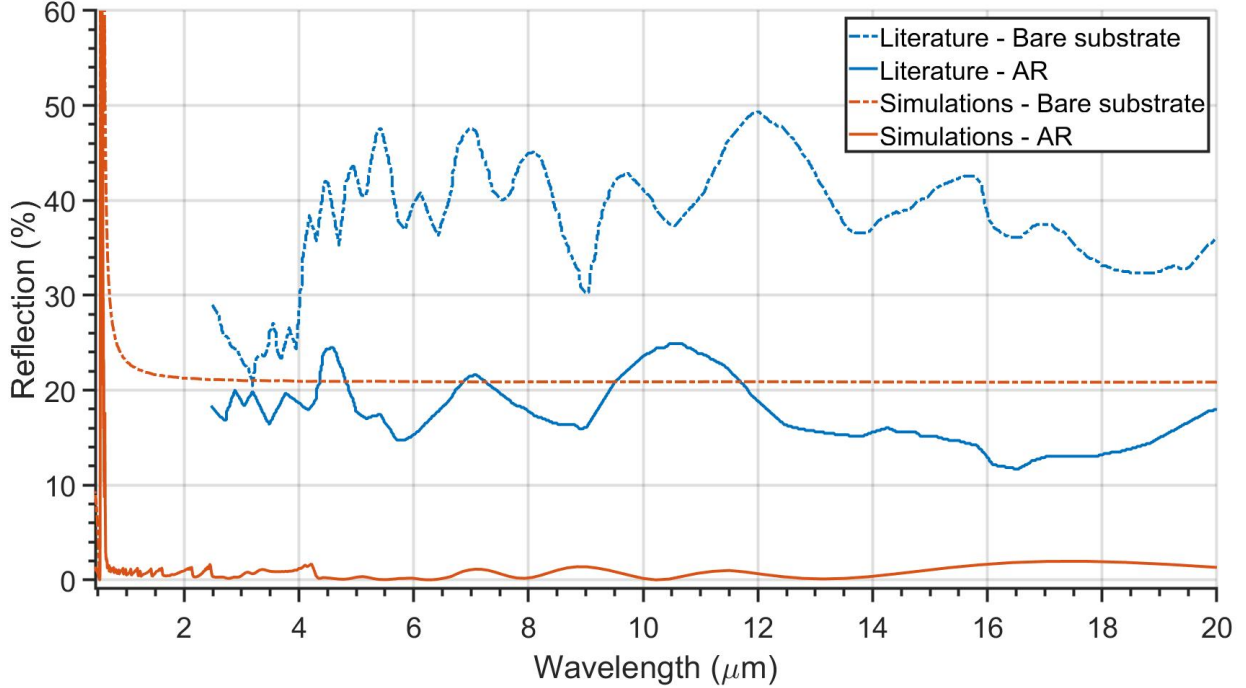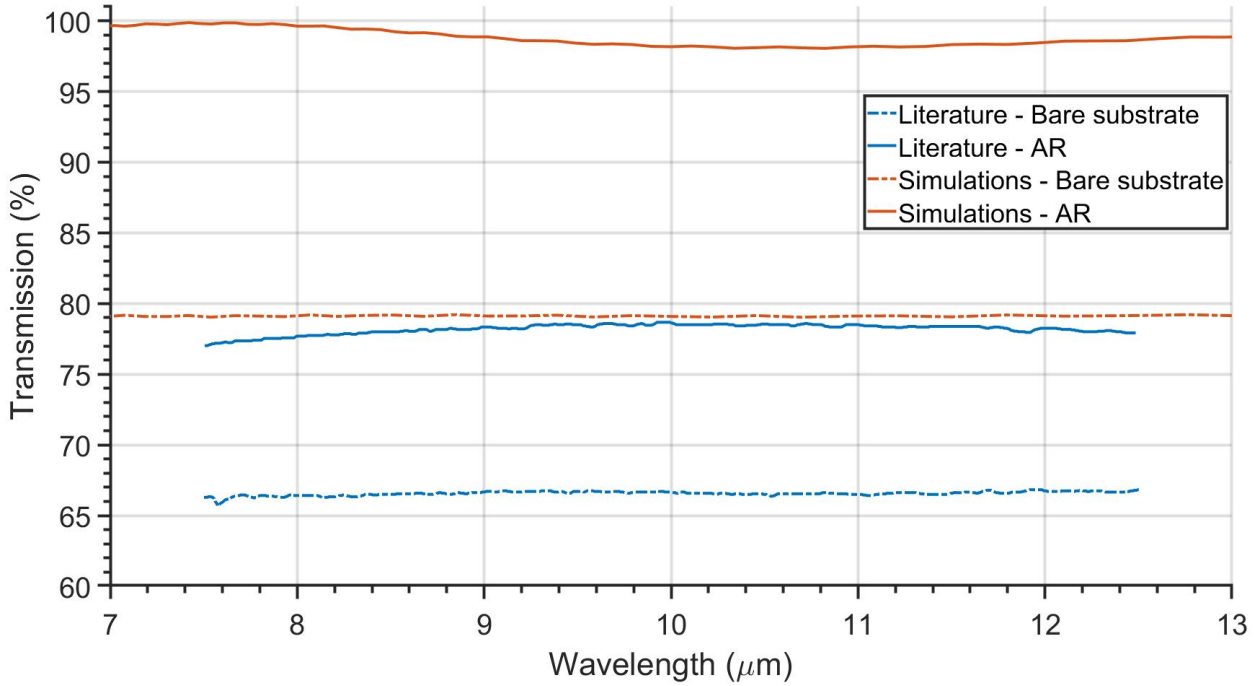***Figure 75:*** *Comparison between the simulated results obtained in this thesis to experimentally measured transmissivity for truncated cone structures of similar sizes.*
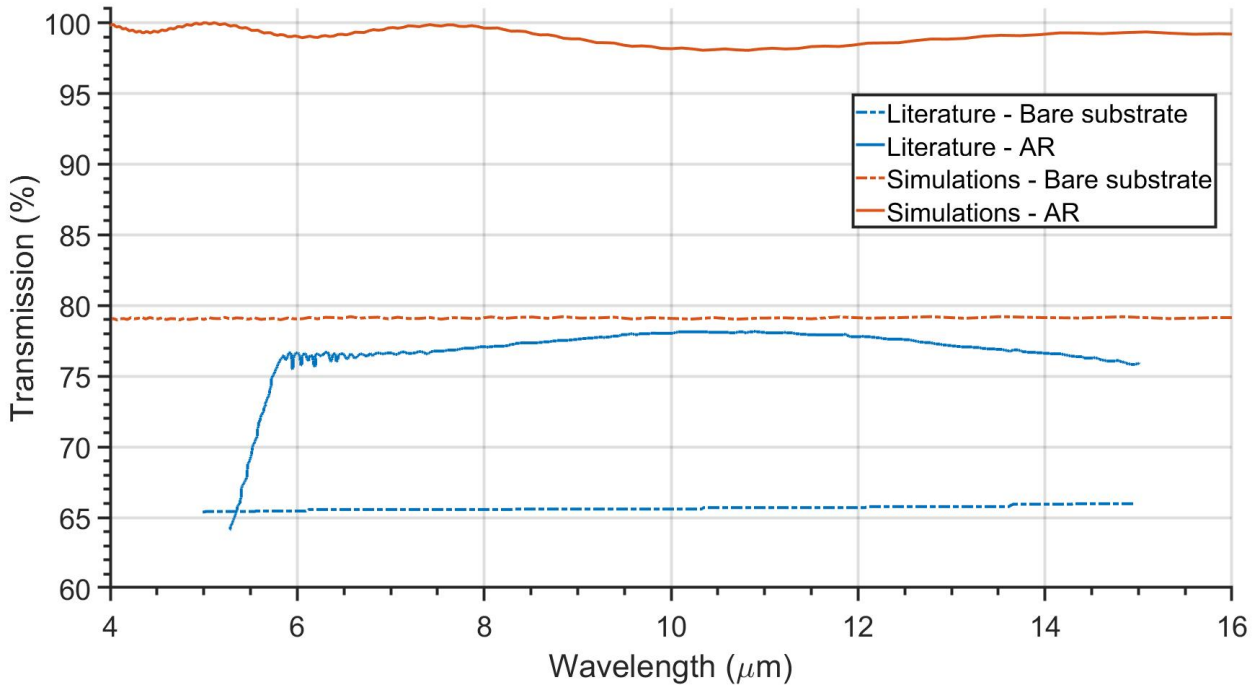
84

7   Conclusion

In this work, the goal has been investigate and optimise anti-reflective methods to achieve the highest transmission possible in the infrared for cadmium telluride (CdTe) substrates. The two atmospheric windows with ranges 3-5 μm and 8-12 μm were the main focus. Two approaches for anti-reflective properties were studied and simulated, namely anti-reflective coatings (ARCs) and anti-reflective micro-structures (ARMS).

For the ARCs, four different materials were selected from the literature and simulated based on their optical properties. Different thicknesses were calculated using the classical thin-film interference formula for the specific ranges and coating material. The substrate with coating is then simulated and optimised for higher transmission in the relevant ranges. The ARC simulations showed transmission results of 97% for the 3-5 μm range, and 96% for the 8-12 μm range. These were both realized by ZnO coating simulations on CdTe. The silicon simulations for the same ARC reached only slightly lower values of 96% and 95%, making these results comparable. The transmission improvements for ZnO on silicon was thus 18% and 17% for the 3-5 μm and 8-12 ranges μm.

For the ARMS, four different structures were selected from the literature, simulated and then analysed. It is hard to determine the relationship between the structure parameters and the transmission results, but some observations were made. By increasing the height of the structures, the transmission band-width increased, and the periodicity of the interference effects were reduced. As the height increases, the gradient is reduced by distributing the packing fraction over a longer distance, allowing transmission over an even broader range, so this consequence is predicted from the theory. And the taller the structures, the longer the wavelengths that interfere in the z-direction are, so the reduction of low-wavelength interference is also not surprising. It was also observed that the transmission into the substrate is not very dependent on the radii of the structures. The packing fraction of the ARMS does not change by increasing their radii, and so the gradient is also unaffected. Though the radius affects the periodicity of the ARMS and hence also should affect interference, and it would also affect *which* wavelengths are the most affected, as it is generally understood that the wavelengths and structure sizes should be of the same order to achieve best AR methods [45]. The ARMS simulations yielded high transmission improvements, from $\approx$ 78% transmission from substrate, to $>$ 99% for narrow bands. Specifically, moth-eye structures improved transmission over the entire 0.45-20 μm range by 19% on average, with truncated cones improving transmission by 17% over the range. For the 3-5 μm and 8-12 μm bands, the best transmissions were 99.9% and 99.6% for moth-eye, and 99.7% for both 3-5 μm and 8-12 μm for truncated cones.

Finally, due to the somewhat easier method of applying ARCs, proof of principle experiments were performed. ZnO films were deposited onto silicon substrates by magnetron sputtering. The transmission spectrum was then captured with an FTIR and the film-thicknesses were confirmed in a SEM. The samples were then compared to the simulated results. The experimentally measured transmissivity for ZnO coating on silicon is somewhat lower than that from the simulations, at 67% and 69% for the same ranges, an improvement of $\approx$ 12 and $\approx$ 14%μm from substrate transmission at the relevant ranges.

8 Appendix

8.1 Lumerical geometric script

Listing 1: Geometry spesification script for Lumerical that was used specifically for Motheye. The scripts for the other geomtries followed the same recipe but with slight changes.

```
1  deleteall;
2
3  hex = true; #hexagonal or square structure
4  xdistance = 1;
5
6  if (hex){xdistance = sqrt(3);}
7
8  for(i=1:nx) {
9          for(j=1:ny) {
10                 addcustom;
11                 set("name","parabola");
12                 set("material",material);
13
14                 set("x",distance*(i-2)*(sqrt(3)/2));
15                 set("y",distance*(j-2)+ (0.5*distance*xdistance)
                      );
16                 set("z",0);
17                 set("x span",height);
18                 set("y span",r0*2);
19                 set("z span",r0*2);
20
21                 a=4*height/(r0)^2;
22                 ?eqn = "sqrt((x+"+ num2str(height) + "/2)/"+
                      num2str(a)+")";
23
24
25                 set("equation units","m");
26                 set("create 3D object by","revolution");
27                 set("equation 1",eqn);
28
29                 set("first axis","y");
30                 set("rotation 1",90);
31         }
32         if (hex){ xdistance = 1;
33         }else{ xdistance = 0; }
34  }
```

References

[1]   Sadao Adachi. *Optical constants of crystalline and amorphous semiconductors : numerical data and graphical information / Sadao Adachi.* eng. Boston: Kluwer Academic Publishers, 1999. ISBN: 0792385675 (cit. on p. 11).

[2]   Petri Ala-Laurila. "Visual Neuroscience: How Do Moths See to Fly at Night?" In: *Current Biology* 26.6 (2016), R231–R233. ISSN: 0960-9822. DOI: https://doi.org/10.1016/j.cub.2016.01.020. URL: https://www.sciencedirect.com/science/article/pii/S0960982216000701 (cit. on p. 19).

[3]   Aldona Beganskienė et al. "Sol-gel derived antireflective coating with controlled thickness and reflective index". In: *Materials Science- Poland* 25 (Jan. 2007) (cit. on p. 23).

[4]   Bell, R.O. "Review of optical applications of CdTe". In: *Rev. Phys. Appl. (Paris)* 12.2 (1977), pp. 391–399. DOI: 10.1051/rphysap:01977001202039100. URL: https://doi.org/10.1051/rphysap:01977001202039100 (cit. on p. 11).

[5]   Pascal Buskens et al. "Antireflective Coatings for Glass and Transparent Polymers". In: *Langmuir* 32.27 (2016). PMID: 27187719, pp. 6781–6793. DOI: 10.1021/acs.langmuir.6b00428. eprint: https://doi.org/10.1021/acs.langmuir.6b00428. URL: https://doi.org/10.1021/acs.langmuir.6b00428 (cit. on p. 15).

[6]   Peiris F. C. et al. "Precise measurements of the dispersion of the index of refraction for Cd1-xZnxTe alloys". In: *Journal of Electronic Materials* 29.6 (June 2000). DOI: 10.1007/s11664-000-0227-9. URL: https://doi.org/10.1007/s11664-000-0227-9 (cit. on p. 6).

[7]   Lina Cao and Kursat Sendur. "Surface Roughness Effects on the Broadband Reflection for Refractory Metals and Polar Dielectrics". In: *Materials* 12.19 (2019). ISSN: 1996-1944. DOI: 10.3390/ma12193090. URL: https://www.mdpi.com/1996-1944/12/19/3090 (cit. on pp. 33, 73).

[8]   Lesley Chan et al. "Fabrication and optical behavior of graded-index, moth-eye antireflective structures in CdTe". In: *Journal of Vacuum Science and Technology B, Nanotechnology and Microelectronics: Materials, Processing, Measurement, and Phenomena* 35 (Jan. 2017), p. 011201. DOI: 10.1116/1.4971770 (cit. on pp. 5, 15, 81).

[9]   Lesley W Chan, Daniel E Morse, and Michael J Gordon. "Moth eye-inspired antireflective surfaces for improved IR optical systems visible LEDs fabricated with colloidal lithography and etching". In: *Bioinspiration Biomimetics* 13.4 (May 2018), p. 041001. DOI: 10.1088/1748-3190/aab738. URL: https://doi.org/10.1088/1748-3190/aab738 (cit. on p. 27).

[10] Yen-Chun Chao et al. "Light scattering by nanostructured anti-reflection coatings". In: *Energy Environ. Sci.* 4 (9 2011), pp. 3436–3441. DOI: 10.1039/C0EE00636J. URL: http://dx.doi.org/10.1039/C0EE00636J (cit. on p. 6).

[11] David B. Chenault, Russell A. Chipman, and Shih-Yau Lu. "Electro-optic coefficient spectrum of cadmium telluride". In: *Appl. Opt.* 33.31 (Nov. 1994), pp. 7382–7389. DOI: 10.1364/AO.33.007382. URL: http://opg.optica.org/ao/abstract.cfm?URI=ao-33-31-7382 (cit. on p. 51).

[12] International Crystal. *Optical Material Properties*. URL: `%5Curl%7Bhttps://www.internationalcrystal.net/materials-technology/%7D` (cit. on p. 7).

[13] Litong Dong et al. "Fabrication of hierarchical moth-eye structures with durable superhydrophobic property for ultra-broadband visual and mid-infrared applications". In: *Appl. Opt.* 58.24 (Aug. 2019), pp. 6706–6712. DOI: `10.1364/AO.58.006706`. URL: `http://opg.optica.org/ao/abstract.cfm?URI=ao-58-24-6706` (cit. on p. 8).

[14] Jian-Shuen Fang et al. "Path-dependent human identification using a pyroelectric infrared sensor and Fresnel lens arrays". In: *Optics express* 14 (Feb. 2006), pp. 609–24. DOI: `10.1364/OPEX.14.000609` (cit. on p. 12).

[15] Federico Lora Gonzalez and Michael J. Gordon. "Bio-inspired, sub-wavelength surface structures for ultra-broadband, omni-directional anti-reflection in the mid and far IR". In: *Opt. Express* 22.11 (June 2014), pp. 12808–12816. DOI: `10.1364/OE.22.012808`. URL: `http://opg.optica.org/oe/abstract.cfm?URI=oe-22-11-12808` (cit. on pp. 19, 20).

[16] David J. Griffiths. *Introduction to Electrodynamics*. Fourth edition. Cambridge university press, 2017 (cit. on p. 8).

[17] P. GRODZINSKI. *Indentation Hardness of Diamond*. June 1956. DOI: `10.1038/1771228a0`. URL: `https://doi.org/10.1038/1771228a0` (cit. on p. 54).

[18] Pavel Hlidek et al. "Refractive index of CdTe: Spectral and temperature dependence". In: *Journal of Applied Physics* 90 (Aug. 2001), pp. 1672–1674. DOI: `10.1063/1.1385351` (cit. on pp. 6, 14, 45).

[19] Douglas S. Hobbs and Bruce D. MacLeod. "Design, fabrication, and measured performance of anti-reflecting surface textures in infrared transmitting materials". In: *Window and Dome Technologies and Materials IX*. Ed. by Randal W. Tustison. Vol. 5786. International Society for Optics and Photonics. SPIE, 2005, pp. 349–364. DOI: `10.1117/12.604532`. URL: `https://doi.org/10.1117/12.604532` (cit. on pp. 15, 17, 82).

[20] Simon G Kaplan and Leonard M Hanssen. "Silicon as a standard material for infrared reflectance and transmittance from 2 to 5 microns". In: *Infrared Physics and Technology* 43.6 (2002), pp. 389–396. ISSN: 1350-4495. DOI: `https://doi.org/10.1016/S1350-4495(02)00161-5`. URL: `https://www.sciencedirect.com/science/article/pii/S1350449502001615` (cit. on p. 8).

[21] Knightoptical. *Infrared coatings*. URL: `https://www.knightoptical.com/infrared-coatings/` (visited on 02/15/2022) (cit. on p. 16).

[22] Goshi Kuno and Kota Sakaguchi. "Anti-reflective biomimetic nanostructures formed by 2D arrays of silica colloidal particles via self-assembly using sublimation, polymer solidification, and thermal fusion". In: *Applied Surface Science* 564 (2021), p. 150406. ISSN: 0169-4332. DOI: `https://doi.org/10.1016/j.apsusc.2021.150406`. URL: `https://www.sciencedirect.com/science/article/pii/S016943322101480X` (cit. on p. 23).

[23] Bo-Tau Liu and Wei-De Yeh. "Antireflective surface fabricated from colloidal silica nanoparticles". In: *Colloids and Surfaces A: Physicochemical and Engineering Aspects* 356.1 (2010), pp. 145–149. ISSN: 0927-7757. DOI: `https://doi.org/10.1016/j.colsurfa.2010.01.003`. URL: `https://www.sciencedirect.com/science/article/pii/S0927775710000130` (cit. on p. 23).

[24] Lumerial. *Finite Difference Time Domain (FDTD) solver introduction.* `https://support.lumerical.com/hc/en-us/articles/360034914633-Finite-Difference-Time-Domain-FDTD-solver-introduction`. Accessed: 2021-13-12 (cit. on pp. 27, 29).

[25] Bruce D. MacLeod and Douglas S. Hobbs. "Long life, high performance anti-reflection treatment for HgCdTe infrared focal plane arrays". In: *Infrared Technology and Applications XXXIV*. Ed. by Bjørn F. Andresen, Gabor F. Fulop, and Paul R. Norton. Vol. 6940. International Society for Optics and Photonics. SPIE, 2008, pp. 318–333. DOI: `10.1117/12.778736`. URL: `https://doi.org/10.1117/12.778736` (cit. on pp. 23, 82).

[26] D. T. F. Marple. "Refractive Index of ZnSe, ZnTe, and CdTe". In: *Journal of Applied Physics* 35.3 (1964), pp. 539–542. DOI: `10.1063/1.1713411`. eprint: `https://doi.org/10.1063/1.1713411`. URL: `https://doi.org/10.1063/1.1713411` (cit. on pp. 6, 45).

[27] Materion. *IR COATINGS AND APPLICATIONS*. URL: `https://materion.com/resource-center/news-archive/microelectronics-and-services/ir-coating-designs-and-applications` (visited on 02/15/2022) (cit. on p. 16).

[28] *n,k database*. 2022. URL: `http://www.ioffe.ru/SVA/NSM/nk/index.html#Silicon` (visited on 04/02/2022) (cit. on p. 29).

[29] David Nečas and Petr Klapetek. *Gwyddion*. Nov. 12, 2021. URL: `%5Curl%7Bhttp://gwyddion.net/%7D` (cit. on p. 45).

[30] Emund Optics. *Cadmium Terlluride (CdTe) Windows*. URL: `https://www.edmundoptics.com/f/cadmium-telluride-cdte-windows/39727/` (cit. on pp. 7, 29).

[31] Emund Optics. *DIAMOND-LIKE CARBON COATINGS*. URL: `https://www.edmundoptics.eu/capabilities/diamond-like-carbon-coatings/` (visited on 02/24/2022) (cit. on p. 16).

[32] ISP optics. *Window transmission curves*. URL: `%5Curl%7Bhttps://www.lakeshore.com/products/product-detail/janis/accessories-and-ancillary-equipment/window-transmission-curves%7D` (cit. on p. 7).

[33] Edward D Palik. *Handbook of optical constants of solids*. Vol. 3. Academic press, 1998 (cit. on pp. 6, 29, 45).

[34] Phillip Papatzacos et al. "Simulated effects of wet-etched induced surface roughness on IR transmission and reflection". In: *2020 IEEE 8th Electronics System-Integration Technology Conference (ESTC)*. 2020, pp. 1–4. DOI: `10.1109/ESTC48849.2020.9229821` (cit. on p. 33).

[35] Dr. Rüdiger Paschotta. *infrared light*. Ed. by Wiley. URL: `%5Curl%7Bhttps://www.rp-photonics.com/infrared_light.html%7D` (cit. on p. 5).

[36] M H Patterson and R H Williams. "Surface layers on cadmium telluride". In: *Journal of Physics D: Applied Physics* 11.5 (Apr. 1978), pp. L83–L86. DOI: `10.1088/0022-3727/11/5/003`. URL: `https://doi.org/10.1088/0022-3727/11/5/003` (cit. on pp. 5, 18, 26).

[37] Dimuthu Perera, James W. Pattison, and Priyalal S. Wijewarnasuriya. "Minimizing Reflectivity by Etching Microstructures in Mercury Cadmium Telluride (HgCdTe)". In: 2013 (cit. on p. 81).

[38] M. N. Polyanskiy. *Refractive index database*. URL: `https://refractiveindex.info` (visited on 02/09/2022) (cit. on p. 29).

[39] Hemant Kumar Raut et al. "Anti-reflective coatings: A critical, in-depth review". In: *Energy Environ. Sci.* 4 (10 2011), pp. 3779–3804. DOI: `10.1039/C1EE01297E`. URL: `http://dx.doi.org/10.1039/C1EE01297E` (cit. on p. 16).

[40] Reading. *Cadmium telluride CdTe*. URL: `https://www.reading.ac.uk/infrared/technical-library/cadmium-telluride-cdte` (cit. on pp. 6, 7, 29).

[41] Barry Rice. *Atmospheric windows*. 2022. URL: `http://www.sarracenia.com/astronomy/remotesensing/physics060.html` (visited on 02/02/2022) (cit. on p. 29).

[42] rmico. *Anti Reflection (AR)*. URL: `http://rmico.com/single-layer-ar` (visited on 02/15/2022) (cit. on p. 16).

[43] Antoni Rogalski. *Infared detectors*. Second edition. CRC Press, 2011 (cit. on pp. 8, 60, 81).

[44] Antoni Rogalski. "Infrared detectors: an overview". In: *Infrared Physics and Technology* 43.3 (2002), pp. 187–210. ISSN: 1350-4495. DOI: `https://doi.org/10.1016/S1350-4495(02)00140-8`. URL: `https://www.sciencedirect.com/science/article/pii/S1350449502001408` (cit. on p. 8).

[45] Antoni Rogalski. "Infrared detectors: status and trends". In: *Progress in Quantum Electronics* 27.2 (2003), pp. 59–210. ISSN: 0079-6727. DOI: `https://doi.org/10.1016/S0079-6727(02)00024-1`. URL: `https://www.sciencedirect.com/science/article/pii/S0079672702000241` (cit. on p. 85).

[46] Antoni Rogalski and K. Chrzanowski. "Infrared Devices And Techniques (Revision)". In: *Metrology and Measurement Systems* 21 (Dec. 2014). DOI: `10.2478/mms-2014-0057` (cit. on pp. 12, 14).

[47] International Gem Society. *The Mohs Hardness Scale and Chart for Select Gems*. URL: `%5Curl%7Bhttps://www.gemsociety.org/article/select-gems-ordered-mohs-hardness/%7D` (cit. on p. 18).

[48] Z. Tomashik et al. "Chemical–Mechanical Polishing of CdTe and Zn x Cd1-x Te Single Crystals by H2O2(HNO3)-HBr-Organic Solvent Etchant Compositions". In: *Journal of Electronic Materials* 38 (Aug. 2009). DOI: `10.1007/s11664-009-0692-8` (cit. on pp. 32, 33).

[49] "Crystal Growth and Surfaces - Chapter I". In: European Materials Research Society Series (2010). Ed. by Robert Triboulet and Paul Siffert. DOI: `https://doi.org/10.1016/B978-0-08-096513-0.00001-7`. URL: `https://www.sciencedirect.com/science/article/pii/B9780080965130000017` (cit. on p. 26).

[50] "Crystal Growth and Surfaces - Chapter II - Applications". In: European Materials Research Society Series (2010). Ed. by Robert Triboulet and Paul Siffert, pp. 145–255. DOI: https://doi.org/10.1016/B978-0-08-096513-0.00002-9. URL: https://www.sciencedirect.com/science/article/pii/B9780080965130000029 (cit. on pp. 5, 7).

[51] II-VI. *II-VI Incorporated*. URL: https://ii-vi.com/ (visited on 03/01/2022) (cit. on p. 42).

[52] Visimax. *VisiClear – Anti-Reflection Optical Coating*. URL: https://visimaxtechnologies.com/optical-coating-products/anti-reflection-visiclear-game-changing-anti-reflection/ (visited on 02/15/2022) (cit. on p. 16).

[53] Ligang Xu, Liangjuan Gao, and Junhui He. "Fabrication of visible/near-IR antireflective and superhydrophobic coatings from hydrophobically modified hollow silica nanoparticles and poly(methyl methacrylate)". In: *RSC Adv.* 2 (33 2012), pp. 12764–12769. DOI: 10.1039/C2RA22107A. URL: http://dx.doi.org/10.1039/C2RA22107A (cit. on p. 16).

[54] G.F. Zhang and X. Zheng. "Optical transmittance of antireflective diamond-like coatings on ZnS substrates". In: *Surface and Coatings Technology* 82.1 (1996), pp. 110–113. ISSN: 0257-8972. DOI: https://doi.org/10.1016/0257-8972(95)02655-X. URL: https://www.sciencedirect.com/science/article/pii/025789729502655X (cit. on p. 16).

[55] Gang Zhang and Dayang Wang. "Colloidal lithography - The art of nanochemical patterning". English (US). In: *Chemistry - An Asian Journal* 4.2 (Feb. 2009), pp. 236–245. ISSN: 1861-4728. DOI: 10.1002/asia.200800298 (cit. on p. 27).

[56] Sichao Zhang and Yifang Chen. "Nanofabrication and coloration study of artificial Morpho butterfly wings with aligned lamellae layers". In: *Scientific reports* 5 (Nov. 2015), p. 16637. DOI: 10.1038/srep16637 (cit. on pp. 18, 19).